University of São Paulo
The University of Astronomy, Geophysics and Atmospheric Sciences
Department of Atmospheric Sciences

Katherine Lisbeth Ccoica López

Interannual variability of Tropical Atlantic and its influence on extreme precipitation events: Focus on the Amazon Basin

São Paulo
2020

Katherine Lisbeth Ccoica López

Interannual variability of Tropical Atlantic and its influence on extreme precipitation events: Focus on the Amazon Basin

Dissertion presented at the Institute of Astronomy, Geophysics and Atmospheric Sciences at the University of São Paulo as a partial requirement for obtaining the title of Master of Sciences.

Area of concentration: Meteorology
Advisor: Prof. Dr. Ricardo Hallak

"Corrected version. The original is avaible at the Unity"

São Paulo

2020

To my mom, my dad and Mathias.

For everything we've been through to get here.

Acknowledgements

To God, for the gift of life.

To my parents, Rosa and José, my brother, Mathias, and my sister, Ginna, for all the love, affection, support and for having taught me the true value of family, friendship and education in human life.

To my advisor, Ricardo Hallak, for the opportunity, for having believed and trusted me, and mainly, for his patience.

To Victor C. Mayta for all the support, interesting discussions and suggestions that helped me improve this work. And also for the great friendship that I found in him.

To my brothers I met here, Luis and Carlos, for their friendship, conversations, constant support and all the good times we spent together. To Eleazar and my Brazilian mother, Claudia, for their support during this period here in Brazil. And to all friends that I met here.

To my colleagues and friends Gabriel, Pedro, Lucas, Diogo, Wesley, Alan and Lucão, for their friendship, companionship and help in many stages of my stay at IAG.

To IAG teachers and staff for the teaching and support that contributed to this work. Special thanks to Prof. Dr. Charles Jones for sharing some tools applied in this study.

To the National Council for Scientific and Technological Development (CNPq) for financial support.

Esta tese/dissertação foi escrita em LaTeX com a classe IAGTESE, para teses e dissertações do IAG.

Resumo

Este estudo fornece uma análise, em escala de tempo interanual, da influência dos oceanos Pacífico tropical e Atlântico no regime de precipitação na América do Sul, com foco na Bacia Amazônica. Para esse fim, primeiro os dados mensais da temperatura da superfície do mar (SST) são usados para determinar os principais modos de variabilidade em três regiões do Atlântico: Atlântico Tropical Norte (TNA), Atlântico Tropical Sul (TSA) e Atlântico Sul Subtropical (STSA). Esses padrões são obtidos da Função Ortogonal Empírica (EOF), onde o primeiro modo (PC1) de cada região explica a variabilidade interanual em porcentagem alta, além de mostrar os picos de SST relacionados a eventos extremos de precipitação na Bacia Amazônica. Além disso, a interação do Pacífico e Atlântico foi analisada por correlações móveis e ondeletas cruzadas para o período 1880-2017, usando índices do Pacífico (índices E e C) e o PC1 de cada região do Atlântico. Os resultados mostram que as regiões do Atlântico estiveram acopladas e desacopladas em determinados períodos. Da mesma forma, os oceanos Pacífico e Atlântico foram mostrados em fase ou fase oposta em diferentes períodos de tempo e escalas de frequência. Finalmente, a precipitação de dados do satélite e dados combinados (observado e satélite) para o período 1940-2010 foram usados para identificar as regiões onde o SST do Pacífico e do Atlântico influenciam. Os resultados sugerem que os diferentes ingredientes de El Niño Southern Oscillation (ENSO) impactam principalmente na precipitação durante o início (outubro-novembro) e o pico (dezembro-fevereiro) do Sistema de Monção da América do Sul (SAMS). Também é mostrado que condições anômalas sobre o Oceano Atlântico Tropical Norte e Sul afetam os regimes de precipitação durante o final (março-abril) e o período de ausência do SAMS (maio-setembro), enquanto o Atlântico Sul Subtropical afeta a precipitação durante o pico e durante a ausência do SAMS. O fluxo de umidade,

sua divergência e a estrutura vertical sobre a América do Sul e os oceanos adjacentes são obtidos para diferentes condições dos oceanos tropicais, através dos índices oceânicos. Os resultados mostram que condições anômalas da temperatura da superfície do mar nessas regiões oceânicas modificam as regiões de fonte e sumidouro da umidade atmosférica em todas as estações. Uma redução no fluxo de umidade, principalmente em condições tropicais quentes do Atlântico, pode levar a períodos extremamente secos no centro-sul da Amazônia e no norte da Bacia da Prata. Esse efeito, de fato, pode ser ainda mais extremo na América do Sul, quando é precedido pelo evento El Niño. No entanto, impactos contrastantes são observados durante os anos do El Niño, com deficit pluviométrico na América do Sul tropical, a leste dos Andes e excesso de chuva no sudeste da América do Sul e noroeste dos Andes (norte do Peru, litoral do Equador e Colômbia). Os resultados fornecem uma análise que ajudará a melhorar as políticas de adaptação e gerenciamento de riscos relacionadas aos impactos da variabilidade e mudança climática.

Palavras chave: *variabilidade da chuva; análise de clusters; índices oceânicos; precipitação extrema; variabilidade interanual da SST; variabilidade interdecadal da SST.*

Abstract

This study provides a detailed analysis, in the interannual time-scale, of the influence of the tropical Pacific and the Atlantic Ocean in the precipitation regime over South America, with a focus on the Amazon Basin. For this purpose, first, monthly sea surface temperature data is used to determine the principal modes of variability in three Atlantic regions: Tropical North Atlantic (TNA), Tropical South Atlantic (TSA), and Subtropical South Atlantic (STSA). These patterns are obtained from Empirical Orthogonal Function (EOF), where the first mode (PC1) of each region explains the interannual variability in high percentage. The PC1 time series also shows SST peaks related to extreme precipitation events in the Amazon Basin. In addition, the Pacific and Atlantic interaction was analyzed by moving correlations and cross-wavelets for the 1880-2017 period, using Pacific indices (E and C index) and the PC1 of each Atlantic region. We found that the Atlantic regions have been coupling and decoupling in specific periods. Likewise, the Pacific and the Atlantic oceans have been shown in-phase or in opposite phase in different periods of time and frequencies. Precipitation from satellite and combined observed-satellite for the 1940-2010 period were used to identify regions influenced by the Pacific and Atlantic SST. The results suggest that different El Niño Southern Oscillation (ENSO) flavors mainly impact precipitation during the onset (October-November) and peak (December-February) of the South America Monsoon System (SAMS). We have also shown that anomalous conditions over the Tropical North and South Atlantic Ocean impact precipitation regimes during the demise (March-April) and the absence of the SAMS (May-September), while the Subtropical South Atlantic impacts in precipitation during the peak and the absence of the SAMS. Additionally, moisture flux, its divergence, and vertical structure over South America and the adjoining oceans were obtained for different conditions of tropical oce-

ans, through the oceanic indices. Results show that anomalous conditions of sea surface temperature in these oceanic regions modify the source and sink regions for atmospheric moisture in all seasons. A reduction in the moisture inflow, mainly in warm tropical Atlantic conditions, could lead to extremely dry periods in central-southern Amazon and the northern La Plata Basin. This effect, indeed, could be even more extreme in tropical South America when it is preceded by the El Niño event. However, contrasted impacts are observed during El Niño years, with rainfall deficit in tropical South America, east of the Andes, and rainfall excess over southeastern South America and northwest of the Andes (northern Peru, coastal Ecuador, and Colombia). These findings provide an analysis that will help to improve adaptation and risk management policies related to impacts of climate variability and change.

Keywords: *rainfall variability; cluster analysis; oceanic indices; extreme precipitation; interannual SST variability; interdecadal SST variability.*

List of Figures

List of Tables

Contents

Chapter 1

Introduction

Precipitation from a given location is the result of a series of physical events with widely varying timescales, even the causes of rainfall can be a mixture of local and remote (teleconnections) factors. The Amazon Basin is located between 5° N - 20° S, and its area is approximately 6 300 000 km^2, covering Brazil, Peru, Colombia, Bolivia, Ecuador, Venezuela, and Guyana, and is one of the regions with the highest precipitation and water vapor in the world, with an average annual precipitation of 2300 mm (Fisch et al., 1998). Since rainfall depends on the availability of water vapor in the region, Molion (1987) discusses that the formation of the precipitation is due to three mainly factors: a daytime convection due to surface heating, lines of instability in the North or Northeast of Brazil, and meso- and large-scale convective clouds clusters and frontal systems to the South/Southeast of Brazil that reach the basin. All of these components result in a complex interaction of various large-scale physical and dynamic processes, which are responsible for the temporal and spatial distribution of precipitation (Figueroa and Nobre, 1990; Satyamurty et al., 1998).

Precipitation in the Amazon Basin is governed mainly by the South American Monsoon System (SAMS) and presents a wet season between November and March, when greater convective activity is observed, and a dry season from May to September; except for the region to the north of the basin, which depicts high rainfall between June to August (Fisch et al., 1998). However, this seasonality may be affected by an interannual variability associated with anomalies in the sea surface temperature (SST), which causes irregular rainfall periods, delaying or reducing the dry and wet seasons.

The remote influence of oceanic conditions in extreme precipitation (droughts and floods) over the Amazon on interannual time-scales was widely discussed in many previous

studies (e.g., Ropelewski and Halpert, 1987; Rao and Hada, 1990; Grimm et al., 2000; Espinoza et al., 2019; Cai et al., 2020, among others). Previous works also indicate an increasing in the amount of extreme cases over the past two decades (Marengo and Espinoza, 2016; Gloor et al., 2013; Barichivich et al., 2018; Espinoza et al., 2019). In this sense, strong El Niño events are related to a warm condition over the Eastern Pacific (e.g., 1982-1983, 1997-1998, 2015-2016) or Central (e.g., 2005-2006, 2010, 2015) Pacific (Timmermann et al., 2018; Freund et al., 2019; Cai et al., 2020). Nevertheless, there are also events associated with an anomalous temperature conditions of the tropical Atlantic (Marengo et al., 2008), which is the main source of moisture for the Amazon. Furthermore, the results indicate an increasing the amount of extreme cases over the past two decades which, in turn, has been given under a more active participation of the Tropical Atlantic (Marengo and Espinoza, 2016; Barichivich et al., 2018; Espinoza et al., 2019). This is the reason why the Atlantic regions become important for the understanding of the circulation mechanisms associated with extreme events in the Amazon.

1.1 Main objectives of this work

This study aims to assess the influence of the Atlantic variability in the Amazon Basin precipitation. For this purpose, the Atlantic Ocean is divided in different regions such as: Tropical North Atlantic, Tropical South Atlantic, and Subtropical South Atlantic. Each region is first studied separately, in order to obtain a specific relationship between them, and how the different peaks are related to extreme precipitation on the Amazon. Likewise, the interaction between the three observed Atlantic regions will be explored, their interaction with the equatorial Pacific. Finally, we will analyze how SST in these regions impacts the moisture flux transport into South America and the Amazon Basin.

The research is organized as follows: Section 2 provides a brief background of the principal Atlantic and Pacific Ocean modes, and how they impact extreme precipitation events. Section 3 describes the data and methodology. Section 4 presents the results. In addition, discussions about how the Pacific and Atlantic basins modulate extreme rainfall events over South America regions are considered. Finally, section 5 gives a summary and conclusions.

Chapter 2

Backgroung

The Amazon Basin is located in South America, between 5°N-20°S. It is considered the largest basin in the world, covering an approximate area of 6,100,000 km^2 covering the countries of Brazil, Peru, Colombia, Bolivia, Equador and Venezuela and Guiana (Espinoza et al., 2009) (Figure 2.1). Amazon Basin has the highest convective activity, the precipitation and water vapor in the world, where rainfall occurs in a large part of the year and, therefore, directly influences the atmospheric circulation of the tropics (Salati et al., 1978; Marengo and Hastenrath, 1993). Besides, the average annual rainfall of 2300mm, contributing 15% of freshwater to the oceans (Molinier et al., 1996; Espinoza et al., 2009).

The main moisture source of the Amazon Basin is the Tropical Atlantic Ocean, and the evapotranspiration of the forest, which plays a very important role in the recycling of water vapor, contributing to 50% of the rainfall in this region (Salati et al., 1978, among others). Nevertheless, precipitation is not homogeneous in the Amazon; it presents interannual and spatial variability, with greater content in the northeast and northwest of the basin and decreases for the tropics (Salati et al., 1978; Espinoza et al., 2009).

2.1 Interannual variability of precipitation in Amazon Basin

SST is one of the most important predictors of climate on interannual time-scale and has been largely studied to understand the interaction between the ocean and the atmosphere in a climatic perspective. Indeed, one of the most important coupled oceanic-atmosphere phenomenon in this scale is the El Niño-Southern Oscillation (ENSO), which is the interannual fluctuation of the SST in the equatorial Pacific Ocean, related to variations in

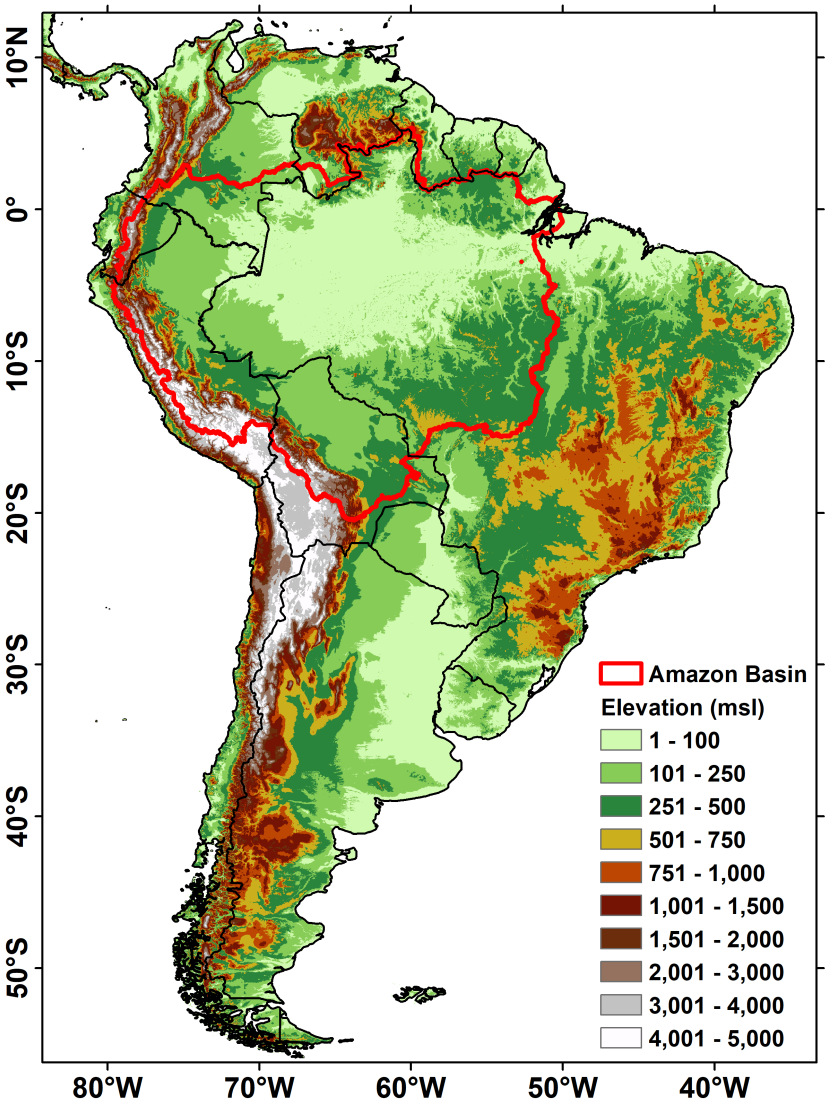

Figure 2.1: South America and Amazon Basin location (region enclosed in red line). Elevation areas are shown shaded (in meters above sea level, msl). Elevation values comes from a digital elevation model (DEM) of the GTOPO30 dataset, from USGS (U.S. Geological Survey).

the atmospheric wind circulation. ENSO influences climate variability in South America, especially in Peru, Ecuador, and Venezuela, as well as in Argentina, Chile, Paraguay and Brazil (Aceituno, 1988; Grimm et al., 2000). ENSO has two phases; the warm phase, when the SST anomalies are above-normal, known as the El Niño event, and the cold phase, when the anomalies are below-normal, known as the La Niña event. The Atlantic Ocean also exerts an strong control on precipitation variability over the Amazon, mainly the Tropical North Atlantic Ocean (TNA) compared with other Atlantic regions such as

the Tropical South Atlantic (TSA) (Yoon and Zeng, 2010).

The interannual rainfall variability in the Amazon is related to the El Niño/La Niña events in the equatorial Pacific and the warming/cooling of the TNA and TSA. Indeed, during the El Niño events, precipitation below-normal are recorded in the north and northeast of the Basin, while to the west and south, opposite conditions are observed. In contrast, La Niña events trigger rains above-normal in the north and northeast of the Amazonian (Ronchail et al., 2002; Marengo and Espinoza, 2016). However, there are also drought events, such as the 1964 and 2005 events, that were not related to the El Niño event, but rather to SST warm anomalies in the Tropical North Atlantic (Marengo et al., 2008). Another example is the drought observed in 2010, when for the first time a combined effect was observed: El Niño event followed by a warm-up of the TNA (Espinoza et al., 2011; Marengo et al., 2011; Marengo and Espinoza, 2016).

2.2 Interannual variability in the Pacific and Atlantic region

2.2.1 Tropical Pacific: Different types of El Niño-Southern Oscillation (ENSO)

El Niño events in recent decades have been classified into the Eastern Pacific and Central Pacific El Niño based on the location of the maximum warming (Takahashi et al., 2011; Capotondi et al., 2015; Timmermann et al., 2018; Freund et al., 2019). The Eastern Pacific El Niño is the cannonical El Niño with the maximum warming in the eastern equatorial Pacific, while the Central Pacific El Niño presents the maximum warming in the central equatorial Pacific and is also referred as the El Niño "Modoki"(Ashok et al., 2007; Takahashi et al., 2011). In addition, atmospheric features of the two types El Niño are different over the tropical Pacific. Pronounced westerly anomalies associated with the Eastern Pacific are found over the entire span of the tropical Pacific basin; but for the Central Pacific, the westerly anomalies exist mainly from the western to the central tropical Pacific, with a more westward location of the rising branch of the anomalous Walker Circulation (Ashok et al., 2007; Timmermann et al., 2018; Freund et al., 2019), as is seen in Figure 2.2. On the other hand, the Eastern Pacific have a increased atmospheric water vapor and strong upward motion anomalies, mainly over the central and eastern Pacific. However, maximum water–vapor increase and enhanced convective activity are

located in the central Pacific for the Central Pacific (Ashok et al., 2007; Timmermann et al., 2018; Freund et al., 2019). Eastern Pacific pattern has a greater effect on the Peruvian coast, while Central Paific may also be relevant in the Andean or Amazon region of Peru through the tropical-tropical "teleconnections" (Takahashi et al., 2011).

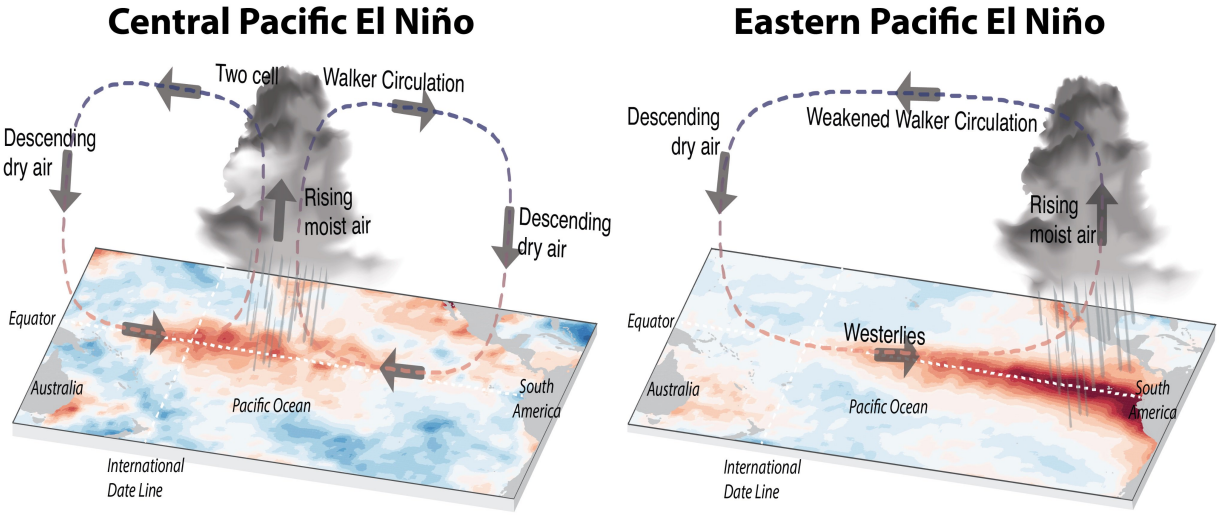

Figure 2.2: Schematic atmospheric and sea surface temperature conditions during Central (left) and Eastern Pacific events (right). From Freund (2018)

In this context, Takahashi et al. (2011) summarize the variability associated with anomalous surface warming in the Eastern and Central Pacific into the E and C index, respectively. They are calculated through Principal Components (PCs), and the linear correlation between them is low, making it possible to better distinguish the variability of each of these regions.

2.2.2 Tropical Atlantic patterns

In addition to the Pacific ocean, the Atlantic influences atmospheric circulation in the Amazon basin, since it is the main source of moisture in this region. Variability in the tropical Atlantic Ocean occurs on different time scales (Chang et al., 2006; Wainer et al., 2008; Deser et al., 2010; Brierley and Wainer, 2018). The most important frequency is the seasonal cycle, which is affected by monsoon forcing (e.g., South American monsoon system; SAMS) and by the ocean-atmosphere interaction that regulates the ITZC (Marengo and Nobre, 2009; Brierley and Wainer, 2018).

In this context, significant interannual variability in the tropical Atlantic shows two

main patterns. The first is a zonal pattern, well-known as tropical Atlantic variability (TAV), which is formed due to the influence of surface winds on equatorial ocean dynamics (Deser et al., 2010; Brierley and Wainer, 2018). This mode can affect precipitation over South America, where the positive phase is associated with SST anomalies in the eastern part of the tropical Atlantic, producing an increase in precipitation over northeast Brazil and western Amazonia (Brierley and Wainer, 2018). However, this pattern does not impact on the displacement of the Intertropical Convergence Zone (ITCZ) (Tokinaga and Xie, 2011).

The second pattern is an inter-hemisferic dipole (Atlantic Meridional Mode, hereafter referred to as AMM Deser et al., 2010; Brierley and Wainer, 2018), where the warm (cold) pole is associated with relaxed (intensified) trade winds (Nobre and Shukla, 1996). This pattern impacts significantly changes in the position and intensity of rainfall related to ITCZ. In other words, when the SST of one pole is abnormally warm relative to the other, the ITCZ moves to the warmer hemisphere, modulating the distribution of precipitation over the tropical Atlantic region (Marengo and Nobre, 2009; Brierley and Wainer, 2018).

2.2.3 South Atlantic Dipole (SAD)

Sea surface temperature variability over the South Atlantic Ocean presents a dominant mode of variability as a dipole (South Atlantic Dipole, SAD), with centers of action over the tropical and extratropical South Atlantic (Venegas et al., 1997; Bombardi and Carvalho, 2011; Nnamchi et al., 2011). This pattern is related to the strengthening and weakening of the South Atlantic Subtropical High, influencing in the SST fluctuations in a north–south dipole structure (Venegas et al., 1997).

On the other hand, SAD is associated with the first mode of interannual variability of circulation over South America (Robertson and Mechoso, 2000). Nnamchi et al. (2011) mentions that this mode is connected to an equatorial Atlantic pattern, the “Atlantic Niño”, subsequently confirmed by Lübbecke et al. (2018).

This pattern in the southern Atlantic is related to extreme rainfall in southeastern Brazil, as well as a delay in the onset of the rainy season over the Amazon (Marengo et al., 2001; Bombardi and Carvalho, 2011). In addition, the SST of the southern Atlan-

tic, together with the Pacific, influence the intensity and pission of the South Atlantic Convergence Zone (ZCAS) (Carvalho et al., 2004; Bombardi and Carvalho, 2011).

2.3 Decadal and Interdecadal variability of the Pacific and Atlantic Sea Surface Temperature

2.3.1 Pacific Decadal Oscillation

The Pacific Decadal Oscillation (PDO) is a variation of the Pacific climate that alternates warming (positive SST anomalies) and cooling (negative SST anomalies) phases every 20 to 30 years. The positive phase is characterized by increased warming in the eastern tropical Pacific and the eastern north Pacific, accompanied by cooling in the central north and western Pacific (Newman et al., 2016). PDO index is determined as the main empirical orthogonal function (EOF) of the monthly mean SST anomalies of the North Pacific (20°-70° N) (Mantua et al., 1997).

Despite the decadal variability be mainly associated with variability over the North Pacific, it also exerts strong control over the tropics. Indeed, the dominant pattern strongly resembles the global ENSO signature (Deser et al., 2004, 2010; Newman et al., 2016). This indicates that the PDO drives changes in rainfall over tropical South America due to a similar mechanisms, such as ENSO events.

2.3.2 Atlantic Multidecadal Oscillation

The Atlantic Multidecadal Oscillation (AMO) is a climate driver that impacts the SST of the North Atlantic Ocean. The different phases (warm and cold phases throughout the basin) oscillate in periods of every 50 to 70 years (Kerr, 2000; Sun et al., 2017). Because AMO is more pronounced over the North Atlantic, the AMO index is defined as the basin average of the Atlantic SST anomalies north of the equator (Enfield et al., 2001; Deser et al., 2010; Sun et al., 2018).

The persistent basin-scale SST anomalies associated with the AMO have significant impacts on climate in the North Atlantic, surrounding, and remote regions. In fact, several studies have suggested that there is an Atlantic-Pacific connection on low-frequency time

scales (Knight et al., 2006; Sun et al., 2017). In addition, the different phases of the AMO have been related to the displacement of the ITCZ on the multidecadal scale. Thus, the negative phases of AMO are related to wetter conditions in the Atlantic regions adjacent to the ITCZ, while the positive phases are associated with drier conditions (Knight et al., 2006).

2.4 Atmospheric circulation and its interannual influence into South America precipitation

2.4.1 Hadley and Walker circulation

The Hadley cell (Hadley, 1735) is a circulation that dominates the global circulation in equatorial and tropical latitudes. This cell extends from the Equator to a latitude of approximately 30° in both hemispheres. It is formed due to the thermal contrast between the Equator and the poles. The Hadley cell has a mass transport towards the Equator in the lower troposphere, due to the predominant flow of trade winds, and mass transport to the pole in the upper troposphere, also convergence in the equatorial region and subsidence in the subtropics (Wang and Fu, 2002; Grimm and Ambrizzi, 2009). The rise of warm air at the Equator is accompanied by the frequent formation of convective storms in the ITCZ, which in turn is the primary source of energy for this cell (Grimm and Ambrizzi, 2009).

The Walker cell, on the other hand, is a zonal tropical atmospheric circulation, driven by the longitudinal temperature gradient (Kousky et al., 1984; Yoon and Zeng, 2010; Barichivich et al., 2018). The main source of energy for the Walker circulation is the release of latent heat in the convection regions associated with ocean-atmospheric interactions. The strongest Walker cell is the Pacific cell (Grimm and Ambrizzi, 2009) and, as shown in Figure 2.3, occurs because the air rises over the western Pacific and is driven in high-level by the western wind, descending over the eastern Pacific and, finally, is closed by the trade winds in the lower troposphere. The Walker cell is induced by the presence of low (high) pressures in the south western (eastern) Pacific, undergoing inversions known as the ENSO. In other words, the Walker circulation is linked to the El Niño and La Niña cycles.

Hadley and Walker cells have significant impacts on the water cycle in the tropical

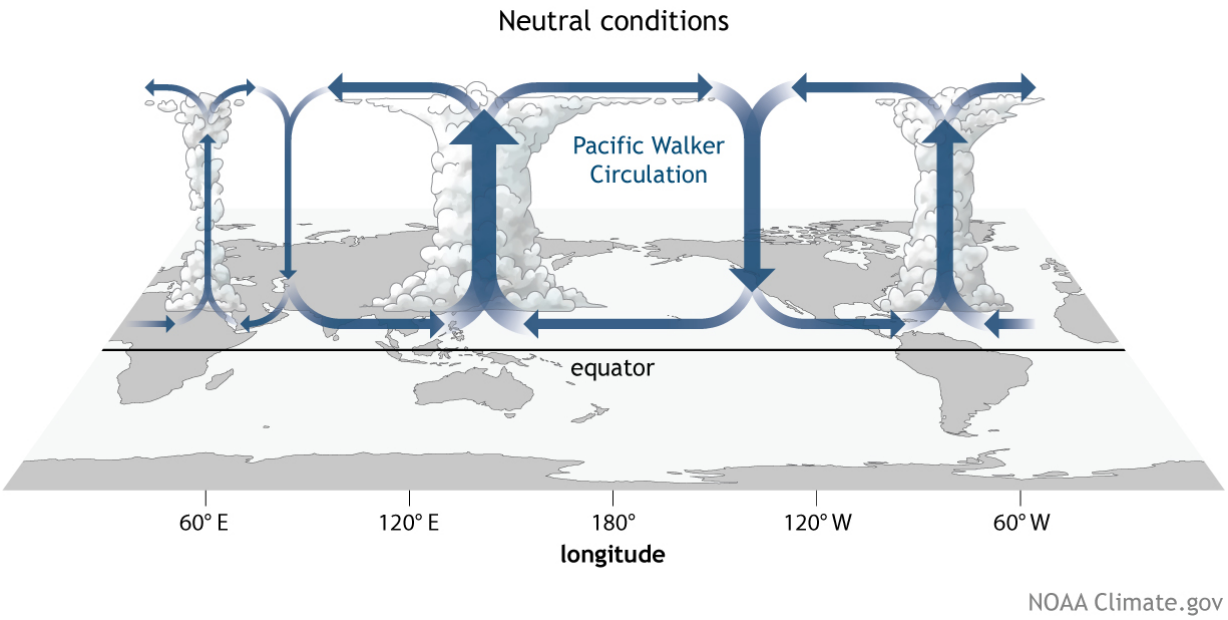

Figure 2.3: Generalized Walker circulation (December-February) during ENSO neutral conditions. From `https://www.climate.gov/`

region of South America and the Amazon Basin, resulting in increased or reduced rainfall over these regions (Yoon and Zeng, 2010; Barichivich et al., 2018). For instance, variations on the Walker cell caused by ENSO, trigger variations in rainfall over the Amazon Basin (Williams et al., 2005). However, an influence of ENSO on Atlantic SST could trigger a delayed rainy season (Yoon and Zeng, 2010). On the other hand, the strong warming of the tropical Atlantic and the cooling in tropical Pacific, strength the Walker circulation, causing an increase of floods in the Amazon Basin as recently documented by Barichivich et al. (2018). On the other hand, anomalous local Hadley circulation influences the South Atlantic determining interannual variability of precipitation in the Amazon Basin (Wang and Fu, 2002; Yoon and Zeng, 2010).

Chapter 3

Data and Methodology

This section explains the procedures that were used to develop the research based on the proposed objectives.The main used methodologies are summarized in Table 3.2, whit corresponding dataset input, the region and period covered by the data.

3.1 Data

3.1.1 Precipitation

TRMM

The Tropical Rainfall Mission Measurements (TRMM) is a joint mission between NASA and Japan's Space Agency. It was launched in November 1997 to monitor and provide information about precipitation and associated heat release in the tropics and subtropics (NASA and JAXA, 2001; Huffman et al., 2007; Braun et al., 2011). The instruments for precipitation that accompany this mission are the TRMM Microwave Images (TMI), the Precipitation Radar (PR), and the Visible and Infrared Scanner (VIRS). TRMM presents three levels of products according to the type of post-processing procedures from the received raw data. In level 3, it is the product 3B42, which has precipitation data with spatial resolution of 0.25 x 0.25 degrees from 50° N to 50° S. for all longitudes. Data are available from January 1998 to the present at every 3 hours, daily averages and monthly averages. This product was calibrated with data from surface stations with observed rainfall, thus being more precise (Huffman et al., 2010).

In April 2015, the spacecraft depleted its fuel reserves and stopped collecting informa-

tion. In June of the same year, it was launched back into the atmosphere while completing the transition from TRMM data to Mission Global Precipitation Measurement (GPM) data, its successor (Huffman, 2018). In this work, TRMM daily average rainfall data (`https://pmm.nasa.gov/data-access/downloads/trmm`) was considered for the 1998 to 2017 period and subsequently converted into monthly accumulated.

HyBAm

The HYBAM Observed Precipitation (HOP) (`http://www.ore-hybam.org/`) is a daily and monthly gridded rainfall database, compiled from 750 in situ stations within the Amazon Basin, which is obtained through several meteorological and hydrological services of the countries that cover the Basin. The quality control of this database was performed using the Regional Vector Method (RVM) and was interpolated using the Kriging method, at a resolution of 1.0 x 1.0 degree (Espinoza et al., 2009). The gridded data is available from 1980 to 2009.

GPCC

The Global Precipitation Climatology Centre (GPCC) is a gridded rainfall database derived from quality controlled station data and can be obtained in `https://www.esrl.noaa.gov/psd/data/gridded/data.gpcc.html`. GPCC has station records in 158 countries and 31 regional suppliers, including the Climate Research Unit (CRU), the Food and Agriculture Organization (FAO) and the Global Historical Climatology Network (GHCN), with around 85,000 stations worldwide (Sun et al., 2018). To collect rain products, GPCC considers a minimum of 10 years of uninterrupted data, and a monthly data is generated with a spatial resolution of 2.5 x 2.5, 1.0 x 1.0 and 0.5 x 0.5 degrees. Four products are available: 1) GPCC Full Data Version 7; 2) Climatology V2011; 3) Monitoring Product V4; and 4) GPCC First Guess Product (Becker et al., 2013; Sun et al., 2018). Of these, the first product, which is available for the 1891-2016 period, is used to assess interannual rainfall variability over South America, with a particular focus in the Amazon Basin. However, in a previous analysis of the data, random values of precipitation from before of 1940 is noticed. Because of this, in this study, the 1940-2016 period is used.

3.1.2 Atmospheric circulation

ERA-20C

The ECMWF twentieth century reanalysis (ERA-20C) is the first reanalysis product of the ERA-CLIM project, which provides global atmospheric three-dimensional data at 3-hour time increments throughout the 20th century (Poli et al., 2013, 2015, 2016). The spatio-temporal evolution of ERA-20C includes 91 atmospheric vertical levels between the surface and 0.01 hPa, four soil layers of the land surface, 25 frequencies and 12 directions of ocean waves. The ERA-20C is a public dataset and is available for downloading directly from `https://www.ecmwf.int/en/forecasts/datasets/reanalysis-datasets/era-20c`. For a description of the contents of ERA-20C, see Hersbach et al. (2015). In this research, winds (u, v, w) and specific humidity (q) data from ERA-20C is used.

3.1.3 Sea Surface Temperature (SST)

HadiSST

The Hadley Center Global Sea Ice and Sea Surface Temperature (HadISST) (`https://www.metoffice.gov.uk/hadobs/hadisst/`) is a gridded SST data obtained from the Met Office Hadley Center. Monthly SST data come from 1870 to the present, thus offering a database for more than 145 years. The spatial resolution is 1.0 x 1.0 degrees, varying in length from 180° W to 180° E (Chelton and Risien, 2016). HadISST is based on SST data from the Marine Data Bank (MDB), which is compounded mainly by ship track measurements, and a combination of adjusted satellite-derived and in situ SST data from 1982 onward, using an optimal interpolation of reduced space. International Comprehensive Ocean-Atmosphere Data Set (ICOADS) were also used from 1871-1995 period, where there were no MDB data. A "bucket correction"was applied to the SST for 1871-1941 (Rayner et al., 2003; Deser et al., 2010).

PIRATA SST data

The Prediction and Research Moored Array in the Tropical Atlantic (PIRATA) is a program supported by France, Brazil and the USA. PIRATA consists of a network of buoys providing meteorological and oceanographic data (Bourlès et al., 2019). This buoy network started in 1997 and presents real-time data, available at `https://www.pmel.noaa.gov/`

Table 3.1 - Geographical coordinates of the buoys used in this investigation obtained from the PIRATA network.

		Latitude	**Longitude**
TNA	Station1	8° N	38° W
	Station2	12° N	38° W
TSA	Station1	10° S	10° W
	Station2	0°	23° W

`gtmba/pmel-theme/atlantic-ocean-pirata`. Data from two buoys located in the North Tropical Atlantic region and two buoys located in the South Tropical Atlantic region were used to compare results obtained by HaDiSST. The coordinates of the buoys are used in Table 3.1 and its location is in Figure 3.1.

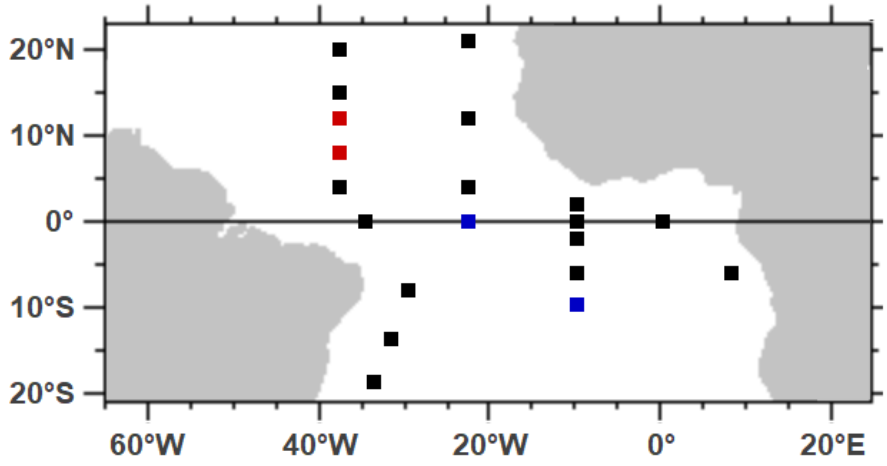

Figure 3.1: Location of the PIRATA network buoys and the buoys used for the region of TNA (red) and TSA (blue).

3.1.3.1 SST index

E index and C index

In this study, we used the eastern (E) and central (C) El Niño-Southern Oscillation (ENSO) index (available in `http://www.met.igp.gob.pe/variabclim/indices.html`). These indices are documented in detail in Takahashi et al. (2011). Computation of the central Pacific (C) and the eastern Pacific (E) indices extend from 1880 to the present.

Pacific Decadal Oscillation (PDO) index

The Pacific Decadal Oscillation (PDO) is a pattern of Pacific climate variability with duration similar to El Niño (Deser et al., 2010)(Zhang et al. 1997). The PDO is defined by the first spatial pattern (EOF) of anomalies of SST in the North Pacific, from the pole to 20° N. Two PDO databases are available: 1) the monthly PDO index from 1900-present, maintained by Mantua et al. (1997); and 2) the monthly PDO index from 1854-present by NOAA-NCDC. Due to the extended data period, the NOAA index (`https://www.ncdc.noaa.gov/teleconnections/pdo/`) is used for this study.

Atlantic Multidecadal Oscillation (AMO) index

The Atlantic Multidecadal Oscillation (AMO) index is obtained from PSD/NOAA (`https://www.esrl.noaa.gov/psd/data/timeseries/AMO`). There are two types of AMO index: 1) based on Trenberth and Shea (2006) and HadISST; and 2) and the AMO index which comes from the NOAA-ESRL, based on Kaplan SST. In this investigation it is used the NOAA index. The AMO index availability is from 1861 until June 2014.

The chosen index is based on the average anomalies of sea surface temperatures (SST) in the North Atlantic, between 0 and 70° N, detrending and smoothing with 1-2-1 filter, using the Kaplan SST data set (Enfield et al., 2001). These Kaplan SST data were produced using various statistical methods such as Optimal Interpolation (OI), Kalman Filter (KF) forecast, KF Analysis and Optimal Smooth (OS) (Kaplan et al., 1998).

3.2 Methodology

3.2.1 Cluster Analysis

Cluster analysis is a multivariate statistical technique that is based on classifying objects or variables forming groups (clusters) that are as homogeneous as possible within themselves and heterogeneous with each other (Wilks, 2011). This method considers the distances as a measure of similarity or dissimilarity. The most common measure is the Euclidean distance, which consists in determining the distance between two k-dimensional points (Wilks, 2011). In this study the city-block method is considered. The city-block approach takes into account the sum of distances in each dimension, reducing the effect of the outliers. The city-block distance is defined as follow

$$d_{i,j} = \left[\sum_{k=1}^{K} |x_{i,k} - x_{j,k}| \right]$$

where x_i and x_j are two points in the k dimension ($k = 1, \ldots, K$) (Wilks, 2011).

There are two methods for clustering: hierarchical and non-hierarchical. The hierarchical clustering method groups the objects considering individual clusters that are grouped into pairs of clusters according to the similarity between them, merging them into a higher group at each step until obtaining a single cluster (Xu and Wunsch, 2005; Wilks, 2011). The output of the hierarchical method is a dendogram or tree diagram, which illustrates the progress of the cluster analysis. The advantage of this method is that it determines the number of clusters into which the variable should be divided, since the dendogram can be cut into a desired number of clusters according to the similarities between them. The main disadvantage of this method is that the element that is assigned to an initial group cannot be reassigned (Wilks, 2011).

The non-hierarchical clustering approach (e.g., k-means) needs as input the final number of clusters, which can be considered as its main disadvantage (Wilks, 2011). The k-means approach is an iterative procedure that is commonly used to identify clusters in a given data set. In this study, the algorithm to decide homogeneous rainfall regions is applied. K-means use as an input the normalized monthly precipitation, which comes from three different datasets. Finally, the Silhouette Index (SI) is used to determine the quality of the formed clusters. This index evaluates the similarity of a data with other data of its own cluster, and the dissimilarity with data from other clusters. The SI is defined as follows,

$$SI_i = \frac{b\,(n) - a\,(n)}{max\{a\,(n)\,, b\,(n)\}}$$

where n is the evaluated point, and *a(n)* is the mean distance between n and all points of its cluster, and *b(n)* is the mean distance between n and all points of the nearest cluster (Rousseeuw, 1987). The values of this index range between -1 and 1, where values close to 1 indicates that the element has a good assignment in its corresponding cluster (Rousseeuw, 1987).

3.2.2 Monthly anomalies calculation

To analyze the interannual variability of the variables (SST, precipitation, zonal wind, meridional wind and the vertical velocity omega), trends of the monthly values are removed, and subsequently, the seasonal and annual cycle, so just the series anomalies remain.

Detrending data

To remove the trend of the series, first, the change in the series was calculated through the detection of shifts in the mean of the series using the "changepoints" method proposed by Rodionov (2004) and following Killick et al. (2012). The points detected were obtained by changes in the series of the common area. Subsequently, the trend for each period between the changepoints was eliminated.

Removing Seasonality

The seasonal and annual cycle of the detrended data is removed by the difference between the monthly data of each year and the monthly average (monthly climatology) (Wilks, 2011). The 1979-2015 period was taken as the base period for climatology.

3.2.3 Empirical Orthogonal Function (EOF)

Principal Component Analysis is used to investigate the interannual variability of the SST in the Atlantic region. The covariance matrix is considered as an input for the EOF analysis. EOFs are the eigenvectors of the covariance matrix, and they form an orthogonal spatial structure. PCs are the principal components, orthogonal in time; they show how the spatial structure varies over time, and they are obtained by projecting the data matrix in the EOFs.

The EOF modes are calculated from the monthly SST anomalies, considering the 1870-2017 period. For the analysis, it is considered the first (PC1) and the second mode (PC2) or the dominant mode. Finally, a correlation between the PCs and the monthly SST anomalies is computed for each region, to verify the degree of association (i.e. spatial structure) of the modes obtained through the EOFs and the SST anomalies.

3.2.4 Atlantic index calculation

The EOF modes were calculated from monthly SST anomalies for the different Atlantic regions (3.2). The first region covers the Tropical North Atlantic (TNA) Ocean, between 5.5° N - 23.5° N. The second region considered in this study corresponds to the Tropical South Atlantic (TSA) from the Equator to 20° S. Finally, the third region corresponds to the Subtropical South Atlantic (STSA), bounded by 20° S to 40° S. These indices were generated from PC1 for each region, considering spatial anomalies of the SST within the mentioned regions, using the HadISST data from 1871 to 2015 period. The results and analysis of the calculation of these indices will be discussed in the next chapter.

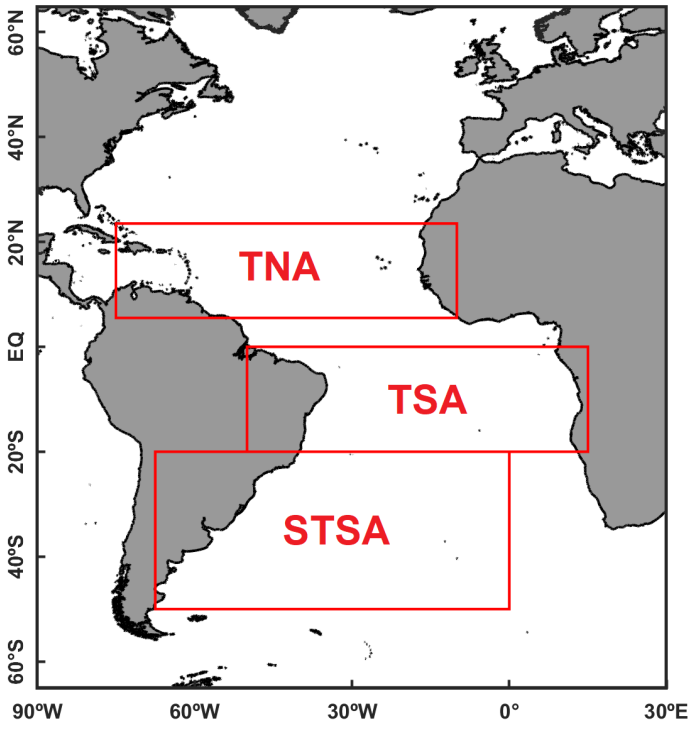

Figure 3.2: Location of the TNA, TSA and STSA areas.

3.2.5 Wavelet Transform

The wavelet transform is a mathematical technique used to detect the time structure of multi-scale variations (Lau and Hengyi Weng, 1995). This technique can transform a one-dimensional time series into a two-dimensional, in the time-frequency domain (Torrence

and Compo, 1998; Silva et al., 2019).

In this research, the wavelet transform is applied to monthly PC1 data for each Atlantic region for the 1880–2017 period, to observe the dominant oscillation modes of this series in time. The statistical significance of the wavelet transform is estimated using Monte Carlo methods, using a significance level of 5%. Wavelet has a cone of influence (COI), marked by a black thin line, where values outside the COI is the result of a significant contribution of zero padding at the beginning and the end of the time series (Torrence and Compo, 1998).

3.2.5.1 Cross-wavelet and wavelet coherence

The cross-wavelet is a technique that characterizes the interaction between the wavelet transform of two individual time-series. Wavelet coherence is defined as the square of the cross-spectrum normalized by the individual power spectra (Torrence and Compo, 1998) and is especially useful for highlighting the time and frequency intervals where two phenomena (or time series) have strong interactions. In other words, is the correlation between two time series in the time frequency space. Wavelet coherence is used to observe the interactions between the Atlantic regions (TNA, TSA and STSA), and the interactions between Atlantic and Pacific regions. As mentioned above, 5% of significance level is used.

3.2.6 Power spectrum

The power spectrum is commonly defined as the Fourier transform of the autocorrelation function, and provides information on the power of a signal (energy per unit time) that falls within given frequency ranges. The power spectrum was applied to the filtered time series of the Atlantic PC1 (TNA, TSA and STSA). A Lanczos filter was applied to eliminate high frequency (frequencies less than one year). As in the wavelet technique, Monte Carlo test is used to determinate the significance, at 5 % of significance level.

3.2.7 Pearson's Correlation

Correlation involves the measurement of association or relationship between two variables. In other words, it is a measure of the changes in one variable by the influence of the

changes in the other variable. The association can be positive, if both variables change in the same direction, or negative, if they change in opposite directions, and it is determined by correlation coefficients. The Pearson correlation coefficient (r) is given by (Wilks, 2011):

$$r = \frac{\frac{1}{n-1}\sum_{i=1}^{n}[(x_i - \bar{x})(y_i - \bar{y})]}{[\frac{1}{n-1}\sum_{i=1}^{n}(x_i - \bar{x})^2]^{1/2}[\frac{1}{n-1}\sum_{i=1}^{n}(y_i - \bar{y})^2]^{1/2}}$$

where x_i and y_i are the variables observed at time i, respectively SST and precipitation in this case; $\overline{x}$ and $\overline{y}$ are the arithmetic means of the time series of each variable, and n is the amount of data that have the two time series.

3.2.7.1 Moving Correlation Analysis between El Niño and Atlantic indexes

This method calculates the Pearson correlation coefficient on a moving window for two or more variables, and serves to analyze the dynamics of the correlation over time.

In this investigation, the 5, 7 and 10 years moving correlations are determined to assess the dynamics of the association between the different indices, corresponding to the Pacific and the Atlantic regions.

3.2.8 Spatial correlation between precipitation and El Niño and Atlantic indices

The influence of the main regions of the Pacific and the Atlantic oceans on extreme precipitation events is determined by the calculation of Pearson's correlation. E and C indices, for the Pacific region, and the indices calculated for the Atlantic were used, and each of them was correlated with the precipitation of TRMM, HyBAm and GPCC data, for the 1998-2009 period. Subsequently, Pearson's correlation statistical significance test was applied, at a 95% level of significance. Correlations were made for each wet (Dec-Feb), dry (May-Sep) and transition (Oct-Nov and Mar-Apr) season of the Amazon basin.

3.2.8.1 Linear regression technique

The relationship between the oceanic Atlantic and Pacific indices and the dynamical fields over South America (and Amazon Basin) is assessed through a linear regression

technique. The linear regression describes the linear relationship between two variables, and is used to represent the evolution of disturbances over time. The regression procedure chooses of the squared-error criterion, that means least-squares regression, or ordinary least squares (OLS) regression (Wilks, 2011).

The linear regression analysis was calculated between the time series and the raw dynamical fields (e.g., unfiltered winds, divergence) for each global grid point, at each pressure level. The statistical significance of these results is assessed based on a two-tailed significance t-student test, which considers the correlation coefficients and an effective number of independent samples (freedom) based on the decorrelation timescale, as in Livezey and Chen (1983). Results are considered significant at the 95% level or greater.

3.2.9 Composites of precipitation

Composites are used to analyze the characteristics of a variable that can be supported by some phenomenon or event. For this, cases are selected, and the statistics of the variable are calculated only for these cases.

In this work, precipitation composites were made considering the warm and cold phases of the PDO and AMO. For this, PDO and AMO index was smoothed by 121-month moving average, where positive values correspond to warm PDO/AMO phase, and negative values are the cold PDO/AMO phase. Consequently, precipitation anomalies are averaged for each period. Composites were made for each wet, dry and transition season in the Amazon basin (Oct-Nov, Dec-Feb, Mar-Apr, May-Set).

Table 3.2 - Methodologies, Input Datasets, Outputs and Period of Datasets.

Section	Methodology	Dataset Input	Region	Dataset Output	Period
South America Precipitation	**Clustering**	TRMM GPCC	South America		1998-2016
	Regionalization	GPCC	South America		1981-2016
The SST Variability over the Atlantic Ocean	**Climatology**	HadiSST	Atlantic Ocean		1870-2017
	Monthly SST Anomalies	HadiSST	Atlantic Ocean		1870-2017
	EOF/PC (Atlantic Index)	HadiSST	TNA TSA STSA	TNAi TSAi STSAi	1870-2017
	Wavelet	TNAi TSAi STSAi			1870-2017
	Power Spectrum	TNAi TSAi STSAi			1870-2017
Relationship between Atlantic and the Pacific SST	**Moving correlation**	E/C index TNAi, TSAi, STSAi			1880-2017
	Cross-wavelet	E/C index TNAi, TSAi, STSAi			1880-2017
Influence of the SST on the precipitation	**Spatial correlation**	GPCC E/C index TNAi, TSAi, STSAi	South America		1940-2010
	Composites of precipitation	GPCC E/C index TNAi, TSAi, STSAi	South America		1940-2010
	Horizontal regression	ERA-20C (u,v,q) E/C index, TNAi, TSAi, STSAi	12° W-0° 55° S-55° N		1940-2010
	Vertical regression	ERA-20C (u,w,q) E/C index	5° S - EQ		1940-2010
		ERA-20C (u,w,q) TNAi, TSAi, STSAi	45° W - 55° W		1940-2010

Chapter 4

Results and Discussion

4.1 Rainfall regionalization in South America

Most of the regional atmospheric systems which cause precipitation over South America at seasonal time scales are widely discussed in previous works (e.g. Figueroa and Nobre, 1990; Rao and Hada, 1990; Satyamurty et al., 1998; Zhou and Lau, 1998; Vera et al., 2006; Poveda et al., 2006; Garreaud et al., 2009; Machado et al., 2014; Viale et al., 2019, among others). The main atmospheric systems that influence precipitation over South America are summarized in Figure 4.1. However, an easy way to describe how different atmospheric systems affect certain regions is, in fact, through the regionalization. Considering that the regionalization of precipitation regime is essential for the optimum design and management of water-related activities, many previous works assessed it, considering only a regional domain. For instance, in the Brazilian Amazon (Santos et al., 2015), in the Amazon Basin (Espinoza et al., 2009; Mayta et al., 2020), in Peruvian Pacific coastal region (Rau et al., 2017), Northeast of Brazil (Uvo and Berndtsson, 1996), Argentina (Aliaga et al., 2017), in southern Andes (Masiokas et al., 2019), in South America (Reboita et al., 2010), among others. Thus, through different precipitation datasets with a homogeneous spatial distribution, our first aim is to regionalize precipitation in the entire South America region.

4.1.1 South America precipitation climatology with focus on the Amazon Basin

Figure 4.2 shows the mean precipitation for the 1998-2009 period, based on observed precipitation over South America and the Amazon Basin as a comparison between TRMM (4.2, column a), HyBAM (4.2, column b) and GPCC (4.2, column c) datasets. Rainfall in

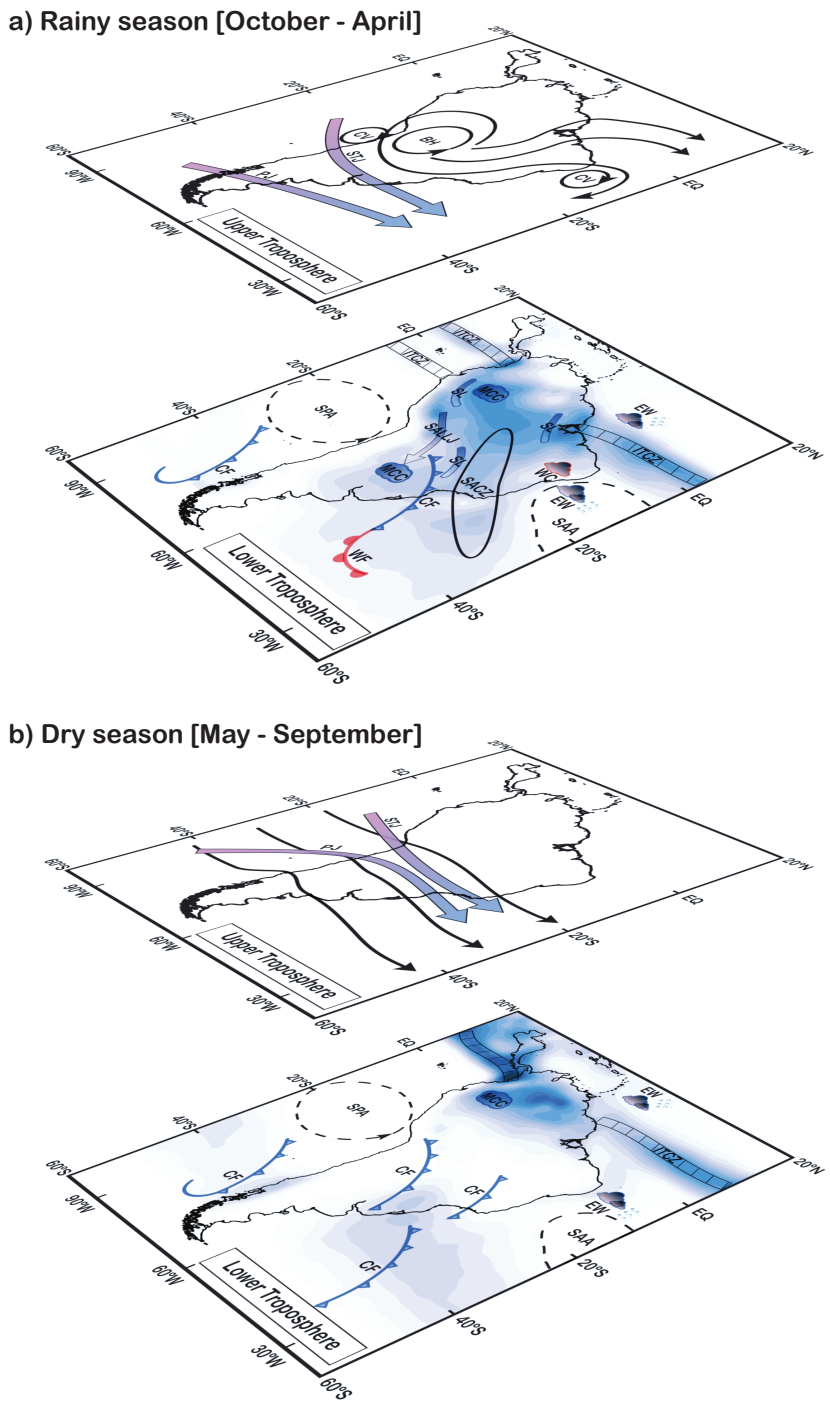

Figure 4.1: Schematic depiction of the main atmospheric circulation features over the South America region: a) October to April and, b) May to September period [Adapted from Satyamurty et al. (1998) and Machado et al. (2014)]. [**SL** = squall lines; **MCC** = mesoscale convective complex; **SALLJ** = South America low-level jet; **CF** = cold front; **WF** = warm front; **WC** = warm cloud; **EW** = Easterly Waves; **SPA** = South Pacific anticyclone; **SAA** = South Atlantic anticyclone; **STJ** = subtropical jet; **PJ** = polar jet; **CV** = cyclonic vortex; **BH** = Bolivian high].

South America is mainly modulated by the active phase of the South America Monsoon System (SAMS; Zhou and Lau, 1998; Vera et al., 2006) during the austral summer and the absence of the SAMS during the austral winter.

During the onset of the SAMS in the Amazon Basin (Oct-Nov), it is characterized by a maximum rainfall over the Northwest of South America (Fu et al., 2013). It is observed that maximum rainfall on South America is located on the west coast of Colombia, due to the positioning of the Intertropical Convergence Zone (ITCZ) and high SST on the coast (Figueroa and Nobre, 1990) such as observed in the TRMM data. Over the Amazon Basin, the northwestern region of the basin (located on the border between Brazil, Perú, Venezuela and Colombia) also shows maximum precipitation, observed mainly in HyBAm and GPCC database (Figure 4.2b,c). This region is characterized by an undefined dry period, but shows maximum annual average precipitation values (Fisch et al., 1998; Espinoza et al., 2009). During this period, it is also observed a northwest to southeast band of precipitation over South America, associated with the South Atlantic Convergence Zone (SACZ) which starts in October (Figueroa and Nobre, 1990; Nieto-Ferreira and Rickenbach, 2011).

During the peak of the SAMS (Dec-Feb), the region with maximum precipitation is located in the central region of South America, including the west, central and south of the Amazon Basin (Wang and Fu, 2002), and the southeastern Brazil, observed in all precipitation datasets (TRMM, HyBAm and GPCC). The ITCZ moves southward, as seen in TRMM data. The moisture flux from the Tropical Atlantic is carried off to the Amazon basin. This flux and the recycled water vapor in the Amazon are transported to the southeast of Brazil through the South America low-level Jets (SALLJ), located along the eastern of Andes (Marengo, 2004). When this flow converges with the winds brought by the South Atlantic Anticyclone (SAA) in lower levels of the atmosphere, deep convection is generated and the SACZ (Gan et al., 2009; Reboita et al., 2010). The SACZ is usually more intense in the summer months (Carvalho et al., 2004; Garreaud et al., 2009; Marengo et al., 2008; Gan et al., 2009; Reboita et al., 2010), causing intense precipitation in the Southeast Region of the country, both for TRMM and GPCC datasets.

The end of the SAMS (Mar-Apr) is characterized by the presence of the ITCZ in its southernmost position ($\sim 2^\circ$ S) (Reboita et al., 2010), as can be seen in TRMM data (Figure 4.2a); becoming the most important system for rainfall in the northeast region of

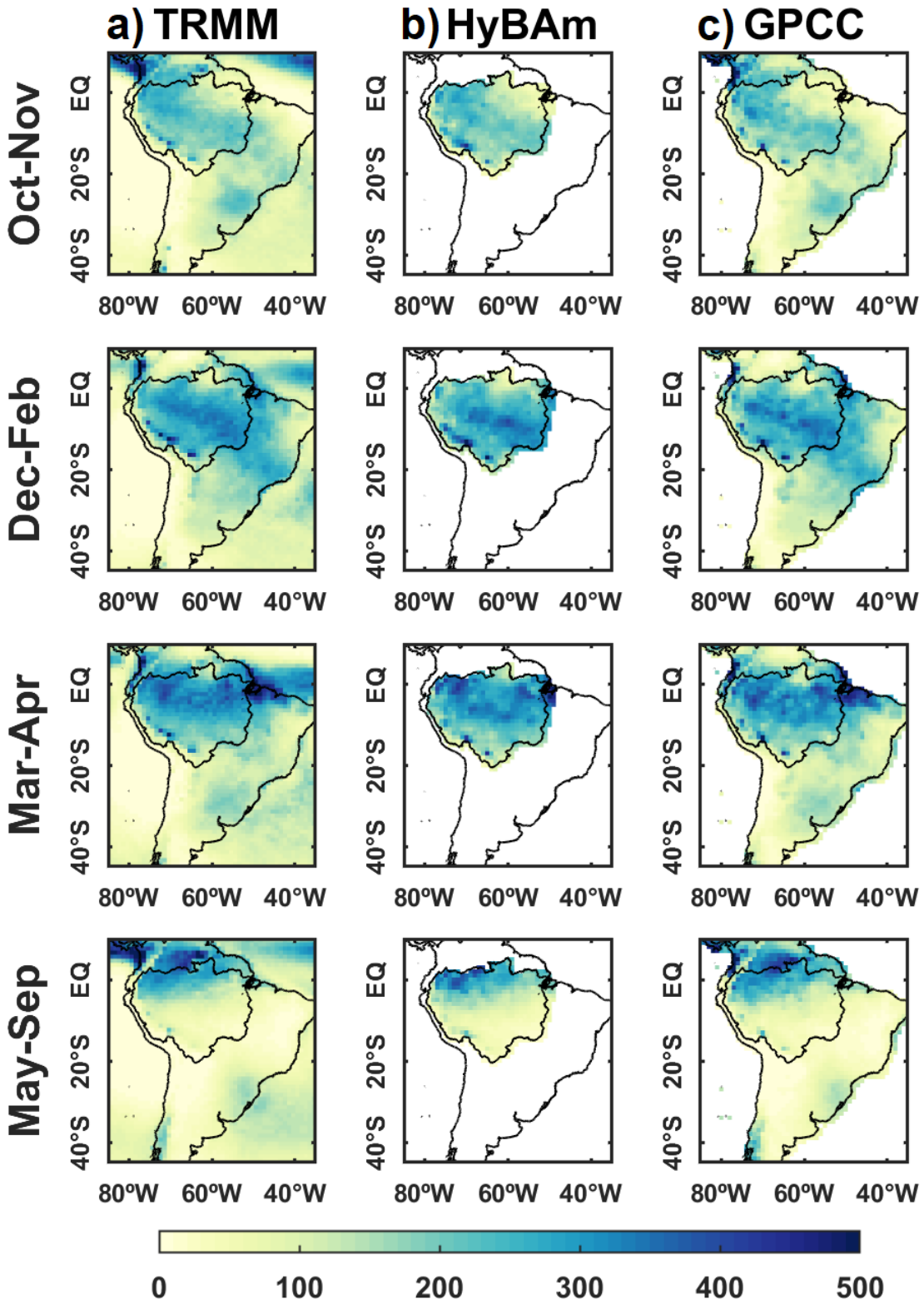

Figure 4.2: Mean precipitation (mm) for the onset (Oct-Nov), peak (Dec-Feb) and the end (Mar-Apr) of the SAMS, and for SAMS absence period (May-Sep) for the 1998-2009 period. Column a) TRMM; column b) HyBAm; column c) GPCC.

Brazil (Melo et al., 2009; Reboita et al., 2010) and the north-central of Amazon basin. Furthermore, the squall lines, a mesoscale convective system, and the sea breeze, a mesoscale mass circulation, which are more intense in this period, contribute to the increase in rainfall along the coast northeast of Brazil (Figueroa and Nobre, 1990; Marengo and Nobre, 2009), noticeable in both TRMM, HyBAM and GPCC data. Besides, the topography of the Andes acts as a barrier for the air masses from the east, generating precipitation due to the orographic effect (Figueroa and Nobre, 1990), as seen in the three databases of Figure 4.1 (third line).

The migration of the ITCZ to the north is observed in May-September period (see Fig. 4.1), observed in the TRMM database (Figure 4.2a). The maximum of precipitation is located in the north part of South America, region which belongs to the Northern Hemisphere (NH). North of the Amazon Basin is located in NH, reason why it shows this features and begin its rainy season in this period (Marengo and Nobre, 2009; Reboita et al., 2010; Mayta et al., 2020). However, there are some regions (south of Chile, clearer for TRMM and GPCC, Uruguay, and South of Brazil) with considerable precipitation during this period, mainly associated with the passages of cold frontal systems (Berbery and Barros, 2002; Viale et al., 2019).

4.1.2 Precipitation Regionalization of South America

Figure 4.3a shows the output of the final merging cluster after a hierarchical cluster analysis, in the form of the tree diagram. The number of clusters is chosen considering the distances between merged clusters, specifically when a markedly jump is observed (Figure 4.3b) (Wilks, 2011).

We will start considering five clusters (Figure 4.4a), where a proper separation for SA precipitation is observed. Nevertheless, regions located in the Northern Hemisphere are, apparently, poorly divided. Indeed, most of the regions located there depict homogeneous precipitation throughout the year, but with different atmospheric systems producing rainfall themselves. The average SI for TRMM and GPCC is 0.29 and 0.29, respectively. Considering six clusters (Figure 4.4b) Cluster 5 (C5) is divided into two regions. One portion is localized in the equatorial region and the second, covers the northern position of SA (C6), and their regimes are influenced by different atmospheric factors, such as the

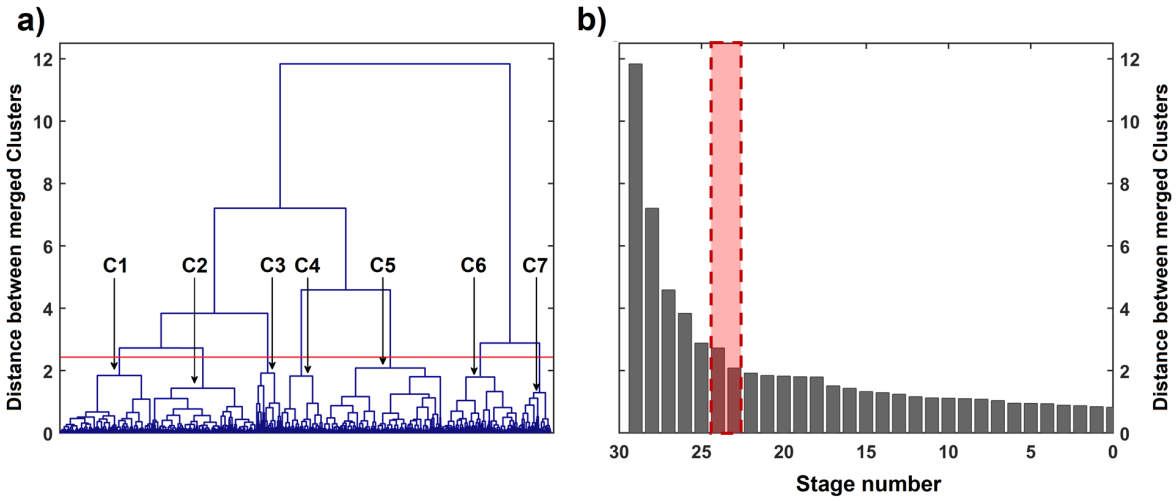

Figure 4.3: Dendrogram (a) and the corresponding plot of the distances between merged clusters as a function of the stage of the cluster analysis (b) for the precipitation data. Normalized data have been clustered according to the minor-linkage criterion. The distances between merged groups appear to increase markedly after 23 stages, which for these data would yield seven clusters, respectively.

ITCZ position. However, the average SI show lower values (0.25 and 0.24 for TRMM and GPCC, respectively) when compared to the 5-clusters choice (Figure 4.3.a).

However, considering seven clusters, C1 is divided into the west and east (see Figure 4.5), which represents a notable difference in the precipitation regime, since this area (C2) is more arid than the adjacent area (C1). Furthermore, the average SI shows similar and relatively high values for the three databases (0.27, 0.26 for TRMM, GPCC, respectively). Finally, when 8 clusters are considered for the analysis, it appears a region which covers Uruguay and south of Brazil (Figure 4.4c). Nonetheless, the SI shows lower valuesfor this choice: 0.27 for TRMM and 0.21 for GPCC. It should be noted that the number of sub-regions may be greater, which only depends on the degree of detail required. Therefore, based on the previous analysis (Figure 4.3), and considering the clustering and better SI value (Figure 4.4), seven clusters are finally considered (Figure 4.5).

Thus, Figure 4.5 shows the spatial distribution of the mean annual total precipitation from TRMM (left) and GPCC (right) for the seven clusters considere.The three databases show similar classification, despite of their different data resolution. For instance, Cluster 1 covers the following regions: Central SA, northeastern forests of Brazil, and the north and central region of Argentina. On the other hand, Cluster 2 includes the West part of

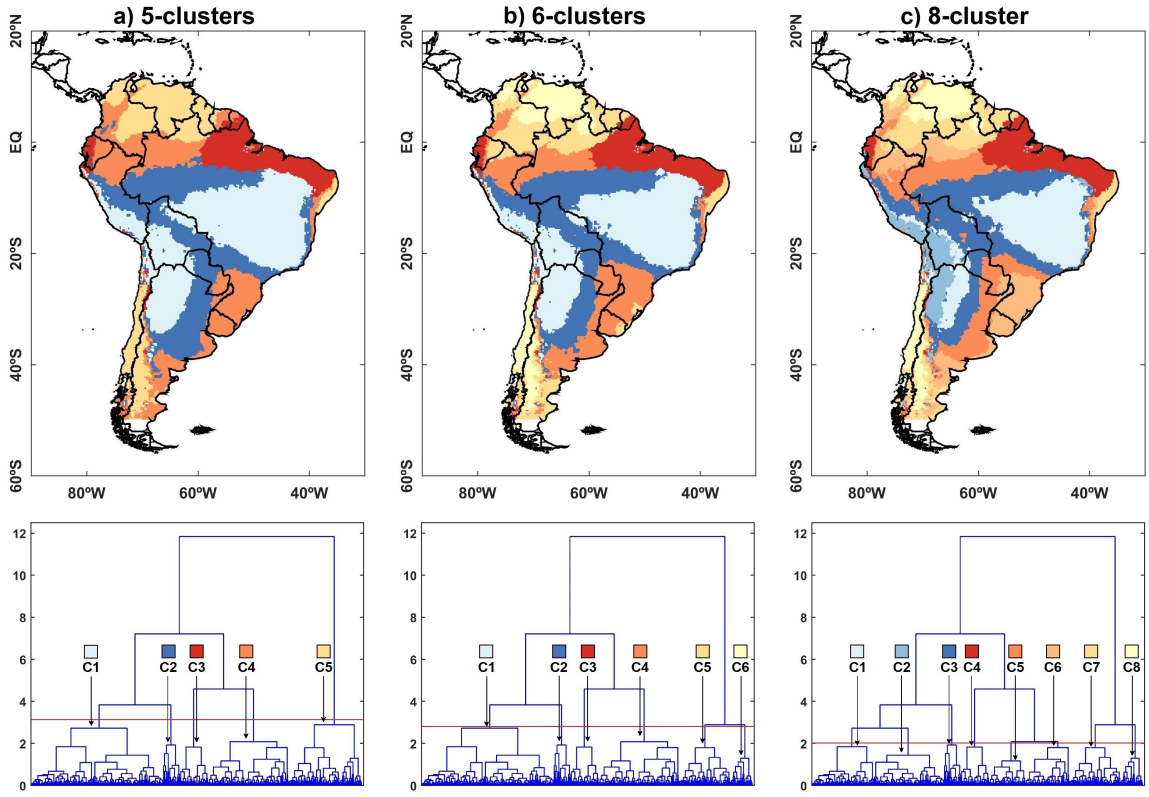

Figure 4.4: Precipitation regimes of South America assessed by non-hierarchical cluster analysis (k-means). Spatial rainfall distribution (upper panels) and their corresponding tree diagram (bottom panels) for (a) 5 clusters, (b) 6 clusters, and (c) 8 clusters.

SA, including the Peruvian coast, western Bolivia and northwestern Argentina. Cluster 3 covers a broad region, where the South American Low-Level Jet (SALLJ) core and northeast and southeast wind trades act during the SAMS.

Cluster 4 shows that the Northeast region of Brazil has the same rainfall regime as the coastal region of Ecuador and part of the northern highlands of Peru. Likewise, Cluster 5 indicates similar rainfall regime in the rainforest between Peru and Brazil, the coast of Colombia and the southeastern region of SA.

Finally, Clusters 6 and 7 cover the North and Southwest of SA, including the southern tip of SA. According to Reboita et al. (2010), these regions (South and Southwest of Argentina, and Central and Southern Chile) show maximum rainfall in winter and minimum in summer, due to ASPS, fronts and cyclogenetic activity; while the north of SA presents this regime due to its position in the Northern Hemisphere.

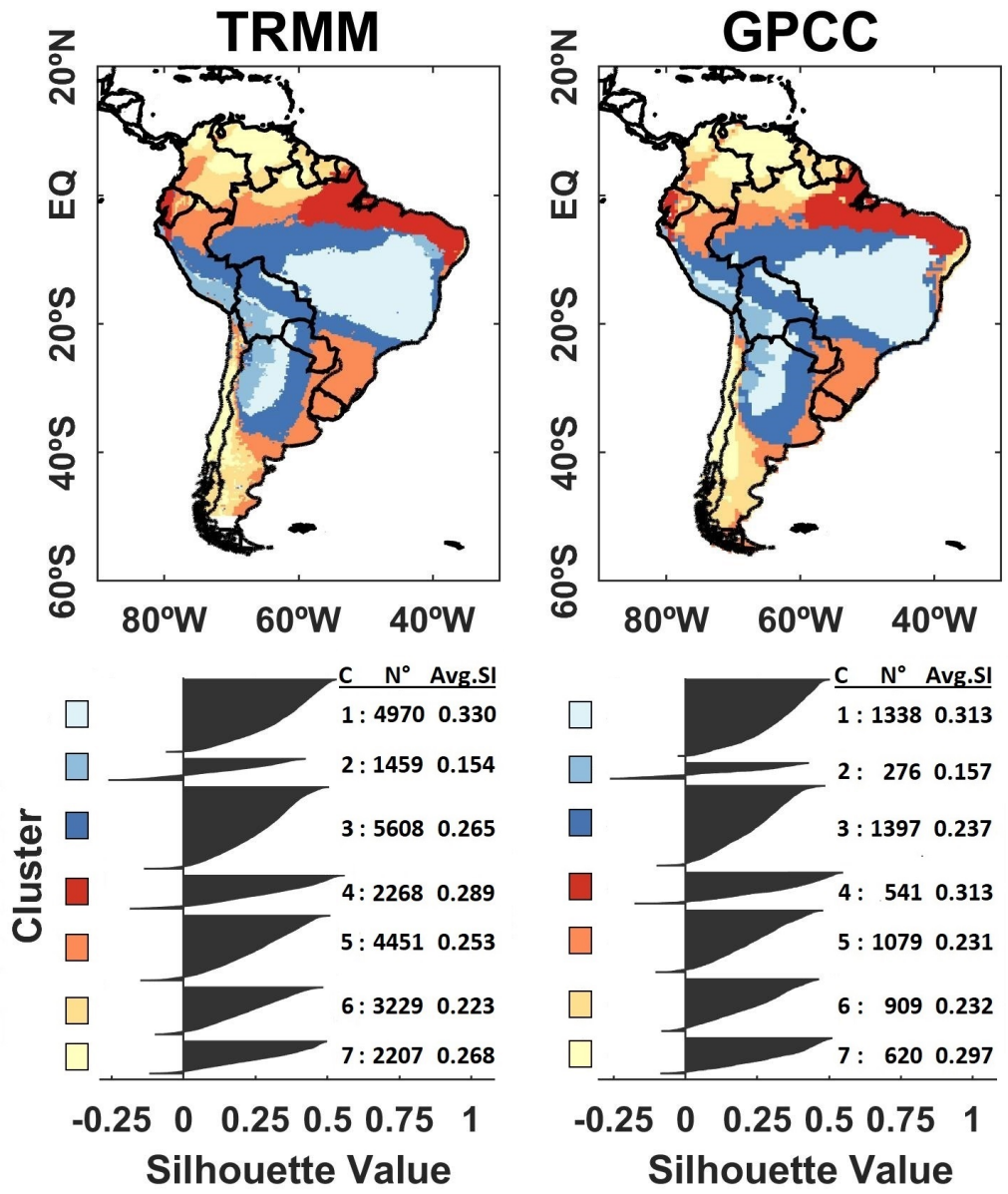

Figure 4.5: Precipitation regimes of South America assessed by non-hierarchical cluster analysis (k-means), when seven cluster are considered. Upper panels: spatial rainfall distribution. Botton panels: the Sihouette Index graph, and table pointing to the number of points for each cluster and SI value are shown for the TRMM-3B42 (left column) and GPCC (right column), respectively.

Although the SI values are not so high, their spatial separation suggests that they are likely due to different physical mechanisms. According to these results, a more exact division from this is made. They are separated as different regions to the data of the same cluster that are located in very different regions. Therefore, Clusters 4, 5, 6 and 7, located in two or three different regions, are considered as different regions over South America.

From here on 12 regions with similar rainfall regimes in SA are considered, whose main features and heterogeneity are well-captured.

4.1.2.1 *Linking the 12 South America spatial and temporal precipitation regimes with the main atmospheric system that drive them*

SA is divided into 12 regions (Figure 4.6) based on the cluster analysis described in the previous section. Each region depicts similar rainfall regime, which is under the influence of the same atmospheric circulation systems. Because of it is essential for future discussions in this work, this section focuses in the description of the rainfall regimes of each region and their associated atmospheric systems which produce precipitation.

Region 1

Region 1 is located in the extreme north of SA (Venezuela and North/Northeast of Colombia) and shows its maximum precipitation during, approximately, the austral winter (May-August), and minimum in the austral summer (December-March), with rainfall ranging between 40 and 300 mm/month (Figure 4.6). As Region 1 is completely located in the Northern Hemisphere, its precipitation regime follows the northern monsoon period. Region 1 is under the influence of trade winds (see Fig. 4.1), which are surface winds from the northeast (in the Northern Hemisphere) and from the southeast (in the Southern Hemisphere), forced into the tropics by the circulation of the Hadley cell and the Coriolis effect. Likewise, the ITCZ band, when migrating from south to north, reaches its northernmost position ($\sim$10° N over the Atlantic) in the austral winter (Hastenrath, 1991; Satyamurty et al., 1998; Poveda et al., 2006). The ITCZ becomes, therefore, one of the most important precipitation systems over the Region 1. In addition, when the ITCZ is in its southernmost position, between summer and autumn ($\sim$4°S on the Atlantic) (Hastenrath, 1991), its influence on Region 1 is negligible.

In short time-scale, Riehl (1977) and Riehl et al. (1977) mention the existence of a trough at high levels (200 hPa) with east-west orientation over the Caribbean area and with a period of 2-3 days, causing severe precipitation. On the other hand, the Easterly Waves (EW), which are wind disturbances in the middle and lower troposphere, propagate from West Africa to the Tropical Atlantic triggering rainfall in Region 1 (see Fig. 4.1).

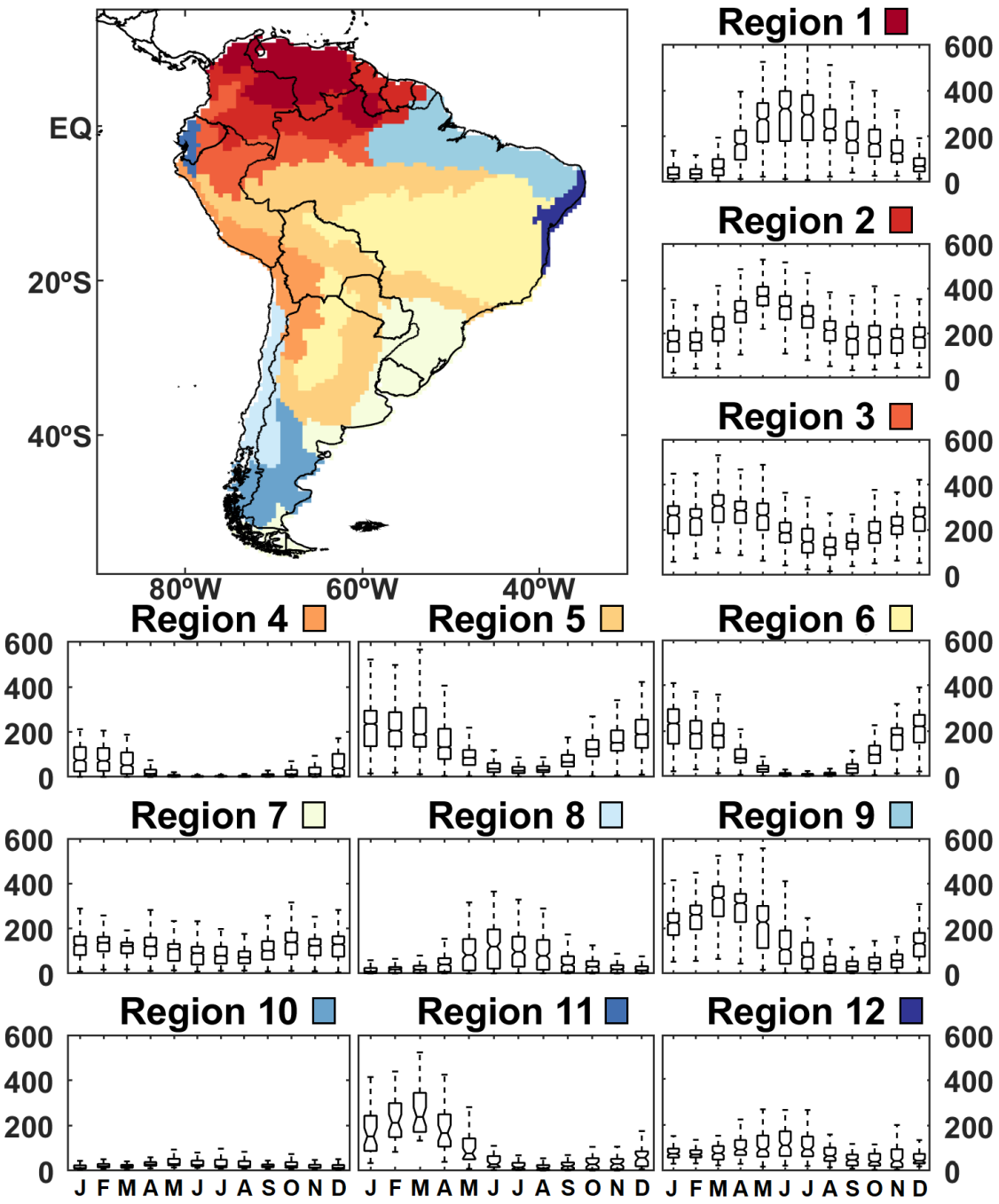

Figure 4.6: (a) The twelve homogeneous precipitation regions for the k-means clustering calculation. (b) Annual precipitation regime (mm/month) in each cluster region. Each region is shown in different colors.

Region 2

Region 2 is also located in the Northern Hemisphere, extending over Colombia, Guyana, Suriname and the extreme north of Brazil. This region shows high rates of precipitation

throughout the year with maximum precipitation during austral autumn (Figueroa and Nobre, 1990; Rao and Hada, 1990), particularly in May (∼360 mm; Figure 4.6). This region is mainly influenced by the ITCZ, which takes its position further south between March and April, affecting the North and Northeast Regions of Brazil (Hastenrath and Lamb, 1977; Rao and Hada, 1990; Poveda et al., 2006; Melo et al., 2009). The mean duration of these disturbances is around 4-5 days with maximum activity during the austral winter (Machado et al., 2009). The Mesoscale Convective Complexes (MCCs) are clusters of cumulonimbus clouds that generate storms with a duration ranging between 6 and 12 hours (Silva Dias, 1987; Silva Dias et al., 2009). These MCCs are normally associated with synoptic systems; however, in tropical regions, such as Region 2, they are formed due to the radiative surface influence (Reboita et al., 2010).

Region 3

Region 3 include the West of SA, eastern Ecuador, eastern Colombia, northern part of Peru, and northern of Amazonas State (Brazil). It is the second region with high levels of precipitation throughout the year. Unlike Region 2, Region 3 record maximum precipitation between December to May (Figure 4.6), with maximum monthly precipitation in March (∼290 mm/month).

As in Region 2, Region 3 is strongly influenced by the ITCZ over the Pacific (see Fig. 4.1), which migrates to the Southern Hemisphere between summer and autumn (Hastenrath, 1991). Likewise, the tropical Mesoecale Convective Systems (MCSs) in Region 3 are formed due to the radiative heating and the orographic effects on the eastern slope of the Peruvian and Ecuadorian Andes, and western slope of the Colombia Andes (Figueroa and Nobre, 1990; Garreaud and Wallace, 1998; Poveda et al., 2006; Laraque et al., 2007). In the northern part of Peru and northwestern Brazil (State of Amazonas) precipitation also occurs due to the arrival of low-levels winds from the Atlantic Ocean that brings moisture to the Amazon area, reaching the Andes (Figueroa and Nobre, 1990; Fisch et al., 1998).

Region 4

Region 4 is one of the driest regions of South America, with rainfall not exceeding 90 mm/month during its rainy season (December-March). Precipitation recorded during this period occurs mainly over Peruvian and Bolivian Andean regions. Garreaud et al. (2003) remark that the rainy episodes during this period are sequential, with an approximate

period of one or two weeks, followed by a dry episode with a similar duration. On the other hand, the minimum rainfall occurs in winter, between May and August (Figure 4.6). This region covers western Peru, northern Chile (Atacama desert), the Andes plateau and northwestern Argentina. Because this region covers different latitudes, there are different atmospheric systems responsible for precipitation regimes in this region.

The north part of Region 4, which is surrounding by the north coast of Peru, is still influenced by the ITCZ over the Pacific, although rainfall is also formed by deep convection due to surface radiative heating over this region and warm SST conditions of the Pacific in summer (Garreaud and Aceituno, 2007). On the other hand, the subsiding of the Southeast Pacific Subtropical Anticyclone (SPSA) is responsible for the low-rates of precipitation and moisture in the central west of Region 4 (Aceituno, 1980).

Another important circulation system that favors rainfall en Region 4 is the Cyclonic Vortex (CV), an upper-level, low-pressure system with a closed and cold core, which flows with western winds over the South Pacific and South Atlantic, especially in the summer months (Kousky and Gan, 1981) (see Fig. 4.1).

In addition, in the interannual time-scale, during the warm phase of El Niño-Southern Oscillation (ENSO), the intensity of the SPSA decreases. This pattern produces an increase and the development of convective activity in the north of Region 4, causing anomalous precipitation (Garreaud and Aceituno, 2007).

Region 5

Region 5 is located in the central part of SA, covering the central equatorial Amazon (central and southern of Peru and southern region of northern Brazil), the Bolivian Amazon, western Paraguay, western and central Argentina, and southern Mato Grosso, Sao Paulo and Paraná (Brazil). Most of Region 5 is located in the main corridor of the SALLJ, as observed by Boers et al. (2014) (see their Figure 1). Region 5 depicts similar rainfall regime compared to Region 4, but shows considerable precipitation even during wintertime (see Figure 4.6).

The rainfall distribution is mainly associated with a high-pressure system at high-levels, quasi-permanent in summer, and formed by the latent heat release due to the Amazon convective processes, known as Bolivian High (Silva Dias et al., 1983). Bolivian High also

influences severe conditions in Region 5, forming MCCs near the exit of SALLJ (Alves, 2009). The SALLJ, therefore, plays an important role in the formation of MCCs, which also is responsible for rainfall in this region.

In the Northeast coast of Brazil, the squall lines (SL) also produce strong precipitation, affecting Region 5 when these systems propagate towards the Andes (Cohen et al., 1989). Greco et al. (1990) found that the squall lines formed in the coast dissipate during the night as they propagate into the central Amazon, and diurnal heating reactivates them in this region (Rickenbach, 2004). During summer, the South Atlantic Subtropical Anticyclone (SASA) is located in its easternmost position, moving away from the coast and introducing moisture from the Atlantic to the continent, favoring precipitation. However, in winter the SASA migrates to the west and a part of it is located on the Southeast of Brazil, suppressing convection there (da Silva et al., 2014). Finally, the cold fronts also play an important role in organizing convection in Region 5. However, remnants of these systems can propagate to the north and, eventually, reach the equator, causing an event known as "friagem" (Marengo et al., 1997).

Region 6

Region 6 covers a broad area of SA (Central, West, and Southeast of Brazil), including the Chaco region (central-southern region of SA). This region shows a remarkable monsoon rainfall regime with maximum precipitation in summer and minimum in winter. The main atmospheric precipitation systems over this region are the Bolivian High, the SALLJ and the formation of MCCs, especially during the rainy period. Oftentimes, the SACZ becomes the most important rainfall producing system over Region 6. As found in Region 5, the SASA also affects Region 6, when introduce moisture from the Atlantic to the continent, favoring precipitation during the summer and early autumn. Moreover, during summer the moisture flux transported by the SALLJ can converge with the SASA, triggering a band of deep convection and nebulosity (Carvalho et al., 2002; Garreaud et al., 2009; Gan et al., 2009; Marengo and Nobre, 2009), generating rain over Region 6 (southeast of Brazil). On the other hand, pre-frontal systems produce precipitation over Argentina, Southeast of Brazil, and Southwest of the Amazon, also leading intense and persistence SACZ over the continent (Carvalho, 2009a). CVs are also common during the summer period in Subtropical Atlantic, favoring precipitation in southeastern Brazil, either by the

penetration of frontal systems (Kousky and Gan, 1981; Satyamurty et al., 1990) or by an anticyclonic circulation in the Southwest of Atlantic and Southeast of Brazil (Ramirez et al., 1999; Carvalho, 2009b).

Region 7

Region 7 is located over southern Brazil, southern Paraguay, Uruguay, including a narrow strip in the east of Argentina. Similar rainfall regimes are also found in the extreme tip of SA. This region is in mid-latitudes and depicts considerable precipitation throughout the year (Rao and Hada, 1990), with a non-well-defined rainy season. Cumulative monthly rainfall ranges between 75 and 130 mm (Figures 4.6).

This homogeneous precipitation regime is influenced by two main factors: MCSs in summer and cold fronts during winter (Montecinos et al., 2000; Garreaud and Aceituno, 2007). The MCCs are more frequent during November to April. As documented in previous literature (e.g., Satyamurty et al., 1998), the SALLJ contributes to the formation of MCCs in northern Argentina, Paraguay, Uruguay, and southern Brazil. In addition, in the morning and with a very short period, MCCs are product of the radiative heating that triggers deep convection over southern Brazil and Uruguay (Velasco and Fritsch, 1987; Garreaud and Aceituno, 2007). On the other hand, frontal systems favor deep convection and prefrontal squall lines that produce precipitation. Satyamurty et al. (1998), also found that mountain breezes can be formed by atmospheric instability in this region.

Finally, in the southern tip of SA, the other portion of Region 7, only the frontal systems and low-pressure systems operate all year round (Reboita et al., 2010; Viale et al., 2019).

Region 8

Region 8 is located in central Chile and northwestern of Patagonia. This region presents maximum precipitation during May to August period, while the rest of the year the precipitation is usually low and homogeneous (Figures 4.6). The main systems and conditions that modulate precipitation in Region 8 is the presence of the Andes and the South Pacific Anticyclone (SPA; Taljaard, 1972). In summer, the SPSA is located in its southernmost position ($\sim$35° S), inhibiting convective activity in the central-southern coast of Chile. Whereas, in winter, SPA is located in its northernmost position, and winds from the west

to the south of the SPA reach the Andes, causing convection by orographic rise (Taljaard, 1972; Garreaud and Aceituno, 2007). Another factor that influences precipitation over Region 8 is the frontal systems, which move further north in winter, causing precipitation before crossing the Andes. In contrast, during summer, as the SPSA is located further south, it acts as a barrier for the cold fronts passage (Reboita et al., 2010; Viale et al., 2019).

Region 9

Region 9 covers a broad area in North of Brazil, including the Amazon Delta region. As found in Region 3, Region 9 shows maximum precipitation values from early summer to autumn, with a maximum monthly precipitation in March (∼315 mm/month). However, Region 9 exhibits a clear dry season, which occurs between August to November (Figure 4.6). The main precipitation system over Region 9 is the ITCZ, causing considerable precipitation during its migration towards the south during February to April (Hastenrath, 1991). In addition, the interaction between the ITCZ and other systems can intensify rainfall in Region 9. For instance, the convective activity of the ITCZ, trade winds loaded with moisture from the Atlantic, and the radiative surface heating cause the formation of MCCs and squall lines (see Fig. 4.1). The formation of squall lines on the coast of Region 9 is also associated with heavy rainfall during March to May, mostly in the afternoon, associated with sea breeze circulation (Fisch et al., 1998; Cohen et al., 1989).

Besides, anomalous migration of the ITCZ further north or south causes change in both, the beginning and the end of the rainy season over this region (Melo et al., 2009), as well as the existence of a double band of the ITCZ between January to August (Hastenrath and Lamb, 1977; Uvo, 1989; Grodsky and Carton, 2003). On the other hand, the EW in the Tropical Atlantic also spread to the Northeast Brazil coast in June-August generating periods of rain during these months (Yamazaki and Rao, 1977).

The Warm Cloud (WC) are shallow clusters of mainly maritime origin or coming from well-developed trade winds, which has the amount of liquid water necessary to produce precipitation known as “warm rain” (Costa et al., 2000; Liu and Zipser, 2009). In Region 9, the WC is formed on the south of the second ITCZ in March-May, in the early afternoon (Liu and Zipser, 2009) influenced by the ITCZ and EW (Machado et al., 2014).

Finally, an upper-level trough over Northeast Brazil, associated with the Bolivian High,

favors the formation of tropical CVs (Kousky and Gan, 1981); likewise, the subtropical CVs formed in the southwestern Atlantic move and may affect Region 9 (Carvalho, 2009b).

Region 10

Region 10 is located in southern tip of SA (western Patagonia, south of Argentina). This region presents homogeneous and low precipitation year-round with monthly accumulated not exceeding 60 mm/month, being the driest region of SA. In the north part of Region 10 (eastern slope of the Argentinian Andes) the absence of precipitation is due to the dry flow of the west that crosses the Andes. On the other hand, in the southern part of this region, the frontal and low-pressure systems (cyclones), favor small precipitation that falls on the region during austral winter (Reboita et al., 2010; Viale et al., 2019).

Region 11

Region 11 is located in the coastal region of Ecuador and part of the northern highlands of Peru. It presents high precipitation values between January to May, with a peak in March, and shows low values of precipitation between July to November. Figueroa and Nobre (1990), for instance, define this region as having an equatorial regime, where the Hadley circulation plays an import role. The ITCZ over the Pacific, and the radiative surface heating as well, contribute to the generation of convection and precipitation. During the winter, the ITCZ is located in its northernmost position over the Pacific ($\sim 13^{\circ}\ N$) causing a significant decrease precipitation (Satyamurty et al., 1998).

Region 12

Region 12 covers a narrow band in the extreme Northeast Region of Brazil. This area records low rates of precipitation, with maximum values during April to August, which does not exceed 120 mm/month in accumulated monthly average.

As was observed in Region 9, the easterly waves propagate towards the NEB coast in southern winter over Region 12, generating periods of constant precipitation there (Yamazaki and Rao, 1977). Trade winds of the southeast also influence precipitation, because they are more intense in this period. These winds converge with the land breeze favoring convective activity in Region 12 .

On the other hand, the tropical CVs formed by the trough located to the northeast of Brazil (see Fig. 4.1), and the subtropical CVs formed to the southeast of South Atlantic,

produce episodes of rain on this region during summer. Finally, WCs are formed during winter on the east coast of Region 12 caused by the advection of trade winds, the ITCZ and EWs (Liu and Zipser, 2009).

4.2 The SST Variability over the Atlantic Ocean

The sea surface temperature (SST) of the Atlantic Ocean has been analyzed by several authors who found evidence that ocean-atmosphere interaction in the Atlantic Ocean affects precipitation patterns. For instance, the Northeast of Brazil is affected by the SST 'dipole' pattern over the tropical Atlantic, which modifies the ITCZ position southernmost (northernmost) of its climatology (Hastenrath and Heller, 1977; Nobre and Shukla, 1996). Cold (warm) Tropical North Atlantic, and warm (cold) Tropical South Atlantic during summer and autumn yields wetter (driest) rainfall conditions (Nobre and Molion, 1988; Melo et al., 2009). However, there are other spatial patterns in the Atlantic that could influence in rainfall over the Amazon Basin. In this section, therefore, the interannual variability of the Tropical Atlantic Ocean is analyzed through the EOFs technique. For this purpose, the Atlantic region was divided into three basins: Tropical North Atlantic (TNA; between 23.5° N-5.5° N and 75° W-10° W), Tropical South Atlantic (TSA; between EQ-20° S and 50° W-15° E) and Subtropical South Atlantic (STSA; between 20° S-50° S and 67.5° W-0°).

4.2.1 Climatology and annual cycle of the Atlantic SST

Before assesing the interannual variability of the Atlantic, the climatology and the annual cycle of the SST from the HadISST datasets for the 1979-2015 period will be first analyzed . Figure 4.7 shows the standard deviations of the SST and the annual cycle for the Atlantic, where the TNA, TSA, and STSA regions are enclosed in the blue box. The Atlantic presents a marked seasonal cycle (Lübbecke et al., 2018; Brierley and Wainer, 2018). The Tropical Atlantic SST presents warm conditions over the western section, where isotherms above 27° C penetrates towards the eastern limit at approximately 10°-25° N (Figure 4.7a). The TNA region is enclosed into the isotherms of 27° C, while the TSA has mostly SST area below 27° C. Meanwhile, the STSA region, in addition to having low

values of SST, shows almost zonal isotherms. However, these SST values are affected by the annual cycle of each region.

The TNA annual cycle shows higher values from August to November, and the annual climatic range is approximately 3° C (Figure 4.7b). Near the coast of Senegal, the SST presents a higher deviation (see Figure 4.7a), which occurs between the months of May-August, where the ITCZ is shown in its northernmost position (Garreaud et al., 2009; Brierley and Wainer, 2018).

On the other hand, the TSA region shows an annual cycle with maximum values in the austral summer. However, unlike the TNA region, the TSA has lower SST values, with an annual SST range of approximately 4° C (Figure 4.7b). The spatial SST are dominated by the presence of a "cold tongue" coming from the southwest of Africa (see Figure 4.7a). This deviations values are due to displacement of the ITCZ to the north between April and May, and to the south in September. This variations triggers shoaling of the thermocline, influx, and vertical mixing, as well as an intensified evaporation (Lübbecke et al., 2018). These features are clearly observed as having the bimodal pattern in the annual standard deviation cycle (Figure 4.7b).

Finally, the STSA, like the TSA, has an annual cycle with maximum SST in the austral summer. Maximum standard deviation values are centered in the southwest of the Atlantic. In this region, fluctuations of the isotherms (see Figure 4.7a) are due to the encounter of two sea currents (Brazil Current from north and Malvinas or Falklands Current from south) as documented by Robertson et al. (2003).

4.2.2 Spatial patterns of the Atlantic SST

This section shows the patterns corresponding to the main modes (Empirical Orthogonal Functions - EOFs) and Principal Components (PC) for each region of the Tropical and South Atlantic. For this purpose, the covariance matrix of the SST anomalies for each region was taken as input, using 1979-2015 period as base of the climatology. From this matrix, the eigenvectors (EOFs) and eigenvalues were calculated. The PC are obtained by projecting the SST anomalies onto the EOFs.

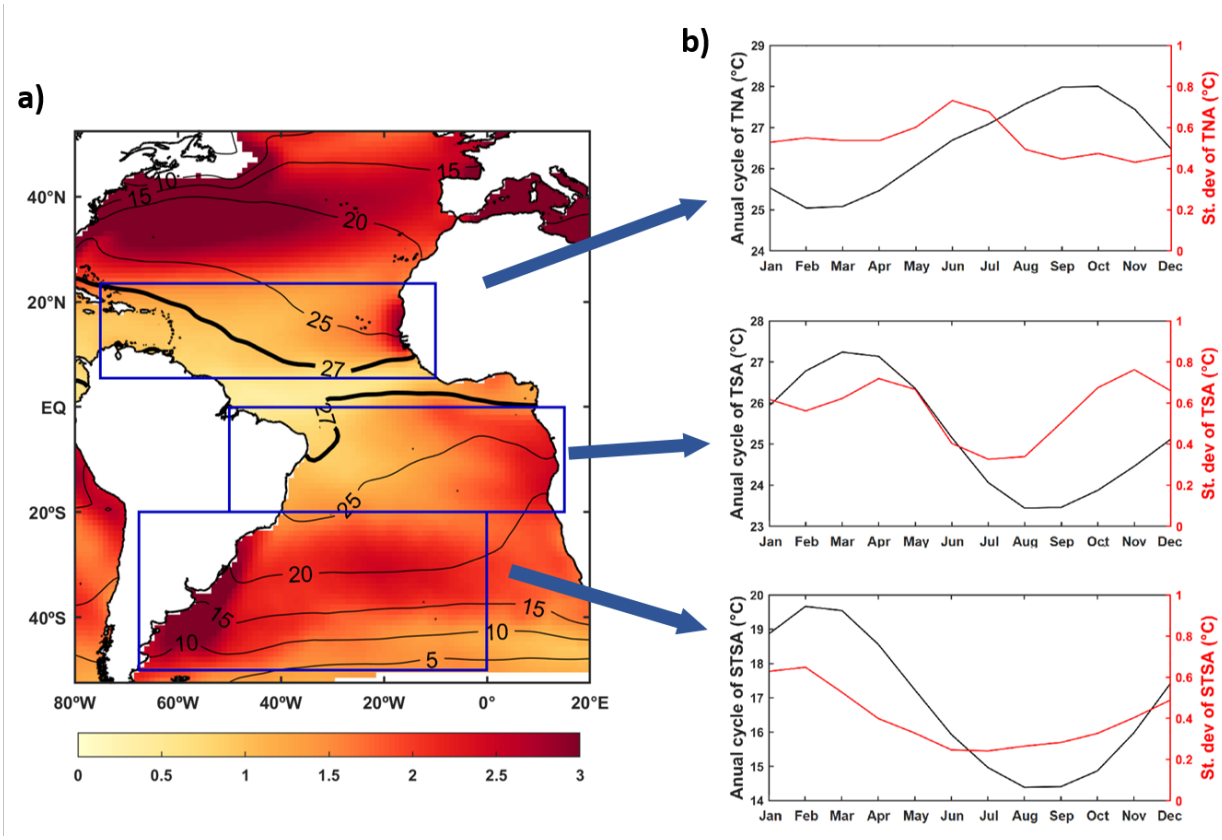

Figure 4.7: Atlantic Ocean SST from monthly HadISST dataset for the 1979-2015 period. (a) Standard deviation (shading) with its annual mean climatological SST (contours). (b) Annual cycle of the monthly average (black) and standard deviation (red) of the SST for TNA, TSA, and STSA region.

4.2.2.1 Tropical North Atlantic (TNA)

Figure 4.8 shows the first two leading modes from the EOF analysis applied to the monthly SST over the TNA region. The first mode (Figure 4.8a) explains about 58.6% of the total variance of the TNA, while the second mode (Figure 4.8b) explains 11.71%. The first spatial pattern (EOF1) mainly represents warming (or cooling) conditions centered in the central region of the TNA. SST anomalies are correlated with PC1 (Figure 4.8a), showing the configuration of the Atlantic interhemispheric and fairly modulated by the AMO phases (Houghton and Tourre, 1992; Sun et al., 2018). In the warm phase of the AMO, for instance, the SST shows warm conditions over the Tropical North Atlantic region, eastern subtropical North Atlantic and the northern end of the Atlantic, and cold SST conditions in the western subtropical Atlantic region (Kerr, 2000; Hu et al., 2011). The spatial pattern for the first mode over the TNA region is consistent with the well-

documented previous works for this region, such as Dommenget and Latif (2000); Huang et al. (2004), among others.

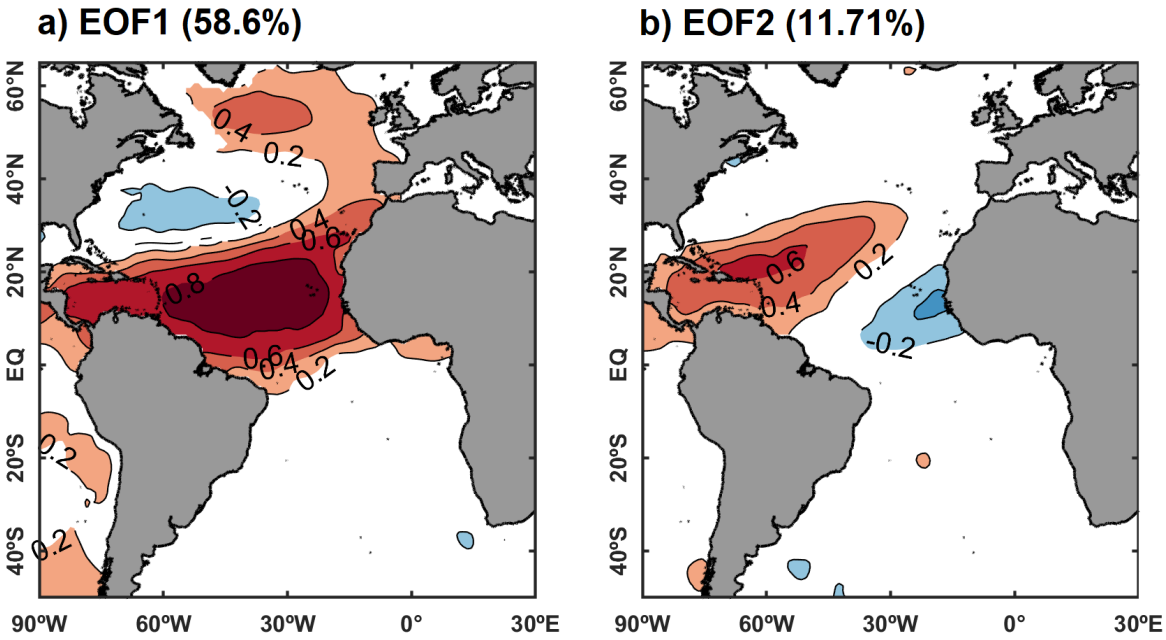

Figure 4.8: Spatial patterns for the Tropical North Atlantic refer to (a) EOF1 and (b) EOF2 in the 1870-2017 period. The maps are shown in the form of correlation coefficients between SST anomalies and the time series of the corresponding EOF mode. Contour interval is 0.2. Red (blue) shadings indicate positive (negative) correlation exceeding the 5% significance level.

The second spatial pattern (EOF2) shows a dipole configuration between the northwest (Caribbean Atlantic) and the coast of Senegal (Figure 4.8b). Because the first mode explains a significant percentage of the total variance, we only used the time series of PC1 for further analysis.

Further analyses applied to the EOF1 time series is shown in Figure 4.9. The wavelet spectrum applied to the PC1 (Figure 4.9a), for instance, shows more significant values in the scale associated with the seasonal and the annual cycles. This is more noticeable during 1960-1990 decades. Moreover, significant values are also observed in 60 months (3 and 5 years) and 128 months (10-11 years) corresponding to the interannual and the decennial variability, respectively. To better analyze these scales, a power spectrum was performed, eliminating, first, frequencies less than 12 months by applying a Lanczos filter. The power spectra (Figure 4.9b) mainly follow a red noise distribution, consistent with Dommenget and Latif (2000) and Huang et al. (2004). Two main peaks occur: one in periods less than

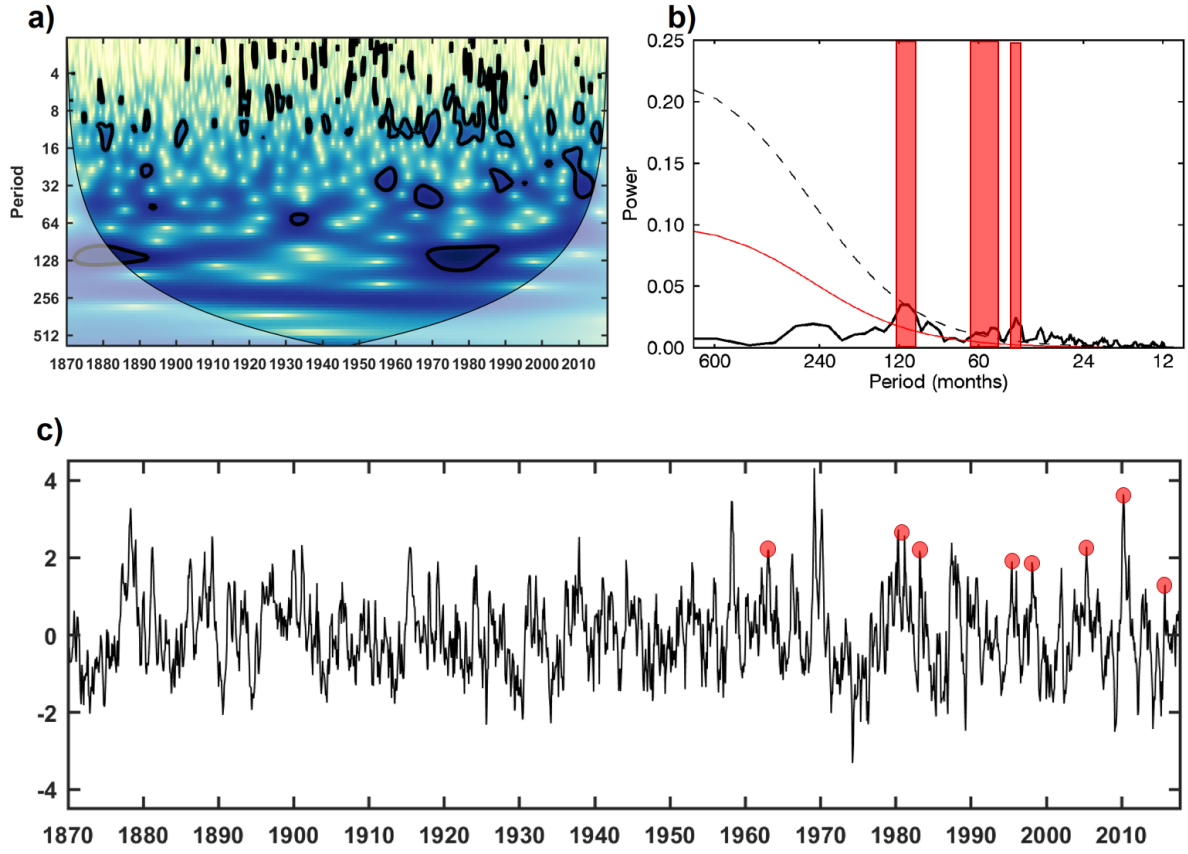

Figure 4.9: Statistical features of the PC1 for the TNA in the 1870-2017 period. (a) Wavelet power spectrum. Thick lines indicate statistically significant variability. (b) Filtered power spectrum of PC1. The red solid line indicates the red noise background spectrum and the dashed line are the 95% confidence level. (c) PC1 time series for the entire period. The red circles indicate the SST peaks associated with recorded extreme precipitation events (droughts) in the Amazon Basin.

five years and, as a secondary peak, one centered in ten years.

Besides, the PC1 time series (Figure 4.9c) is able to show peaks associated with extreme precipitation events (droughts) recorded by anomalous warm TNA conditions, which occurred in 1963-1964, 1979-1981, 1982-1983, 1995, 1997-1998, 2005, 2010, and 2015. All these events are well-summarized in Espinoza et al. (2019).

Since PC1 is used to explain the TNA behavior, it is noteworthy to compare it with the PIRATA SST data. Figure 4.10 shows the time series of PC1 and the SST anomalies from two PIRATA stations located in the TNA region. The Pearson correlation calculated between PC1 and Station1 time series was 0.63, and between PC1 and Station2 was 0.82. Therefore, it can be concluded that PC1 well-explains the SST anomalies variations over

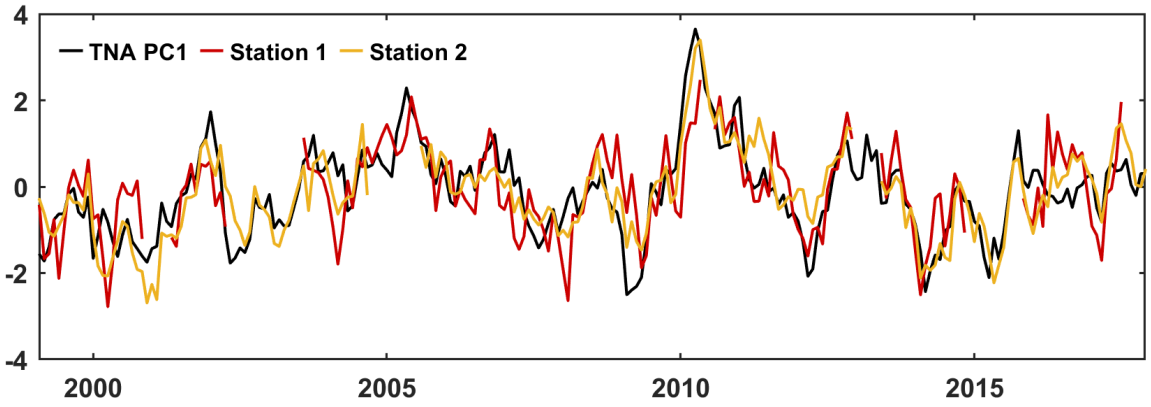

Figure 4.10: TNA PC1 times series (black line) and times series from PIRATA stations located over the TNA region for 1998-2017 period.

tropical Atlantic. Finally, the PC1 time series could be used to explain the SST variability, and monitoring extreme precipitation events over the Amazon and several other parts of South America as well.

4.2.2.2 Tropical South Atlantic (TSA)

Figure 4.11 shows that two leading modes explain a significant amount of the total variance of the SST distribution on TSA. The remaining modes contributes with a much smaller fractional variance. The EOF1, for instance, explains a high percentage (57.17%), and EOF2 explains 13.79%. The first spatial pattern, as shown in Figure 4.11a, exhibits SST fluctuations over the TSA region, coincident with a configuration pattern of the north pole of the South Atlantic Dipole (SAD) (Venegas et al., 1997; Sterl and Hazeleger, 2003; Bombardi et al., 2014; Nnamchi et al., 2011). This spatial feature is centered on the coast of Africa between Guinea Equatorial and Angola. The PC1 time series, obtained from the EOF analysis, is well-correlated with the global SST anomalies with positive correlations over regions mentioned above. These results are in agreement with Hirst and Hastenrath (1983), who also found a strong modulation of precipitation due to TSA fluctuations on the coast of Africa (east South Atlantic). In addition, this spatial pattern is similar to the TSA pattern documented in Huang et al. (2004), through EOF in the Atlantic for 50 years. On the other hand, the spatial pattern of EOF2 (Figure 4.11b) indicates a dipole configuration within the TSA region, with significant positive correlations centered near

the coast of Southeast Brazil and negative correlations on the coast of Congo.

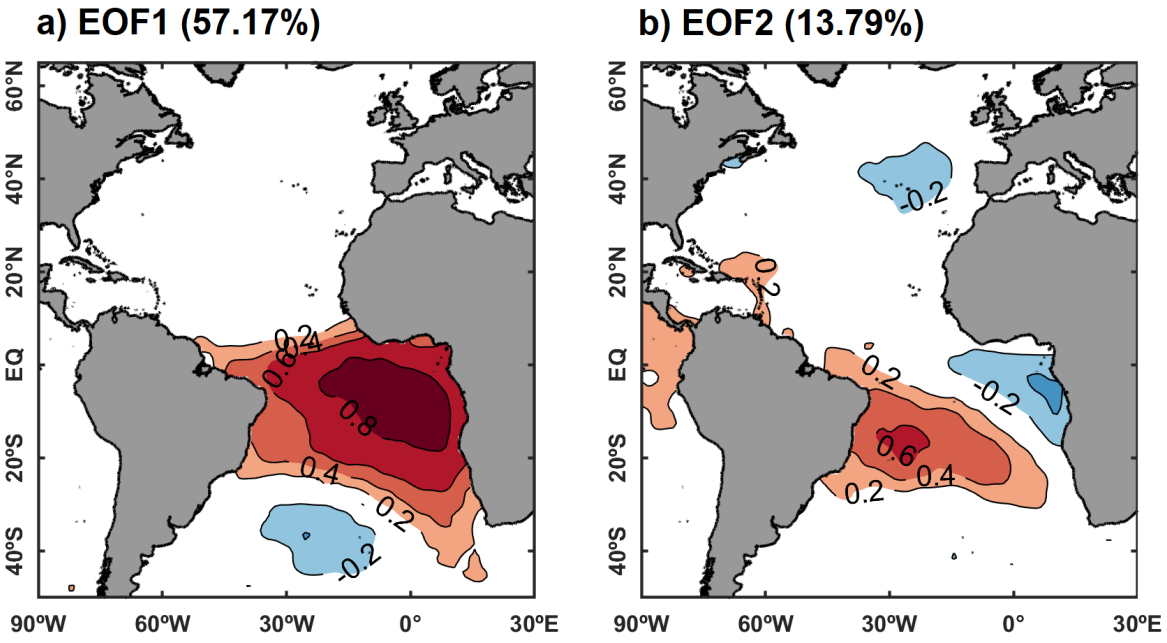

Figure 4.11: As Fig. 4.8, but for TSA.

The TSA temporal variability of the first EOF is shown in Figure 4.12. The wavelet power spectrum (Figure 4.12a) shows significant values on a seasonal scale. On the other hand, significant frequencies are also shown in 30-32, 128, and 256 months (approximately 2.5, 11, and 21 years, respectively). The filtered power spectrum (Figure 4.12b) also follows a red noise distribution, with maximum peaks at 1.5, 2.5, 4, 5, and 11 years.

The time series of PC1 (Figure 4.12c), reinforces what was observed in the spectrum, showing a strong interannual variability. In the time series, maximum peaks of the SST are observed in years in which remarkable extreme event occured (associated with floods) due to the TSA warm conditions. These events are also highlighted in light blue circles.

Considering the PC1 time series given by the EOF analysis, Figure 4.13 shows that the evolution of SST anomalies from PIRATA stations are well-represented by the PC1. Correlations between the PC1 time series against time series at both stations are 0.53 and 0.55 for Station1 and Station2, respectively.

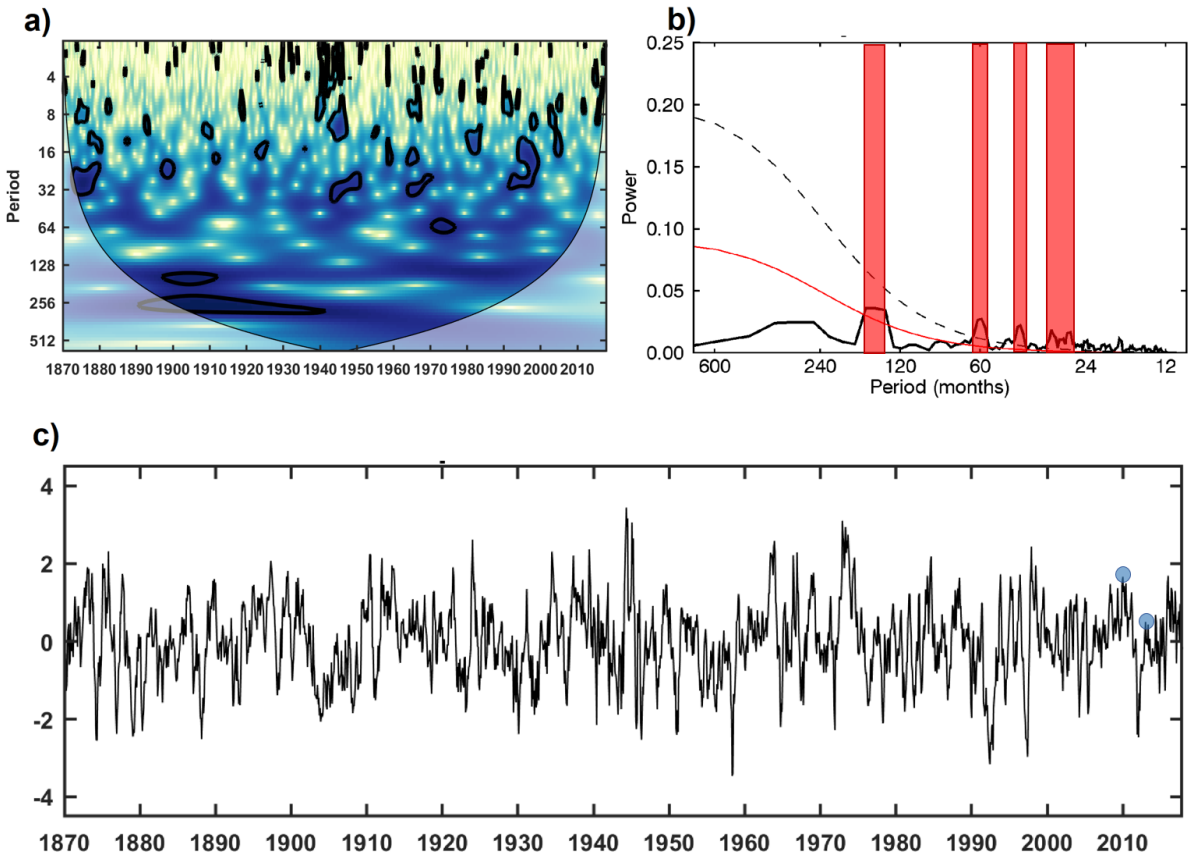

Figure 4.12: As Fig. 4.9, but for TSA. The blue circles indicate the SST peaks associated with recorded extreme events of precipitation (flood events) in the Amazon Basin.

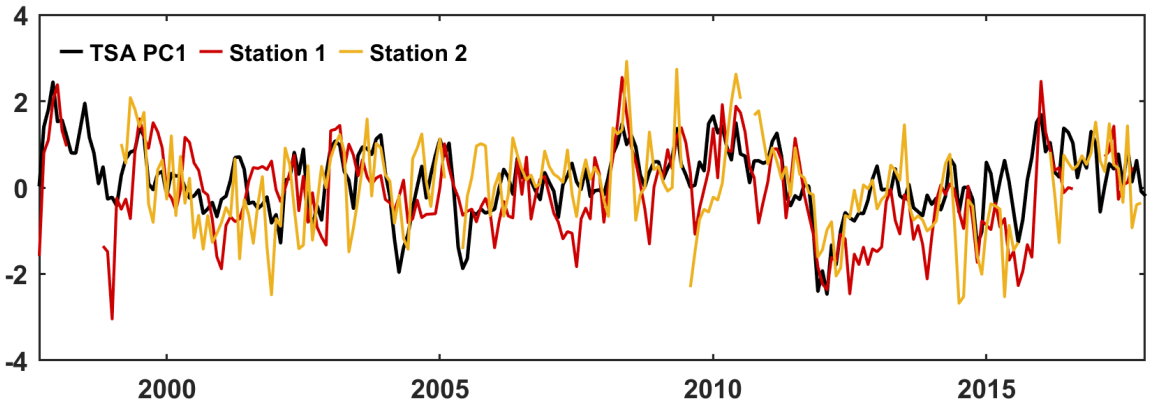

Figure 4.13: As Fig. 4.10, but for TSA.

4.2.2.3 Subtropical South Atlantic (STSA)

The southern subtropical Atlantic (STSA), unlike the tropical Atlantic, have three leading spatial modes, that explain a large percentagem of the variance (Figure 4.14), where the first mode (EOF1) explains approximately 21.41% of the total variance, the second (EOF2) explains 14.74%, and the third (EOF3) 14.16%, respectively. The spatial feature of the first EOF shows positive correlations centered near the southeastern coast of South America (Figure 4.14a). The SST has almost a zonal climatic isotherms (see Figure 4.7), presenting positive correlations between the PC1 and the SST anomalies for this region. This spatial pattern is similar to the second mode of variability of the South Atlantic (south pole of the SAD pattern) shown by Sterl and Hazeleger (2003, see their Figure 1b).

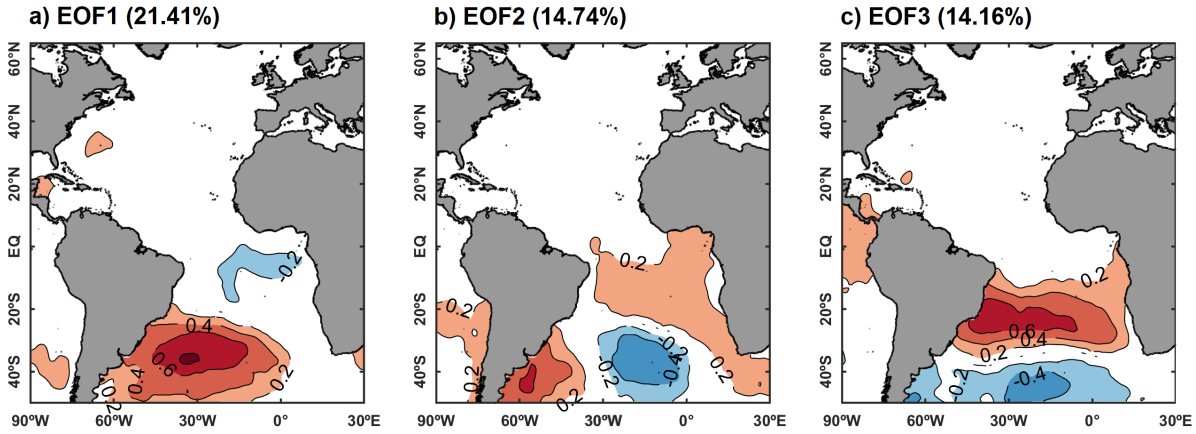

Figure 4.14: As Fig. 4.8, but for STSA.

The second EOF (Figure 4.14b) shows positive correlation centered along a large stretch of the coast of Africa, extending towards the equatorial Atlantic. The second and strong correlation is also observed in the southern Atlantic. Between the two positive correlation areas is observed an area of negative correlation, resembling the wave trains pattern in the atmosphere, which is also quite often over these same regions. The positive correlation over the coast of South Africa seems to be related to the "Agulhas leakage", which is a warm and saline water flow from the Indian Ocean (de Ruijter et al., 1999). This flow pattern can influence the tropical Atlantic and the Northeast Region of Brazil through the southern equatorial current in a period of 10-15 years (Castellanos et al., 2017; Rühs et al., 2013).

The third EOF (Figure 4.14c), which explains about 14% of the total variance, shows a dipole configuration in the South Atlantic. The correlations between PC3 and SST anomalies of the STSA region show positive values on the southeast coast of Brazil towards the northern region of the South Subtropical Atlantic (20-25° S) and negative correlations at the southern end of the STSA, centered around 45° S. This dipole feature is consistent with the interannual variability of the SACZ documented by Robertson et al. (2003), also coinciding with the confluence of the currents of Brazil and Malvinas.

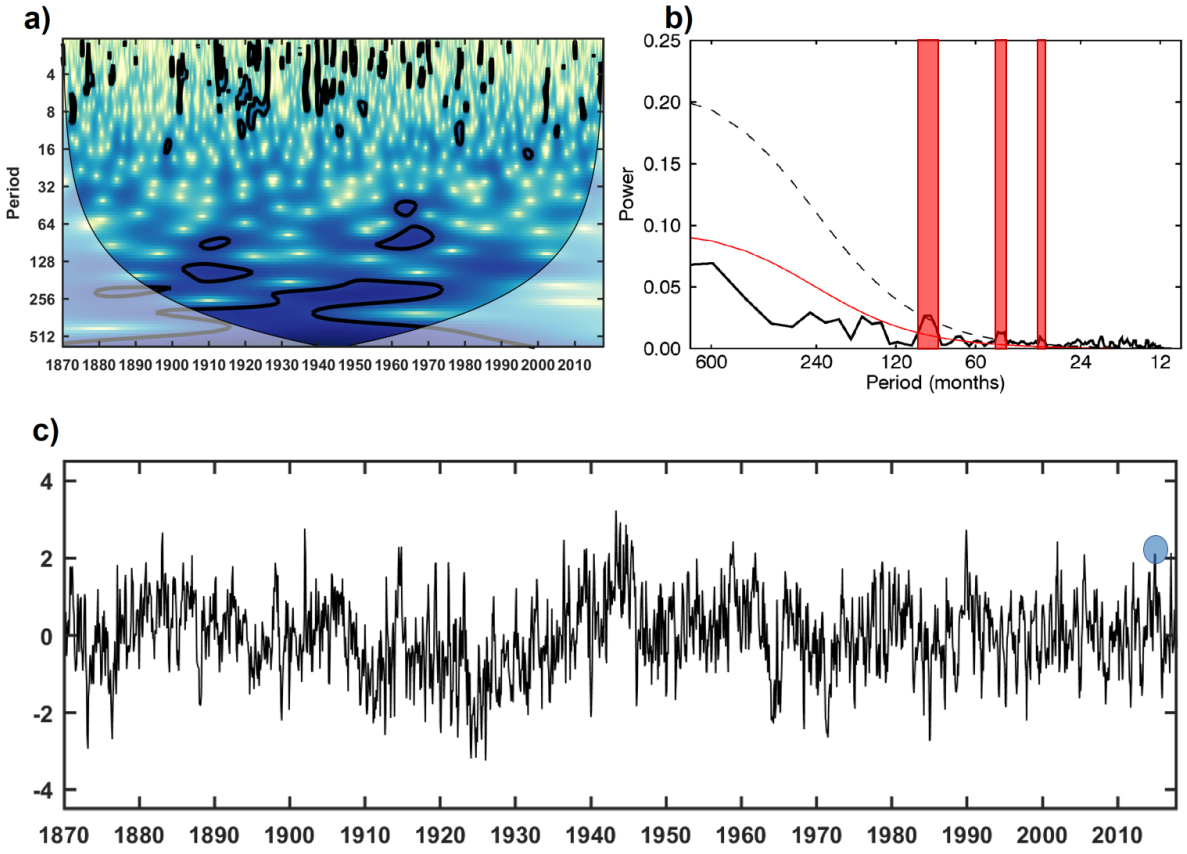

Figure 4.15: As Fig. 4.9, but for STSA.

Although the first three spatial patterns explain almost all of the total variance, the PC1 was finally used for further analysis. The PC1 time series of the STSA is shown in Figure 4.15. The wavelet power spectrum (Figure 4.15a), similarly to the TNA and TSA region, shows a strong power centered on seasonal variations. Significant values, however, are also observed in periods of 1.5, 4-6, 10, 30 and even more than 40 years, similar to the oscillations found by Wainer and Venegas (2002). The filtered time series shown in the power spectrum (Figure 4.15b) reinforces the interannual variability of the STSA, showing

distribution in red noise for periods at 1.5, 4, 5, 6 and 8 years. Other periods do not exceed the red noise, even if they show peaks.

Finally, the PC1 time series (Figure 4.15c) shows the oscillation of approximately 20 years between 1870 and 1950 (Figure 4.15a). On the other hand, high and low peaks are shown in this pattern, periods in which the STSA was warmer or colder than normal. The blue circle represents the extreme flood event over southern Amazon Basin related to anomalous warm STSA in 2014 (Espinoza et al., 2014; Coelho et al., 2016). Despite this event was related to a strong PC1 or warm STSA condition, it can also be seen others high peaks before that period. In this way, further investigation is required.

4.3 Relationship between the Atlantic and the Pacific SST

It is well-known that the rainfall variability over South America is influenced by the Pacific SST variation, especially on the ENSO region. However, the Atlantic region has also shown evidences of being responsible for extreme precipitation variations in the last decades (Yoon, 2016).

The time series of the interannual and interdecadal indices of the Atlantic and the Pacific region is shown in Figure 4.16. The PC1 time series obtained from the EOF analysis detailed in the previous section are considered as Atlantic indices. Hereafter, these indices will be referred to as TNAi (TNA-PC1), TSAi (TSA-PC1), and STSAi (STSA-PC1). The Pacific indices, documented in detail in Takahashi et al. (2011), corresponding to the Eastern Pacific (E index) and Central Pacific (C index) region are also considered for the analysis. The decadal and interdecadal indices which correspond to the Atlantic Multidecadal Oscillation (AMO) and the Pacific Decadal Oscillation (PDO) are used in this work as a complementary analysis. The PDO and the AMO are shown as red and blue shaded areas in Figure 4.16, based on their positive and negative values, respectively. Shaded circles, in addition, show the years when are recorded extreme rainfall events of drought (red) and flood (blue) occurrences in the Amazon Basin, according to Espinoza et al. (2019) (see their Table 1).

First, analyzing the behavior of the SST in the Atlantic, the TNA index and the AMO show a similar pattern, reinforcing what was mentioned in the previous section, that the

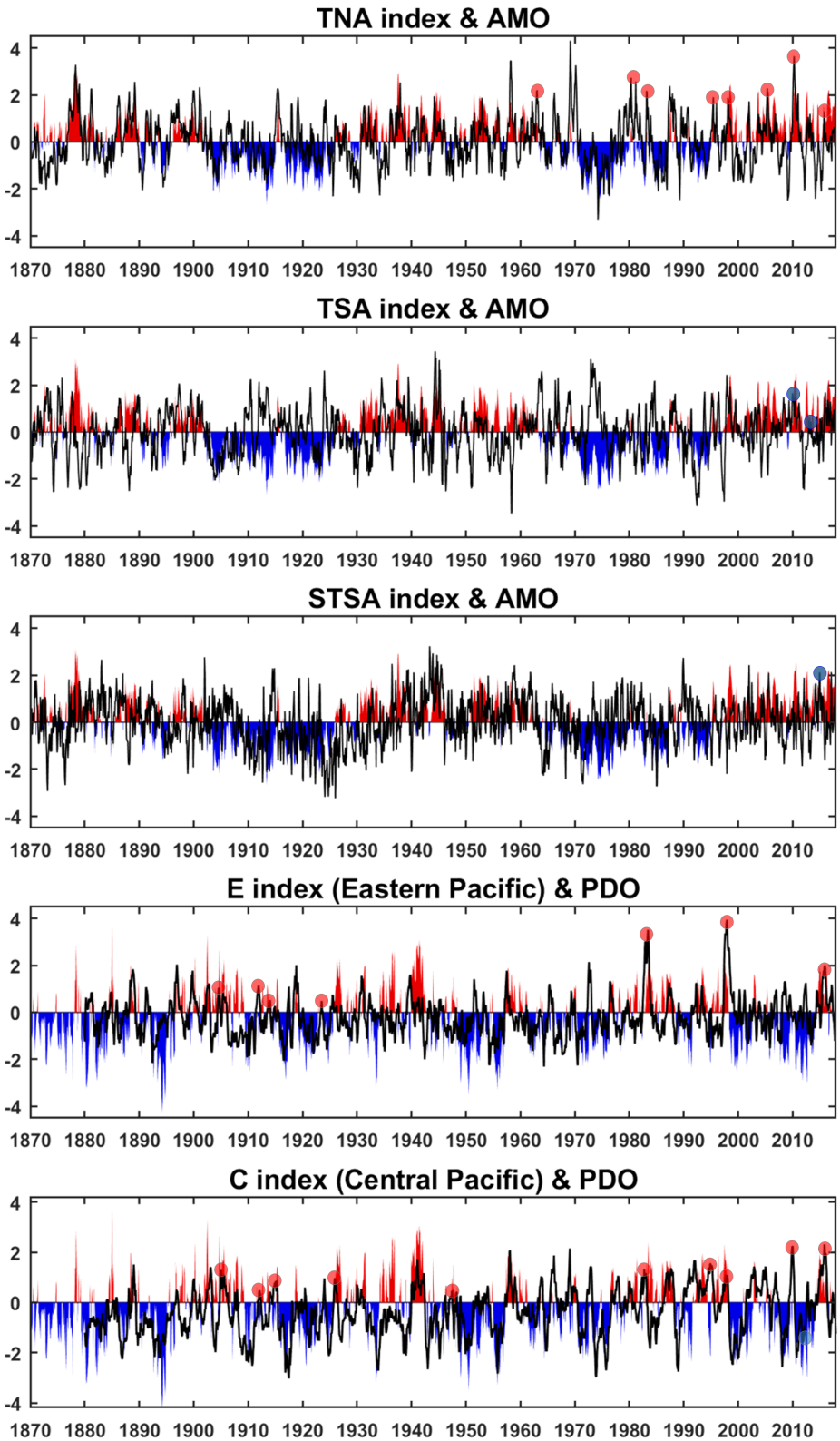

Figure 4.16: The Tropical Atlantic and Pacific indices. Black lines represent interannual Atlantic (TNAi, TSAi and STSAi) and Pacific indices (E and C). Red and blue areas correspond to positive and negative PDO and AMO index.

first mode of the TNA region are strongly modulated by the AMO phases (see Figure 4.8). Drought events recorded in the Amazon Basin due to TNA warm conditions are consistent with the positive peaks over the time series. Moreover, most of all events recorded in the last decades coincide with the positive AMO values, except for events occurred in 1980-1981 and 1983, where the AMO presented negative to neutral values. On the other hand, strong peaks in TNAi and AMO index as well in 2010 is also visible. As documented in previous works, this event was considered the most severe drought event in the century (Marengo et al., 2011). As expected, the AMO index also record strong values.

On the other hand, the TSAi is more variable compared to TNAi, and does not follow the AMO variations specifically in the last 40 years. As observed in Figure 4.16 (second panel) it is noticeable that when the AMO has positive values, TSAi also presents positive values. Years with extreme flood events recorded in the Amazon Basin were affected according our results by an increase in the SST of the TSA. Despite this recorded events do not associated to high values of TSAi as in other years, the AMO has positive values and, in combination with other mechanisms, could develop the extreme precipitation events. The extreme flood 2012 event (Marengo et al., 2013), likewise, was associated with low SST values in the STAi. However, these values were preceded by a low peak in the time series (Figure 4.16).

Concerning the STSAi, AMO positive and negative phases still modulate warm and cold conditions over this region. The only extreme rainfall event (flood) recorded in the Amazon Basin, due to STSA warming, occurred in 2014. As observed in the STSAi time series (Figure 4.16, third panel) that year presents a strong positive peak and AMO dos the same as well. However, similar peaks was also recorded in past years (e.g. 1883, 1902, 1914, 1936, 1943-1944, 1990, 2001-2002), which could indicate the existence of other unrecorded events associated with the STSAi anomalous conditions.

In the Pacific region, both the Eastern and the Central Pacific (E and C index) also follow the PDO variation. However, the ENSO varies on interannual scale ($\sim$2.5-7 years), while the PDO oscilates on decadal time-scale ($\sim$20-30 years) (Mantua and Hare, 2002). The extraordinary ENSO events (e.g., 1982-1983, 1986-1987, 1997-1998, 2015-2016), indeed, occurred in phase with PDO strong and positive phase. In the time series corresponding to the Eastern Pacific (E index), the peaks during the ENSO events of 1982-1983 and

1997-1998 years are notorious, as highlighted by Freund et al. (2019). These peaks caused drought events in the Amazon Basin (Marengo et al., 2008; Espinoza et al., 2019). Strong E index, as documented in previous works, more accurately measure the occurrence of the extraordinary ENSO events. Besides, all the SST peaks in the Eastern Pacific region, related to extreme events, are accompainned by positive PDO values, which does not happen with the Central Pacific. In this region, the most significant peaks occur in 2010 and 2015, also associated with drought events on the Amazon (Marengo et al., 2011; Marengo et al., 2018; dos Santos et al., 2017; Espinoza et al., 2019).

On the other hand, although in the 1982-1983 event the TNAi shows high values and the AMO shows neutral values, the significant increase of the SST in the Eastern Pacific helped the formation of this drought event. Similarly, in 2010, the PDO showed neutral values. However, the C index and the TNAi have very high values that explain why this event was considered one of the most extreme.

In the previous section, the modes of variability of the Atlantic were observed, showing that each oceanic basin (TNA, TSA, and STSA) presents individual warming and individual influencing in rainfall over South America and the Amazon Basin. However, the warming period of these regions may not be separated from each other, and the same applies to the ENSO regions (Eastern Pacific and Central Pacific). This section shows the analysis related to the coupling and decoupling of the Atlantic and Pacific Ocean basins over time, and the connection between these ocean basins, in order to observe influences from one basin to another that could trigger extreme precipitation events over the Amazon.

4.3.1 The relationship between the tropical and extratropical Atlantic Ocean

Figure 4.17 shows the 7-year moving correlations between the three Atlantic basins two by two (TNA - TSA, TNA - STSA and TSA - STSA). Positive correlations indicate a coupling between the basins: for instance, both are warming at the same time. Negative correlation also indicates a coupling between them: while one is warm, the other is cold. Finally, a low correlation or close to zero means decoupling between the different Atlantic regions.

TNA and TSA (black line in Figure 4.17) have shown a periodic coupling approximately

every 20 years (positive correlations greater than 0.5). However, from the 1970s to the first decade of 2000, both ocean basins were less coupled. From the second decade onwards, the correlations present higher values again, which indicates return to coupling. Concerning the moving correlations between the TNA and the STSA (blue line), there are frequent changes in the SST behavior, but with correlation values that do not exceed ±0.5. A change in the correlation behavior from positive to negative is also observed from 2010 onward, and it is clear the increase of negative values with time.

On the other hand, the TSA and the STSA (red line in Figure 4.17) are mostly uncoupled (values ranging around ±0.25). Nevertheless, looking to breakings in this time series correlation, an important shift around 1979 is noticed, which becomes negative. In other words, while the TSA region turns warm, the STSA becomes cold at the same time.

The decoupling between STSA and TSA and TNA occurs from 1950 to 1980, period associated with climate shift in the PDO and AMO time series accordingly to several authors (Venrick et al., 1987; Zhang et al., 1998; Deser et al., 2004). Besides, in this same period and since 1977, also occurs a significative increase in the SST of the Indian and the Pacific Ocean (Deser et al., 2004), and a change SAMS period (Carvalho et al., 2011).

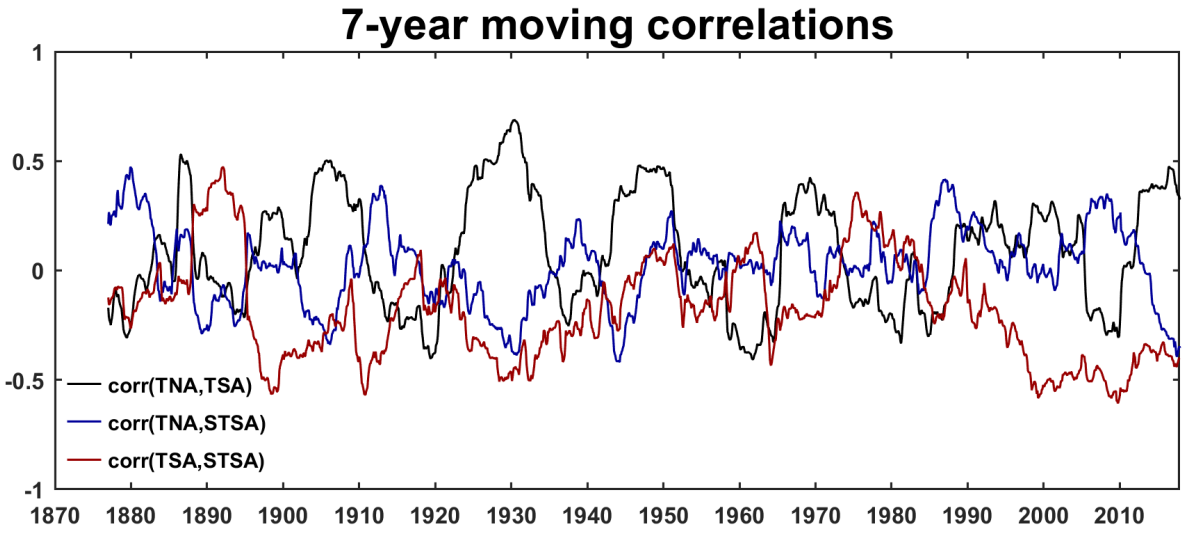

Figure 4.17: 7-years moving correlation of the Atlantic regions: TNAi-TSAi (black), TNAi-STSAi (blue) y TSAi-STSAi (red).

During the 1979-1981 period, the Amazon Basin was affected by an extreme drought event related to an increase of the SST in the TNA region (see Table 1 in Espinoza et al.,

2019). Furthermore, in the 1970s, the AMO index present negative values (cold phase), and the TNA and STSA shows a transition (from negative to positive values), while the TSA has positive values at the beginning of the decade and negative values at the end of the 1970s (see Figure 4.16). This increase in the temperature of the TNA and decrease in the TSA is known as the Atlantic dipole (positive dipole). When the SST of the TNA is warm, upward mass motions are generated over the Atlantic and subsident motions of dry air are seen over the north and northeast region of the Amazon, inhibiting cloud formation and decreasing precipitation (Deser et al., 2010). On the other hand, Silva Dias et al. (2013) reported an increase of daily rainfall thresholds on the Southeast of Brazil from that period, which in turn is related to the local SST (STSA), and the increase in the rainy period of the SAMS. However, although it seems that there should be a (positive) coupling between both Atlantic regions (TNA and STSA), it was not observed.

To further analyze the relationship between the different Atlantic regions, a cross-wavelet coherence between them is computed. Figure 4.18 shows the cross-wavelet coherence between the time series of the Atlantic indices (TNAi - TSAi, TNAi - STSAi, TSAi - STSAi), where the regions of highest coherence (shaded) tend to red color, and the significance of coherence is plotted in black contour. Black arrows plotted within the diagram indicate the relationship conditions between the Atlantic regions analyzed. While east-pointing arrows indicate in-phase behavior, the west-pointing arrows indicate out of phase (opposite phase) behavior. Similarly, North-pointing arrows indicate that the peaks in the first Atlantic region lead the second Atlantic region; south-pointing arrows indicate that the second Atlantic region lead peaks in the first Atlantic region.

Following the above considerations, the TNAi and the TSAi, for instance, are in phase and centered in the frequency of 3-4 years (interannual variability) during 1880-1891, 1925-1932, 1988-1990, and from 2010 periods (red box), as shown in (Figure 4.18a). From these periods, 1880-1891 and 1988-1990 are shown that the TSA is leading (arrows in $\sim$-45°). These results are consistent with our previous results, where the TNA and the TSA are positively coupled (see Figure 4.17). In other words, both regions are warm or are cool at the same time. Thus, according to the coherence wavelet, the warming (cooling) of the TSA led to the warming (cooling) of the TNA in that period. Between 1970 and 1990, out of phase behavior is observed between both ocean regions in the frequency of 11-12 years.

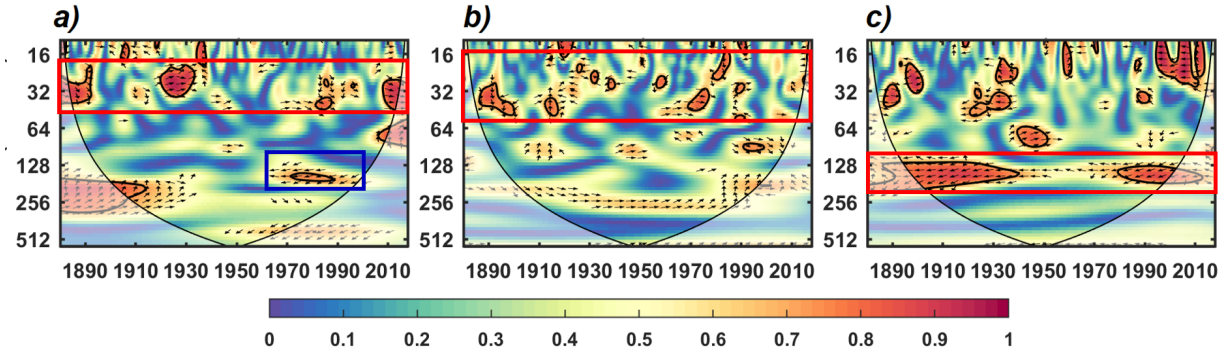

Figure 4.18: Cross-wavelet coherence between (a) TNAi-TSAi, (b) TNAi-STSAi, and (c) TSAi-STSAi. The black lines limit the cone of influence (COI). The color bar indicates the power ranges from blue (low coherence) to red (high coherence). 95% confidence for the coherency are plotted as contours in black. Black arrows indicate the phase relationship of the two time series in time-frequency space.

This is consistent with the negative coupling between both Atlantic regions in 10-years moving correlation (see Figure A.1). Until 1920, a significant in-phase relationship was observed in a frequency of 16-20 years between both time series, where TNA leads TSA (arrows in ∼-45°; blue box in Figure 4.18a), consistent with coupling between them in that period (20-years moving correlation, Figure A.2).

On the other hand, the relationship between TNA and STSA have a high coherence in specific time periods (e.g., 1890-1905, 1912-1918, 1925-1940, 1965-1977, 1978-1985, 1988-1992), in the frequency of 1.5-5 years, as is shown in the red box of the Figure 4.18b. However, the relationship between them is very variable, showing in-phase behavior during 1969-1977 period, a leading of the TNA over STSA in the 1915-1920 period, and a leading of the STSA over TNA in the 1890-1900 and 1980-1985 period.

Finally, between TSA and STSA (Figure 4.18c), there is a high and significant coherence in the frequency of 10-20 years (red box), except during 1945-1980, coinciding with a cold phase of the PDO. This coherence also indicates an out of phase behavior between both time series, where the STSA is leading in the most of the significant area. The out of phase behavior shows that the SST of both ocean regions move in the opposite direction mostly in ∼20 years, where warming (cooling) of the STSA leads to a cooling (warming) of the TSA. This is consistent with the negative correlations between TSA and STSA, showed in the Figure 4.17 and Figure A.2.

4.3.2 *The relationship between the Pacific and Atlantic Ocean SST*

Besides the connection between the different Atlantic regions, the Equatorial Pacific has shown signs of a connection with the Atlantic (put some references here). Figure 4.19 shows the 7-year moving correlations between the Atlantic and the Pacific indices to assess the periods in which both ocean basins were connected (positive/negative correlations).

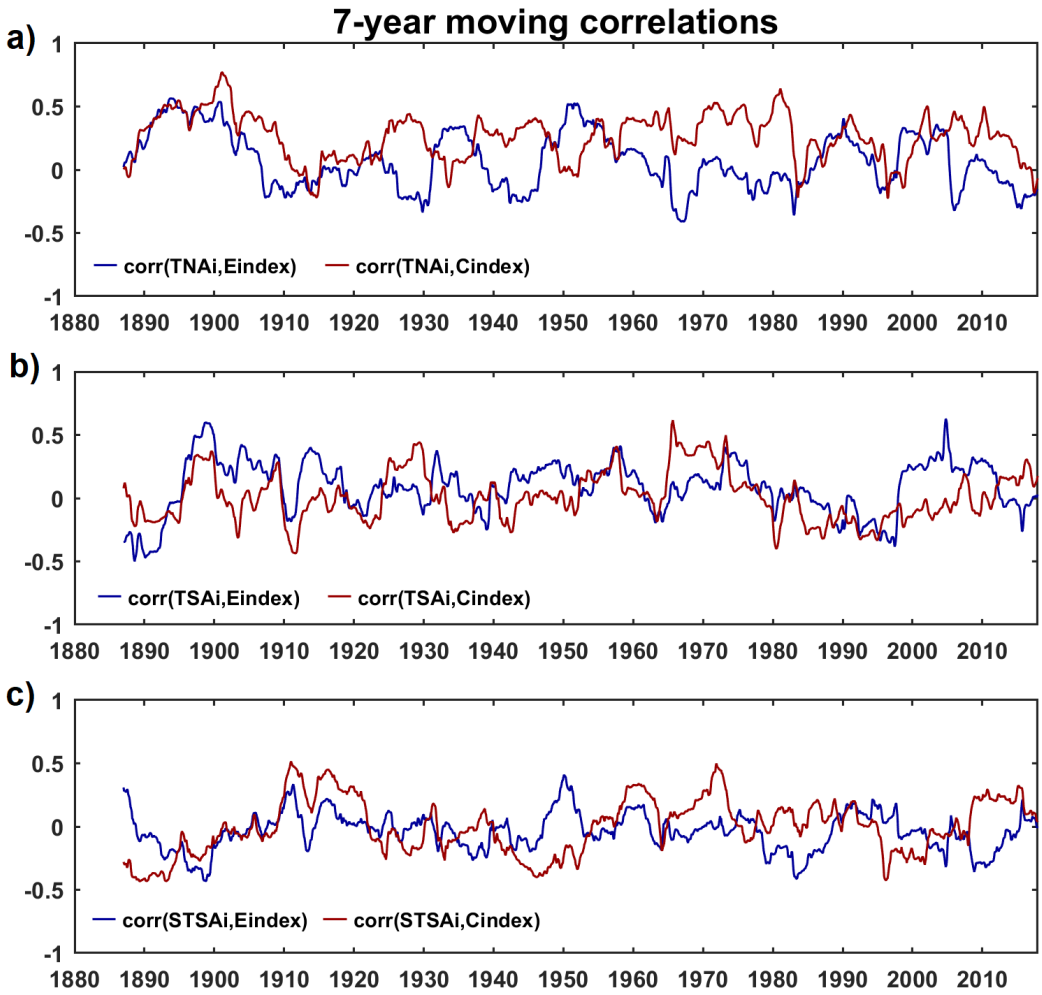

Figure 4.19: 7-years moving correlation between E index (blue) and C index (red) against (a) TNAi, (b) TSAi, and (c) STSAi.

Starting with the TNA against the E and C indices (Figure 4.19a), a periodic behavior in the correlations is clearly evidenced. The TNAi is more correlated with the Central Pacific region (C index), presenting mostly positive values. Consequently, the TNAi and C index are consistent with drought events in the Amazon Basin influenced by a simultaneous abnormal warming of the SST over the Tropical North Atlantic and the Equatorial Pacific (El Niño event). The 1980-81 and 2010 years (see Table 1 of Espinoza et al., 2019),

for instance, coincide with positive SST anomalies in the Central Pacific region (Timmermann et al., 2018; Freund et al., 2019) followed by warm Tropical Atlantic. Although the 1995 (strong positive C values), 1997-98 (strong positive E values), and 2015-2016 (strong positive E values) drought events on the Amazon Basin are due to the influence of El Niño and warm TNA, the behavior of the correlations in these periods show no evidence of a strong simultaneous connection between both oceanic regions.

Correlations peaks between TNAi and C index are also observed in 1892-1895, 1898-1901, 1971-1972, 1975 and 2002 years. These results suggest a greater connection between the Tropical North Atlantic and the Central Pacific region, compared to the Eastern region. In addition, during other years, as those related to the recorded drought years, there was a simultaneous connection between both ocean basins, but several factors led to no such event unfolding. An additional cross-correlation analysis (not shown) reveals that both behaviors would have similarities with a lag time ($r = 0.45$), which means that the behavior of the TNA-C Pacific connection presents a similar pattern with the TNA-E Pacific connection, but with a delay of 3.5 years.

Concerning the TSAi (Figure 4.19b), the behavior of the correlation oscillation in time suggests a connection between the Eastern Pacific and the TSA (E index and TSAi). However, low correlations values are observed, indicating that there is no connection between both ocean regions. Only two positive peaks in the period 1897-1900 and 2004 are noticed. On the other hand, the connection between the TSAi and the C index is more variable. The correlations show high negative and positive peaks, one of them around 1965 (positive correlation), and other two in the years of 1911 and 1980 (negative correlations). This last peak is associated with an anomalous warming condition in the Central Pacific (Freund et al., 2019), and indicates that during this period, the TSA maintained a cold SST. Additionally, although the flooding in the northeast of the Amazon basin in 2012 was related to La Niña event associated with a warm TSA (Espinoza et al., 2013; Satyamurty et al., 2013), there are no correlation between TSA and E/C indices during that period. However, both E index and C index show approximately the same correlation values with TSA in that period (crossing point near to zero; Figure 4.19b).

Finally, the correlations between the SST of the STSA and the Pacific region (Figure 4.19c) also shows differences between the Central and the Eastern Pacific region. In the

case of the STSA and the Eastern Pacific, a connection between both ocean basins is shown every ∼40-50 years (positive correlations). In contrast, the correlations between the STSA and the Central Pacific show a periodic connection behavior every 60-70 years, approximately. Over the time series, it is observed that both E and C indices have similar behavior in their respective correlations with STSA. However, the C index shows high correlation values. The most significant periods are 1910-1912, 1915, 1971-1972 years, when in the last one period, the Central Pacific showed warming (Freund et al., 2019). On the other hand, periods such as 1888-1893 and 1995-1996 show that the SST of the Central Pacific and the STSA had opposite signals. The last period also coincides with the warming period of the Central Pacific in 1994-1995 (Timmermann et al., 2018; Freund et al., 2019). Besides, during the 1982-1983 period, opposite signals between the Eastern Pacific and the STSA are shown. This time also coincides with warm Eastern Pacific conditions (Timmermann et al., 2018; Freund et al., 2019). These correlations suggest that during those periods, the SST of the STSA region was cold.

Figure 4.20 shows the cross-wavelet coherence between the Atlantic (TNAi, TSAi, and STSAi) and the Pacific (C and E) indices, where the regions of highest coherence (shaded) tend to red color and the significance of coherence is plotted in black contour. As noted in the previous section, the black arrows indicate the phase relationship between the Atlantic and the Pacific region. However, in this case, north-pointing arrows indicate that the peaks in the Atlantic index lead the peaks in the Pacific index, and south-pointing arrows indicate that peaks in the Pacific index lead the peaks in the Atlantic index.

Considering the TNA region (Figure 4.20a), there is high and significant coherence with the East Pacific in the frequency of 3-5 years for 1890-1920, 1930-1940, and 1960-1990 periods, when the TNA leads the peaks in the Eastern Pacific SST. In the contrary, during 1965-1982, an out of phase relationship is observed (arrows pointing to southwest) in the frequency of ∼10 years. During this period, the correlations between both basins showed a neutral behavior; that is, low correlations values (Figure 4.19a).

When Central Pacific region is considered for the analysis, the Figure 4.20b shows that both ocean basins have remained in-phase in the frequency of 3-5 years, in several stages, when mostly the TNA leads the variation in the Central Pacific SST (∼45° arrows). From 1950 until the end of the 1990s, there is in-phase relationship in the frequency of 10 years.

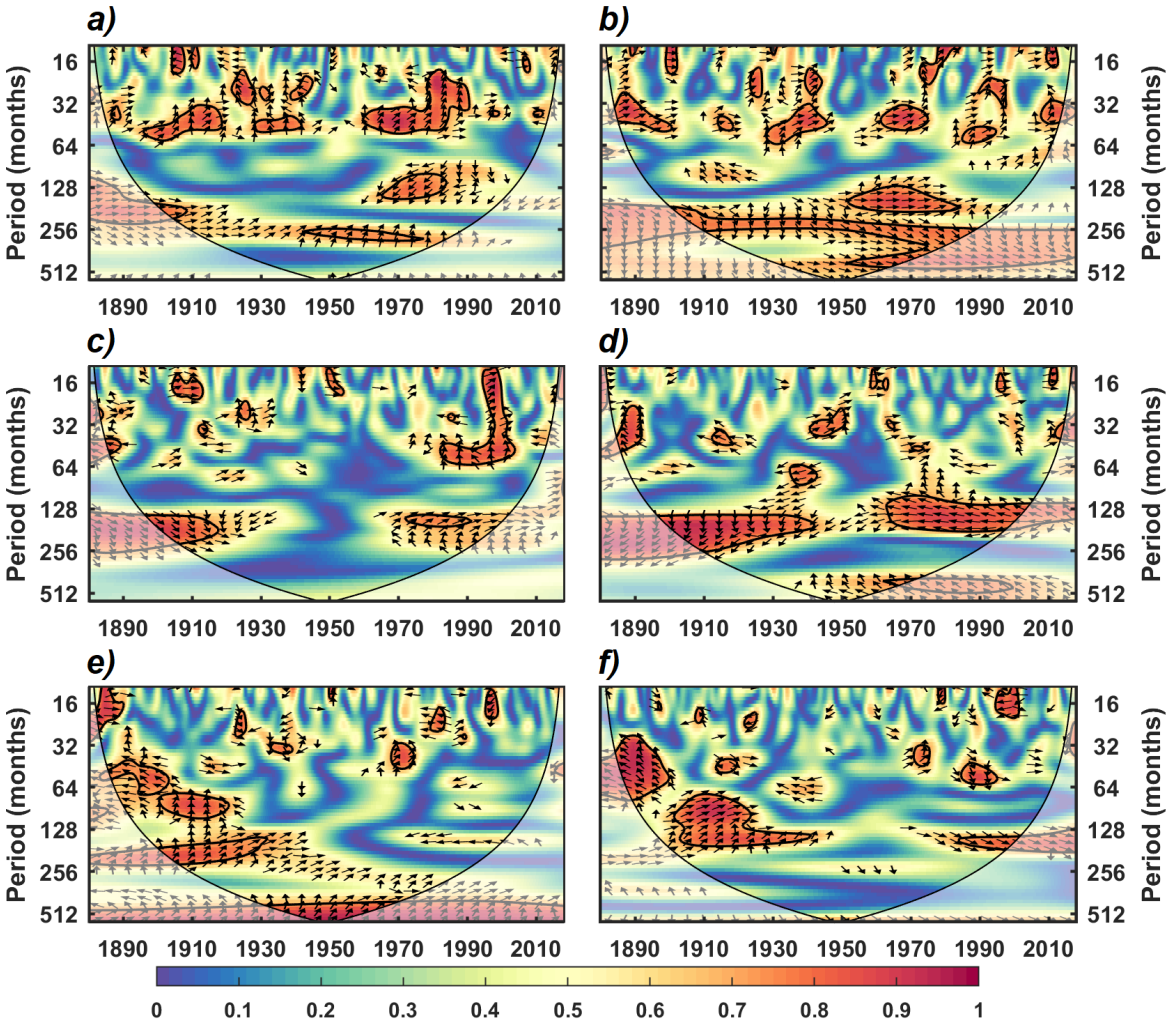

Figure 4.20: Cross-wavelet coherence for TNA (a,b), TSA (c,d), STSA(e,f) with E index (left) and C index (right), respectively. The black lines limit the cone of influence (COI). The color bar indicates the power ranges from blue (low coherence) to red (high coherence). 95% confidence for the coherency are plotted as contours in black. The arrows indicate the phase relationship between two time series in time-frequency space.

This is consistent with a coupling period between both oceanic regions (see Figure 4.19a), more noticeable in 10-years moving correlations (Figure A.3). In low-frequencies (more than 15 years), there is a high coherence within the interval of significance between the TNAi and the Central Pacific, when the Central Pacific region leads the TNA, and an in-phase relationship between them from 1950 onwards.

The relationship between the TSA and the Eastern Pacific region is shown in Figure 4.20c. Significant relations are observed in high-frequencies in specific periods. Between 1995 and 2000 it is observed that the E index leads TSAi in the frequency of 1-5 years

(interannual variability), and in 1980-2000 in frequency ranging in 4-5 years. These periods corresponds to a change in relationship between the Pacific and the Atlantic, from a decoupling to an increase in negative coupling (see Figure 4.19b). In low frequency (∼10-11 years), it is observed that the TSA and the Eastern Pacific are in-phase during the 1970-1990 period when the TSA leads the peaks of the Pacific region (arrows pointing in (∼45°). However, from the beginning of the time series until 1920, an influence of the Eastern Pacific in the TSA is shown (arrows in (∼-45°).

Figure 4.20d shows an out of phase relationship in frequencies of 10 to 20 years between the TSA and the Central Pacific. However, for the 1940-1960 period, the relationship was in-phase for higher frequencies (∼2-3 years). The relationship in low frequencies reveals that the Central Pacific is the one that leads the TSA in the 1880-1940 period.

The relationship between the STSA and the Pacific shows an out of phase relationship until the beginning of 1900. For instance, between both regions (STSA - East Pacific, and STSA - Central Pacific), significant coherence is noticed in the frequency of 3-4 years. In low frequency (∼20 years), the STSA and the Eastern Pacific show in-phase relationship during 1880-1930 period, when the STSA is leading (mostly arrows in 45°). In frequencies $>$ 50 years, also STSA leads the East Pacific. This is consistent with was mentioned above, when more than 50 years periodicity in the coupling between both regions is detectable (see Figure 4.19c for more details).

The STSA and the Central Pacific have been shown in-phase relationship in frequencies ranging between 5 to 10 years from the early 1900s until 1950, when the STSA leads (arrows in 45°). This is also consistent with the coupling relationship between them for that period (see Figure 4.19c). Nonetheless, this is reversed since 1980, when the Central Pacific leads to the STSA peaks (arrows in -45°). The period between this phase changes shows no apparent relationship at any frequency for that series.

4.4 Influence of the SST on the precipitation

4.4.1 Interannual variability of the SST associated with rainfall in the Amazon.

Several authors conducted many studies on the influence of the STT on rainfall over South America, including the Amazon Basin. Over South America, a recent paper of Cai et al. (2020) showed the different ENSO flavors impacts in precipitation and temperature. Specifically on the Amazon, Espinoza et al. (2019) well-summarized the impact of the ENSO region and the Tropical Atlantic in extreme precipitation events. In this section, the relationship between the SST conditions (ENSO and Atlantic regions) and the extreme precipitation events are analyzed through the correlations between the standardized anomalies of precipitation and five different SST indices [E and C index, for the Pacific region, and the TNAi, TSAi and STSAi for the Atlantic region] considering the 1940-2010 period.

The correlation maps for the five indices are presented in this section, with values exceeding the 5% significance level in hatched contours. The computations are made for the following seasons: the onset (Oct-Nov), peak (Dec-Feb), and demise (Mar-Apr) of the SAMS seasons and, finally, the dry absence of SAMS (May-Sep). These correlations show the positive (negative) influence of the SST on precipitation, where an increase in the SST triggers an increase (decrease) in rainfall values, contributing with flood (drought) events.

In addition, Appendix B presents a comparison between three precipitation databases (TRMM, HyBAm and GPCC) to discuss differences and similarities in the correlation results for the 1998-2009 period.

E index

During October-November, correlations between precipitation and the E index (Figure 4.21) show significant positive (blue) values over most of southeastern South America, southern Chile, northern coast of Peru, and coast of Ecuador; while negative values spread in the central east and northeast of South America, and in the central west of Argentina. The Eastern Pacific impacts the Amazon Basin with negative correlations in the eastern part of the basin. These correlations spread towards the north of Amazon Basin during December-February, contributing in droughts over these regions. Negative correlations are also observed in the central Andes (South of Bolivia), due to stronger mid-level westerly

flow (Vuille et al., 2000; Garreaud and Aceituno, 2001; Cai et al., 2020). In the other hand, positive correlations were displaced towards southern Brazil and central Argentina. Correlation values diminish throughout March-April. However, the Peruvian coastal region is still influenced by strong positive correlation, as occurred in the extraordinary 2017 coastal El Niño (Garreaud, 2018; Peng et al., 2019). Significant negatives values remain in the southeast of the Amazon Basin, and positive correlations are observed in southeastern Brazil and southern Argentina.

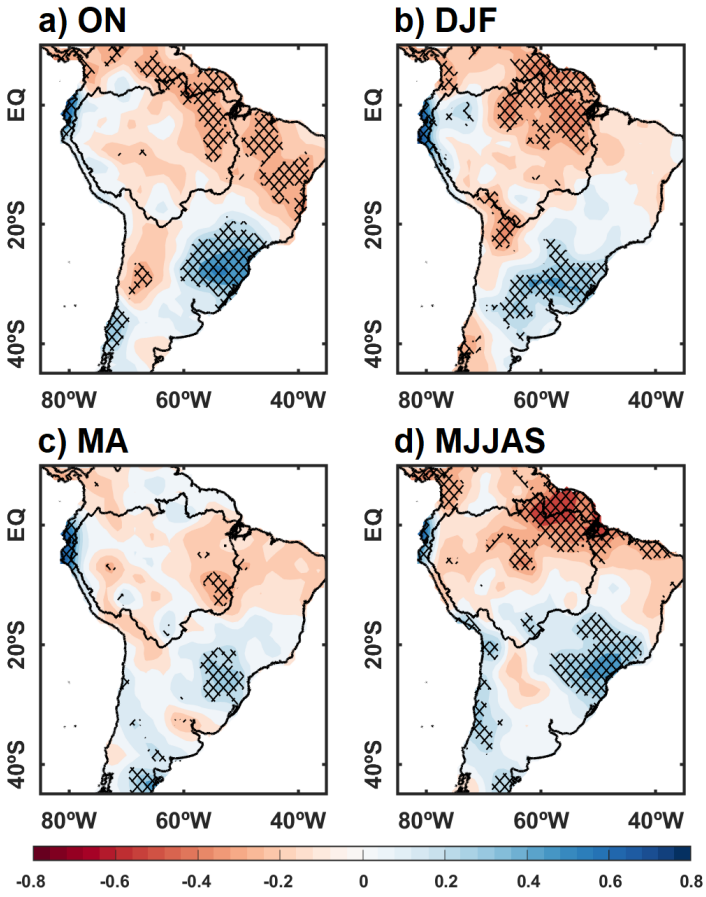

Figure 4.21: Correlation between the South America precipitation against the E index (Eastern Pacific) for the a) Oct-Nov (ON), b) Dec-Feb (DJF), c) Mar-Apr (MA), and d) May-Sep (MJJAS) period. Blue (red) shadings indicate positive (negative) correlation, where statistically significant values (exceeding the 5% significance level) are plotting in hatching. Precipitation data used are from GPCC for the 1940-2010 period.

Finally, during May-September, significant negative correlations are displaced northward. Negative correlations are located in the central, north and northeast of the Amazon Basin, while positive areas spread over the Southeast of Brazil, central and north of Chile. Positive correlations are still noticeable in northern coast of Peru and coast of

Ecuador, as previously discussed by Horel and Cornejo-Garrido (1986); Goldberg et al. (1987); Cai et al. (2020), among others. This influence generates deep convection over these regions.

C index

Concerning the C index (Figure 4.22), it presents significant positive correlations during the onset of the SAMS (Oct-Nov) in the southern Chile and southeastern part of South America, while negative values remain over North and northeastern South America, as discused by Cai et al. (2020). In comparison to the E index influence, positive correlations extend southward, resembling the Ronchail et al. (2002) findings. Negative correlations are displaced and intensified towards the North in the peak of the SAMS season (Dec-Feb). Significant negative correlations are located in the North of South America, including North and Northeast of the Amazon Basin. These negative values are consistent with Poveda et al. (2001) and Acevedo et al. (1999), who found a decrease in convection due to land–ocean thermal contrast, followed by subsidence due to convection over the ITCZ. Positive correlations are located in Uruguay, central-east of Argentina, and in the South and Northeast of Brazil. Moreover, the C index shows strong influence over the tropical Andes area during this period, in agreement with previous works (e.g. Vuille et al., 2000; Lavado-Casimiro and Espinoza, 2014; Sulca et al., 2018).

The significant correlation is vastly decreased during the demise of the SAMS season (March-April), with slightly negative values over North and Northeast of Brazil, and eastern and southwestern of the Amazon Basin. This weaker influence is also observed during the May-September season, with smaller positive correlations over the southeastern Amazon Basin. The Central Chile also presents positive correlations, consistent with Montecinos et al. (2000), and Masiokas et al. (2006), who found that this influence is due to blocking in the southeast of Pacific, causing an increasing of storms. Likewise, southern Argentina presents positive influence in the Central Pacific and Eastern Pacific for this period (see Figure 4.21). Negative values are seen over the northwestern portion of South America, and the northeastern of South America (including north and northeast of the Amazon Basin).

Overall, the influence of the ENSO (Eastern and Central Pacific) in droughts in the Amazon Basin occurs mainly during December-February in agreement with several stu-

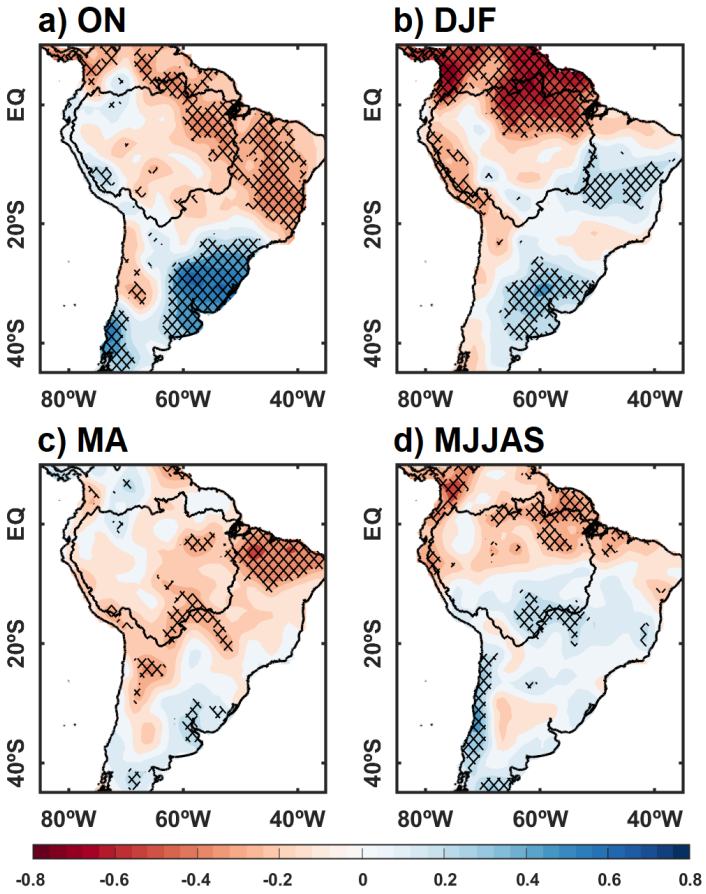

Figure 4.22: As in Fig. 4.21, but for C index (Central Pacific).

dies (e.g. Ropelewski and Halpert, 1987; Rao and Hada, 1990; Uvo et al., 1998; Grimm and Tedeschi, 2009; Cai et al., 2020; Aceituno, 1988, , and references therein). The main teleconnection that produces extreme events (e.g., droughts) is the tropical-tropical teleconnection, in other words, the anomalous displacement of the Walker circulation, where the central Pacific seems to be the most influential region (Grimm, 2009, (Cai et al., 2020).

TNAi

Recent studies highlight the role of the tropical Atlantic in the last extreme events that occurred, for instance, over the Amazon region. Indeed, positive trends in the SST showed in the previous section yield clues about how frequent those events will be in the years to come. In this subsection, we will discuss how anomalous conditions in the tropical Atlantic impacts precipitation over South America and the Amazon region, considering different periods. In the onset of SAMS season, only significant negative correlations are observed

in the north of Amazon Basin (Figure 4.23). These correlations are displaced towards the northeast of the basin during the peak (December-February), while weak and positive correlations appear in the central Brazil and Uruguay. Negative correlations indicate low rate of precipitation reducing intensity in northeast moisture transport into the Amazonia (Marengo et al., 2008).

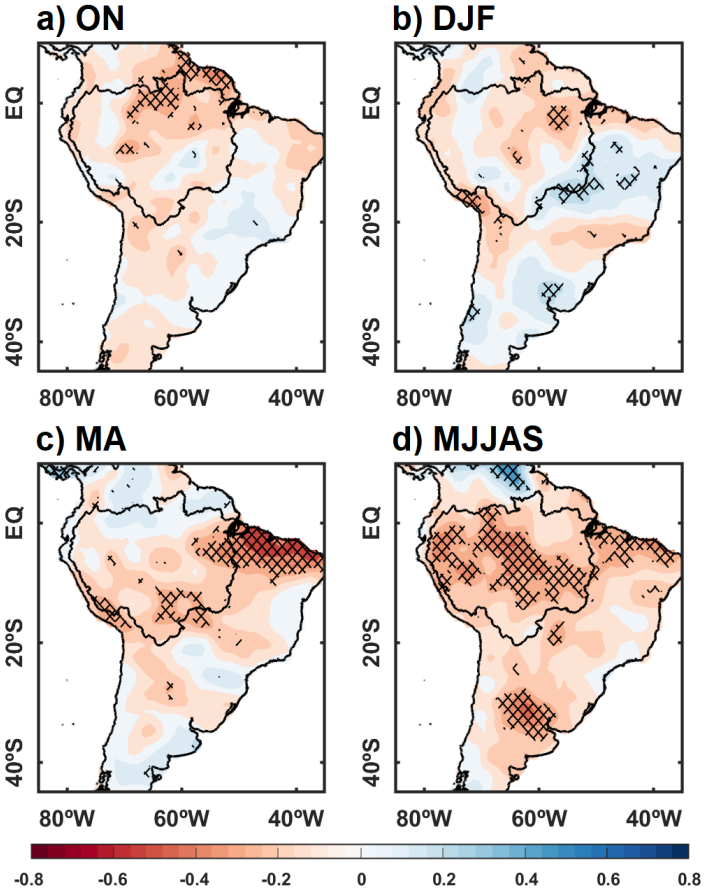

Figure 4.23: As in Fig. 4.21, but for TNAi (Tropical North Atlantic).

Unlike the SST conditions from the Pacific Ocean, the TNA influence over South America is significant mostly during the late of SAMS season and the May-Sep period. Strong and significant negative correlations are noticed in the North and Northeastern of Brazil and southern Amazon Basin during this period. Likewise, significant negative values are observed over the central continent, covering also the Amazonian. In fact, the last two extreme events over the Amazon Basin (occurred in 2005 and 2010) was strongly modulated by warm conditions in the tropical North Atlantic. These extreme events, as documented in recent papers, occurred during the March-September period (Espinoza et al., 2011;

Marengo et al., 2011). The main phenomenon that explains such events is related to the warm Atlantic condition, which creates a mechanism that does not favor the transport of moisture from the ocean towards the Amazon Basin, reducing convective development and precipitation (Marengo et al., 2008). Negative values are also observed in central Argentina and North and Northeast of Brazil, while positive correlations are seen in the most part of the north trip of South America.

TSAi

Concerning the TSAi (Figure 4.24), in the onset of the SAMS period, positive (negative) correlations are limited in the southeastern (northeastern) of Brazil. In the peak of the SAMS (Dec-Feb), there are negative values spreading in the north part of South America, while positive correlations are mainly located in northern Brazil and Uruguay. These correlations are intensified and displaced eastward during the late SAMS season (March-April). Significant negative correlations are observed in the northeastern part of South America, while positive correlations are located in the northeastern of Brazil, which is opposite to what was observed for the TNAi (see the third panel of Figure 4.19c).

As observed for correlations calculated using the TNAi, the TSA influence over South America is predominant during the May-September period for most of the continent. There are predominantly positive correlations over the northeastern of Brazil regions, covering the north and central Amazon Basin, while significant negative values are found in the Central and South Regions of Brazil and southern Argentina. In addition, the south and the extreme southeast of the Amazon Basin presents negative correlations.

STSAi

Unlike other indices presented above, significant correlations between STSAi and precipitations (Figure 4.25) are scattered in South America all year-round. However, correlations are noticed during the peak of the SAMS season (December-February) and during the SAMS absence (May-Sep). In the peak of the SAMS season, positive correlations are observed in the Central and North of South America, covering also the southeast, central and north of the Amazon Basin. In the other hand, negative correlations (weak values) are located in the Northeast of Brazil and the southern tip of South America. Significant correlations are vastly decreased during the demise of SAMS season (March-April), where only negative correlations are noticed in the north coastal region of the Northeast of Bra-

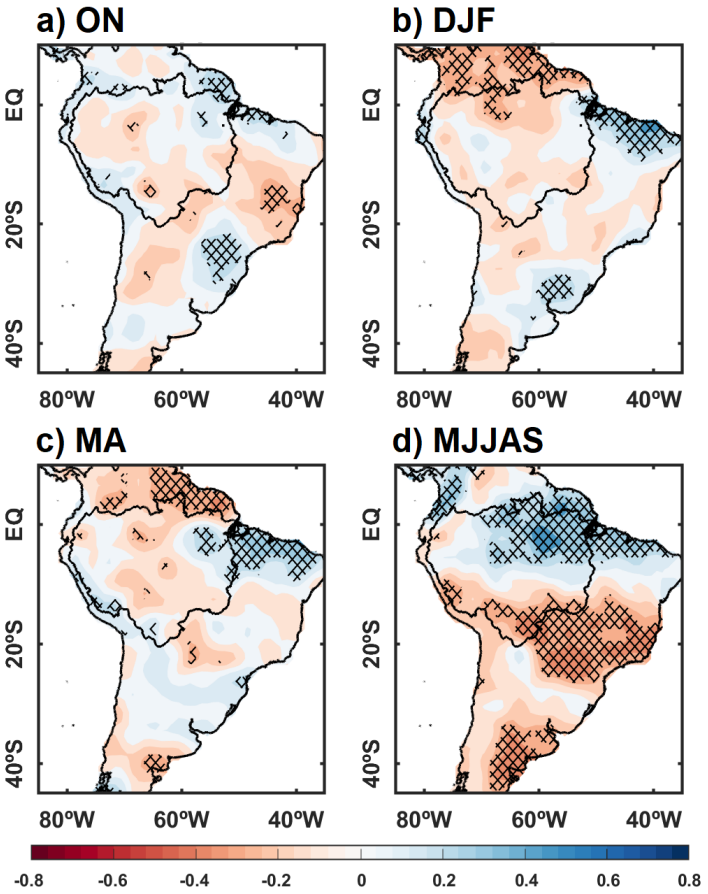

Figure 4.24: As in Fig. 4.21, but for TSAi (Tropical South Atlantic)).

zil. This configuration is slightly changed during the May-September period, with negative correlations spreading over the North of South America, including the central and north part of the Amazon Basin.

4.4.2 Decadal and interdecadal variability in the Pacific and Atlantic, and the associated precipitation patterns in South America: A focus on the Amazon Basin

There are some previous studies that document the influence of the PDO and AMO on precipitations over South America and the Amazon as well (e.g. Marengo, 2004; Andreoli and Kayano, 2005; Kayano and Andreoli, 2006, 2007; Kayano and Capistrano, 2014; Chiessi et al., 2009; Levine et al., 2017, 2018; Martín-Rey et al., 2018, among others). Several studies have mentioned and pointed out that regions of South America are affected by both of those climatic oscillations, based on their cold and warm phases. For instance,

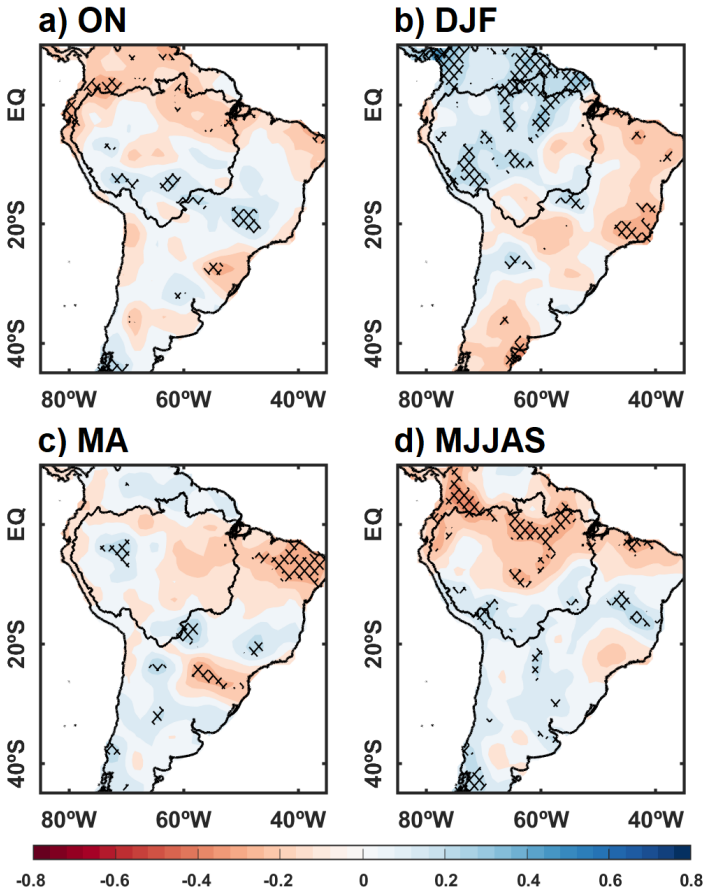

Figure 4.25: As in Fig. 4.21, but for STSAi (Subtropical South Atlantic).

Kayano et al. (2019) suggest the AMO and PDO play an important role in modulating the Walker and Hadley cells and the Rossby wavetrain pattern in South America. However, in this section, an analysis of the influence of PDO and AMO is made according to the positive (high PDO/AMO) and negative (low PDO/AMO) values in the 1940-2016 period. As documented in previous sections, and considering the that SAMS is the main driver of precipitation on broad South America, we consider the following phases: Onset of SAMS (October-November), the peak of SAMS (December-February), demise (March-April), and the absence of SAMS forcing (May-September).

Pacific Decadal Oscillation precipitation patterns

Figure 4.26 shows the precipitation composite maps considering the warm and cold PDO phases. We considered warm and cold PDO when the PDO values positive and negative, respectively.

The warm PDO (Figure 4.26a) during the onset of the SAMS (ON), is characterized by low precipitation in the east of South America and high precipitation in the south of the Amazon Basin. Low precipitation in east of South America during warm PDO is according to correlations between precipitation and C and E index (see Figure 4.21 and 4.22). These results suggest that during high PDO, ENSO influence is intensified in these regions in Oct-Nov, which is consistent with Andreoli and Kayano (2005) findings.

During the peak of the SAMS (Dec-Feb), negative values of prcipitation are located in the north and nortwest of the Amazon Basin, and positive values in the south of the basin ad east of South America (see Figure 4.26a, DJF). In this period, high precipitation is in agreement with positive correlations between precipitation and C index (see Figure 4.22), suggesting an intensification of ENSO influence during high PDO. Likewise, since STSA influences in high precipitation over all the Amazon Basin during Dec-Feb (see Figure 4.25, second row), PDO can generate precipitation differences within the basin.

In the demise of the SAMS (Mar-Apr), a precipitation dipole is formed within the continent, where negative anomalous precipitation is formed in the north region of South America, and the north of the Amazon Basin. In contrast, precipitation forms in the south region of the basin and southeast of South America. The negative anomalies regions in Amazon Basin are consistent with the results by Kayano and Andreoli (2007) for high PDO values. Moreover, the positive precipitation anomalies propagate to southeastern Brazil.

Finally, the dry period (May-Sep) is characterized by a significant area with negative anomalies centered in the north of South America, including north and northwest of the Amazon Basin. Moreover, positive anomalies are not noticed in this period. Significant low precipitation composite areas during warm PDO is similar to correlations between precipitation and C index (see Figure 4.22, fourth panel). These comparisons suggest that PDO may influence the intensity of the interannual index.

During periods of cold PDO (Figure 4.26b), precipitations have an opposite pattern in comparison with the warm PDO. The onset of the SAMS is characterized by dry regions in the south of the basin, while the regions with significant positive precipitation anomalies are not noticed in this period. Negative precipitation over south of the Amazon Basin suggests that cold PDO intesify (weakens) TSA (STSA) influence (positive/negative correlations between precipitation and TSA/STSA; see Figure 4.24 and 4.25).

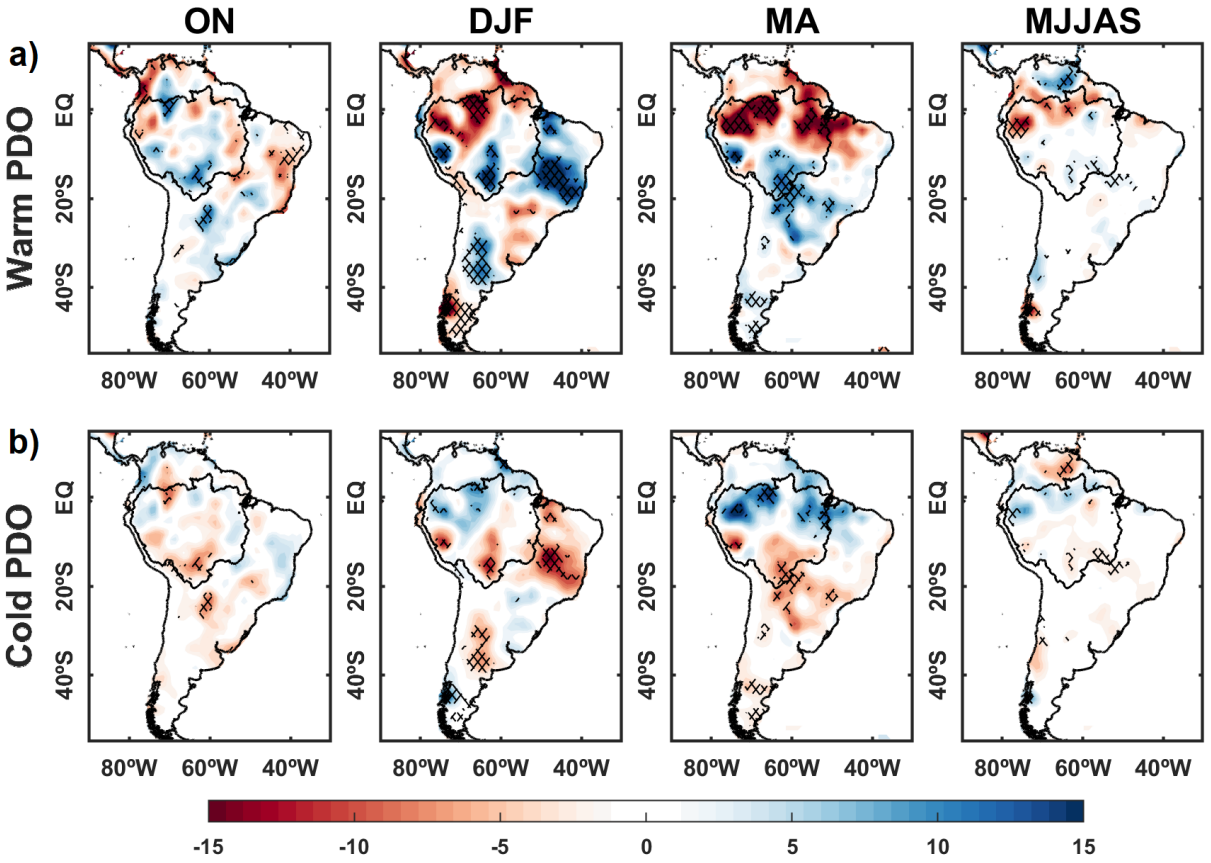

Figure 4.26: Precipitation anomaly composites (in mm/month) considering a) warm (positive) and b) cold (negative) PDO values, for the Oct-Nov (ON), Dec-Feb (DJF), Mar-Apr (MA), and May-Sep (MJJAS) period. Hatching filled area indicates the areas with 95% significance or above.

Towards the peak of the SAMS, significant negative anomalies regions expand to southeast of South America. Within the Amazon, there are specific regions of low rainfall in the west and south. Regions with positive rainfall anomalies are shown in the north of South America (north, and northwest of the Amazon Basin). High precipitation in the northern Amazon Basin is in agreement with scattered positive correlations between precipitation and STSAi (see Figure 4.25), suggesting an intensification of STSA influence in this region, during cold PDO.

The precipitation increases at the end of the SAMS, where significant areas (hatch-filled areas) with high precipitation is shown in a broad region of the north of the Amazon Basin and northeast of BraziL. Low precipitation in the south of the basin and the southeast of South America is noticed. Finally, during the absence of the SAMS, rainfall during the cold PDO are weak compared with other periods (∼-8 mm/month).

Overall, composites precipitation for warm PDO shows some regions similar to ENSO and STSA influence areas. Besides, regions in southeastern South America presents mostly high precipitation, and northern South America presents low precipitation, consistent with results found by Kayano and Andreoli (2007) for South America and Marengo (2004) for Amazon Basin. Besides, cold PDO shows no influence on absence SAMS, suggesting that the interannual influence during this period (ENSO and warm/cold subtropical Atlantic) could modify precipitation patterns without PDO intervention. These differences suggest that precipitation anomalies are more (less) intense when PDO and ENSO/STSA presents the same positive (negative) values.

Atlantic Multidecadal Oscillation precipitation patterns

AMO is the dominante mutidecadal variability pattern of the Atlantic (Levine et al., 2017; Martín-Rey et al., 2018). For instance, AMO is in positive phase since the beginning of 2000, favoring the intensification of droughts and wet events over South America and Amazon Basin. In fact, Levine et al. (2017) found a strong influence of the Atlantic on the multidecadal variability of ENSO. Then, as made in previous section, in this section we computed composite maps (Figure 4.27), concerning the positive and negative AMO phases.

Considering the warm AMO (positive values of AMO; Figure 4.27a), it is observed regions with negative precipitation anomalies at the onset of the SAMS period in the Southeast of South America, and specific areas in the center of the Amazon Basin. Low precipitation over southeast of the continent coincides with positive correlations areas between precipitation and C index (see Figure 4.22). These opposite values suggest that during the high AMO, the influence of the warming of the Central Pacific would be affected by this interdecadal variation.

During the peak of the SAMS, positive anomalies regions appear in the center of the Amazon, coincident with positive correlations between precipitation and STSAi (see Figure 4.25), suggesting an intensification of Subtropical South Atlantic influence. In contrast, the negative anomalies are located in the southern basin, and southeast of South America. Chiessi et al. (2009), found that during high AMO, SACZ is displaced northward, diminishing precipitation over La Plata Basin.

In the end of the SAMS (Mar-Apr), significant regions with negative anomalies are

observed in Uruguay (∼-10 mm/month). Negative anomalies in the central and northwest of the Amazon Basin are also noticed, with anomalies reaching values of -15 mm/month or less, modifying Central Pacific and TNA influence (see Figure 4.22 and 4.23). Regions with positive anomalies are shown in the east of South America and south of the Amazon Basin, similar to previous period (Dec-Feb), disintensifying the Central Pacic and TNA influence.

Finally, during the absence of the SAMS (May-Sep), the Amazon basin presents mostly negative rainfall anomalies, between -3 and -8 mm/month, where eastern region of the basin is significant. These results suggest that during high AMO, TNA influence is more intense over the Basin (see figure 4.23).

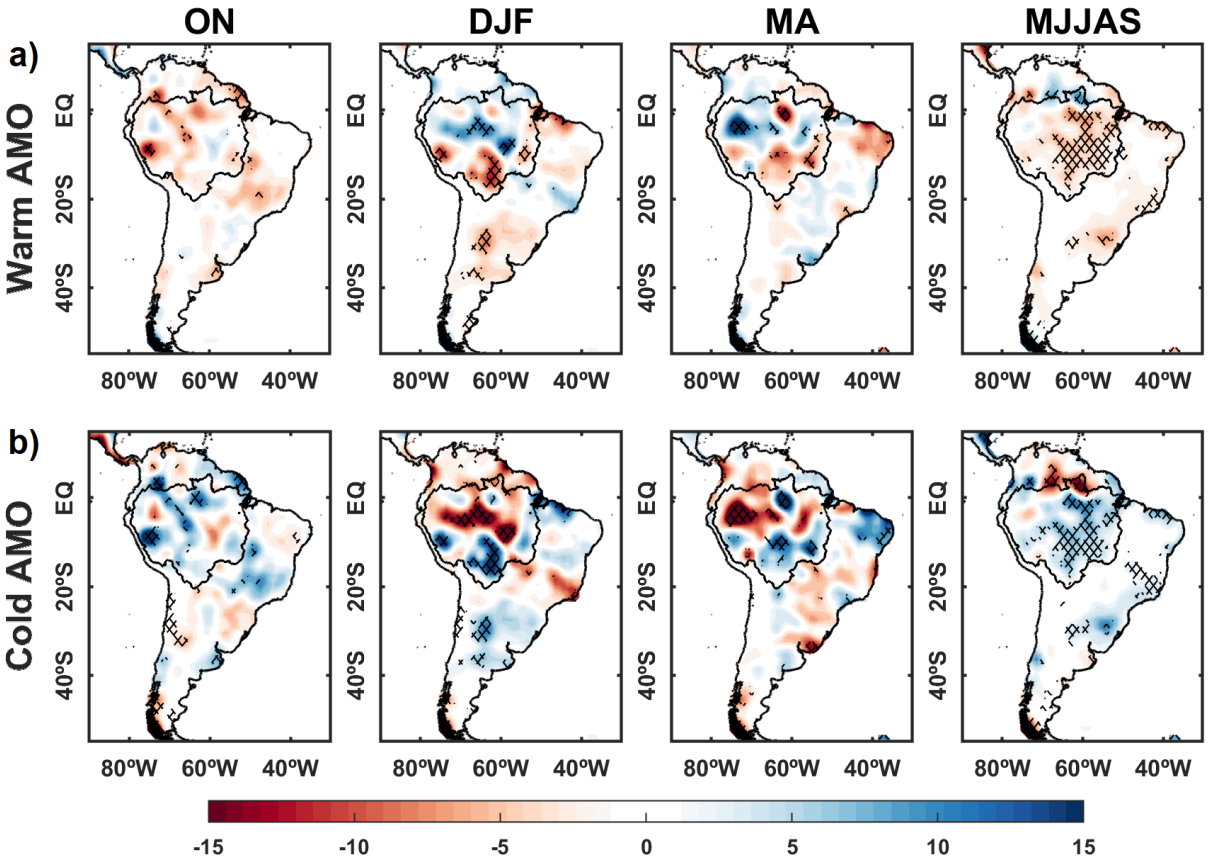

Figure 4.27: As in Fig. 4.26, but for AMO.

The years with cold AMO (negative AMO values; Figure 4.27b), also show opposite precipitation patterns in comparison with the warm AMO. During the onset of the SAMS (Oct-Nov), spread regions with low rates of rainfall anomalies, both positive and negative, are observed. In the peak of the SAMS (Dec-Feb), significant areas of positive precipitation

anomalies are shown in the the Northeast of Brazil and the south and southwest of the Amazon Basin. Negative anomalies are found in the north of the basin, coincident with the influence of the Central Pacific, TNA and TSA influence (see Figure 4.22 and 4.23).

At the end of the SAMS (May-Apr), positive anomalies are intensified in the northeast of Brazil and south of the Amazon Basin. In contrast, negative rainfall anomalies are located in southern of South America, including the north region of the Amazon Basin. Finally, during the absence of the SAMS (May-Sep), there are significant regions of low positive anomalies throughout the Amazon Basin (∼5 mm/month), except the extreme north; while positive anomalies occurred in the eastern side of northern South America, including the north of the Amazon basin, with anomalies of (∼8-10 mm/month) mm/month.

Overall, the AMO also influences mostly during the peak and the end of the SAMS. Negative (positive) precipitation over northeastern South America during MAr-Apr is consistent with results described by Levine et al. (2018), which indicates that high (low) AMO produces a ZCIT displacement to northward (southward), inhibiting (increasing) convection. This AMO phases (high, low) also modifies the SAMS configuration (northward, southward) and SACZ intensity (more intense, less intense), influencing in precipitation, as previously mentioned in this section.

4.4.3 Dynamical features associated with anomalous SST condition in the tropical Pacific and Atlantic

While the correlation analysis between the SST climate indices and precipitation time series over South America offered insights on how rainfall is affected during positive or negative phases of the aforementioned indices, a regression analysis assessed in this section will provide physical explanations about how circulation and rainfall are affected. In this section, moisture flux and divergence values regressions for each Pacific and Atlantic indices are shown. Positive (negative) values indicate divergence (convergence) and, therefore, represent a source (sink) region for moisture. In addition, the average zonal (5° S-5° N) and meridional (55° W-45° W) regressed vertical sections are shown in Figures 4.30 and 4.34, for the Pacific and Atlantic indices, respectively. Vertical sections exhibit the specific humidity, vertical velocity, and u,w (for Pacific) and v,w (for the Atlantic) vector winds regressed. Positive (negative) shaded values indicate downward (upward) movement; while

solid (discontinued) lines show positive (negative) values of regressed q.

E index

When the Eastern Pacific is warm (Figure 4.28), it is clearly seen a progression in intensity of the regressed values from the onset of the SAMS (Oct-Nov), reaching its maximum intensity during the late SAMS (Mar-Apr). October-November presents convergence flux regions in the Northern Hemisphere, for the Pacific (∼EQ-10° N), while divergence is noticed in South (∼EQ-10° S). This divergent flux is, additionally, observed in the central continent, with center in the northeast of Brazil. On the other hand, convergent flux is observed in southeast of South America, and the presence of intense moisture transport from the Amazon Basin towards southeastern South America and northern Argentina through the SALLJ following the eastern Andes is also observed. This feature was extensively discussed by several authors (e.g. Drumond et al., 2008; Arraut and Satyamurty, 2009; Alves, 2009; Boers et al., 2014).

Concerning December-February season, a strong convergence zone is established over the Equatorial Pacific, with a dipole formed over South America, characterizing the typical shift in the Walker circulation cell associated with stronger ENSO phases. Bersides, it is noticeable the presence of the SAMS over South America, with divergent flux over North Atlantic, moisture flux entering to Amazon Basin to southeast, and convergent flux over southeast of South America. This convergent flux, observed mainly with E index regression, could be also associated to the SACZ that is more persistent in warm phases of the ENSO (Carvalho, 2009a).

The demise of the SAMS (Mar-Apr) period shows the intensification of the convergent flux over Equatorial Pacific, and its displacement southward (∼5° N-5° S), in comparison with Oct-Nov. Thus, Equatorial Pacific is converted in a sink region of moisture during Mar-Apr. However, the dipole over South America is diminished, while the SAMS presence is disappeared and the convergence over southeast of South America is also diminished.

Moisture flux decrease in intensity during the absence of the SAMS over Equatorial Pacific, and South America (southeastward flux), associated with the SALLJ. This flux configuration indicates that Eastern Pacific also influence over the moisture distribution during the absence of the SAMS (May-Aug). Over the north of the Southeast Pacific Subtropical Anticyclone (SPSA) it is noticed a convergent flux accompanied a moisture

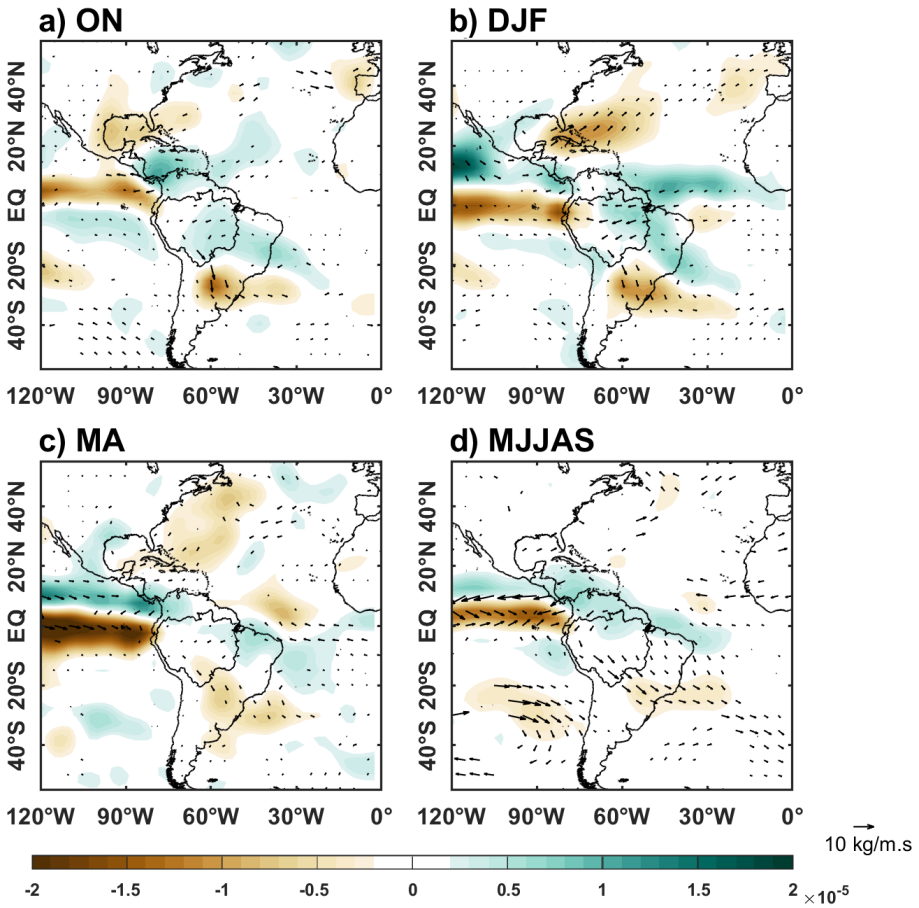

Figure 4.28: Regressed horizontal structure of vertically integrated moisture-flux (vectors) and its divergence (shaded) against the E index (Eastern Pacific) for the a) Oct-Nov (ON), b) Dec-Feb (DJF), c) Mar-Apr (MA), and d) May-Sep (MJJAS) period. Shaded divergence in $kg\ m^{-2}s^{-1}$ is shown by the legend. The moisture-flux reference vector is 10 $km\ m^{-1}s^{-1}$. Positive (negative) contours are solid (dashed). Dinamic structure data used are from ERA20-C for the 1940-2010 period.

flux with opposite direction, indicating that the intensity of the SPSA diminishes in this period influenced by Eastern Pacific anomalous condition.

The Walker circulation pattern is in agreement with the vertical structure of specific humidity, zonal and vertical velocity (Figure 4.30a) for a high-longitude cross-section between 5° S-EQ. Strong convection over the central and eastern Pacific is observed with subsidence in the eastern and western branches, for the peak and late of the SAMS, when this circulation is more intense. The western branches of this circulation are more intense compared with the eastern, where the Amazon Basin is located. During the absence of the SAMS it is also observed the Walker circulation, but less intense, evidencing the influence of the Eastern Pacific over the Amazon, even during this period. This circulation, with

subsidence over the Amazon, shows the influence of the Eastern Pacific and its circulation condition reducing precipitation over the Amazon, consistent with the correlation between E index and precipitation (see Figure 4.21), and also documented in a recent paper (Cai et al., 2020).

C index

Concerning the C index (Figure 4.29), dynamical features that mainly characterize the ENSO ´´Modoki" type is observed over the Equatorial Pacific. During the onset of SAMS, the dipole configuration influenced by strong ENSO over South America is noticed. In addition, extreme moisture convergence in the southeast of South America mainly resembles the strong precipitation when the central Pacific is warm. The moisture flux from the Amazon Basin towards southeastern Brazil and northern Argentina, suggesting the presence of the SALLJ acting in moisture distribution, as was observed in the Easter Pacific regressions, also described by Drumond et al. (2008) and Arraut and Satyamurty (2009). As discussed by Berbery and Barros (2002), the SALLJ influences moisture distribution over the La Plata Basin throughout the whole year, increasing its intensity during positive ENSO phases. Over the South Atlantic, an anticyclone configuration is observed, with strong intensified moisture flux, showing the influence of the ENSO located in the Central Pacific, contrasting with Venegas et al. (1997); Sun et al. (2017), among others. On the other hand, in the southern Pacific, flux from the southeast indicates that the intensity of the SPSA is diminished.

Opposite to the E index, during the peak of the SAMS it is observed that the convergence flux over the Southeast of South America is weaker. However, an increasing of divergent flux over the Northeast of Brazil is noticed, covering the north and northeast of the Amazon Basin. Besides, the SAMS flux looks weaked; however, its configuration is still observable, with moisture entering over the Amazon Basin from the northeast and going out to the south of the basin. The moisture flux patterns are maintained during the late of the SAMS (Mar-Apr), although the convergence (divergence) decrease in the southeast (northeast) of South America. Divergent flux in the northeast is displaced to south, and the statistically significant westerly moisture flux is entering into the Amazon Basin. Finally, in the absence of the SAMS (May-Sep), patterns show a decrease in the intensity of divergence over the northeast of the Amazon Basin, while the ENSO event in

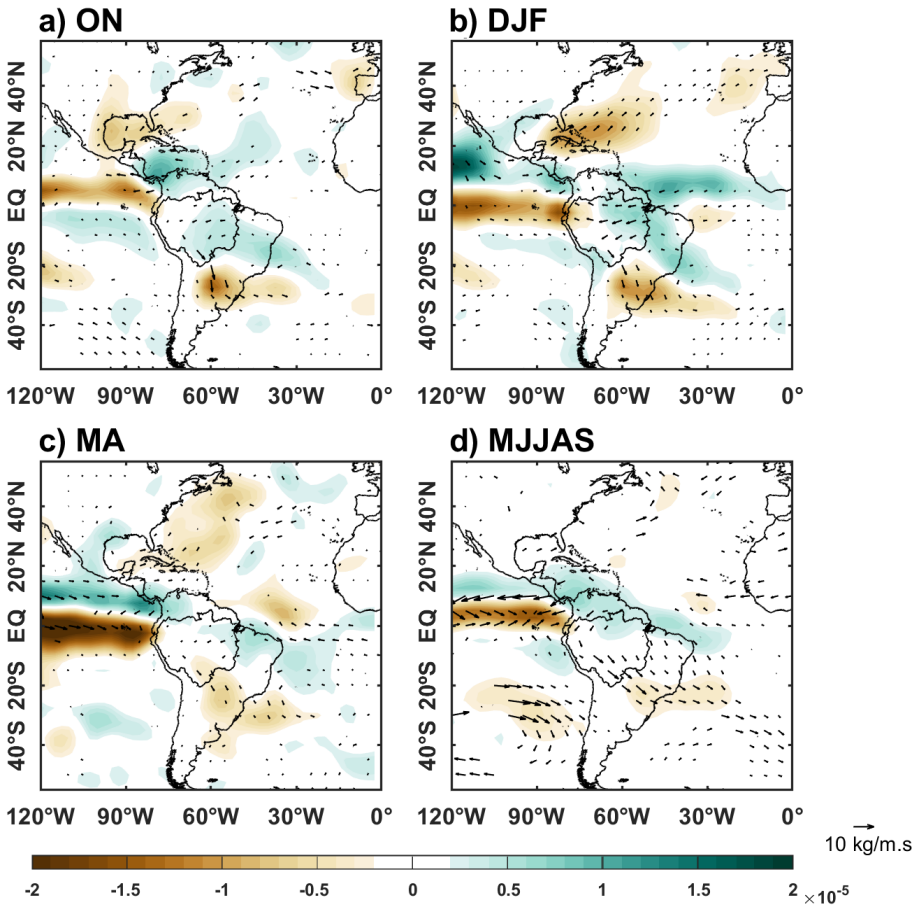

Figure 4.29: As in Fig. 4.28, but for C index (Central Pacific).

the Pacific is reaching its final. Also, the SPSA, located near of 100° W is weak (arrows in opposite direction), evidencing the influence of the anomalous Central Pacific in the SPSA in the absence of the SAMS.

Circulation patterns are affected by this configuration (Figure 4.30b), with changes in the teleconnection patterns affecting moisture distribution over South America. The Walker Circulation cell is now characterized by a double cell with an ascending branch over central Pacific and high level wind convergence. The descending branches usually associated with rainfall suppression are observed for both eastern and western flanks of the convective central region. The ascending branch is more intense during the Dec-Feb and Mar-Apr, while descending branches are more intense during May-Nov (western flank) and Mar-Apr (eastern flank). Nevertheless, low-level specific humidity (q) over the Amazon (∼70-60° W; contours) during Dec-Apr, indicates that, although there is descending circulation, the basin presents high moisture content, which could be associated to a local

generation of water vapor through evapotranspiration (Salati et al., 1978; Marengo and Nobre, 2009).

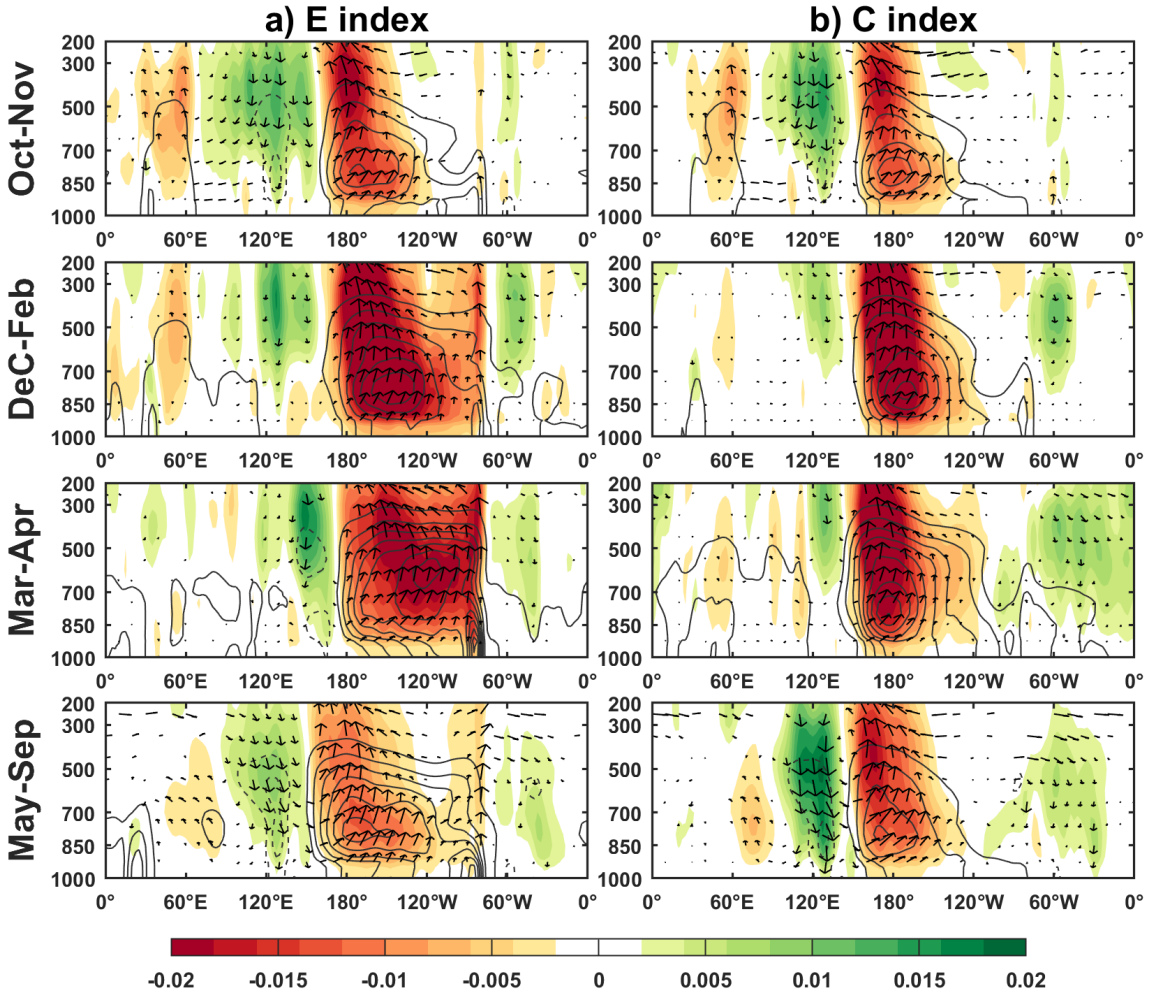

Figure 4.30: Regressed vertical sections of the zonal-vertical wind (u,w; vectors), vertical velocity (shaded), and specific humidity (contours) associated with the Pacific condition over South America. Averaged zonal from 5 °S - EQ vertical section. Contour interval is 1x10^{-2} $g\ kg^{-1}$ for specific humidity with solid (dashed) lines indicating positive (negative) values. The wind reference vector is 10 $m\ s^{-1}$. Wind fields are plotted only where either the u or w component is significant at the 95% level or greater, as estimated by t-Test.

TNAi

Under anomalous condition over TNA (Figure 4.31), the moisture source is located over the Tropical Atlantic Ocean during the Oct-Nov. This source sends moisture to northern and south Atlantic. In addition, the cyclonic circulation pattern in the Northern Hemisphere resembles the negative phase of North Atlantic Oscillation (NAO Hurrel et al., 2003), with less intensified trade winds and moisture convergence going towards South

America. In the Amazon Basin, moisture flux of the east of the Andes is observed going to southwards of the basin. Apparently, this flux converges over Uruguay and eastern Agentina, where a convergent flux region is noticed.

During the peak of the SAMS (Dec-Feb), the moisture source covers the north and northeast of the Amazon Basin, taking away the moisture of this region. The moisture subtraction of this region triggers the non-development of precipitation, consistent with the Figure 4.23, that shows negative correlations between TNAi and precipitation in the northeastern Amazon Basin during this period. Moisture suppression is also observed in the vertical-meridional cross-section of specific humidity and winds regressed (Figure 4.34a, second panel), with descendent winds and low specific humidity (contours) over the northeastern Amazon Basin (∼EQ).

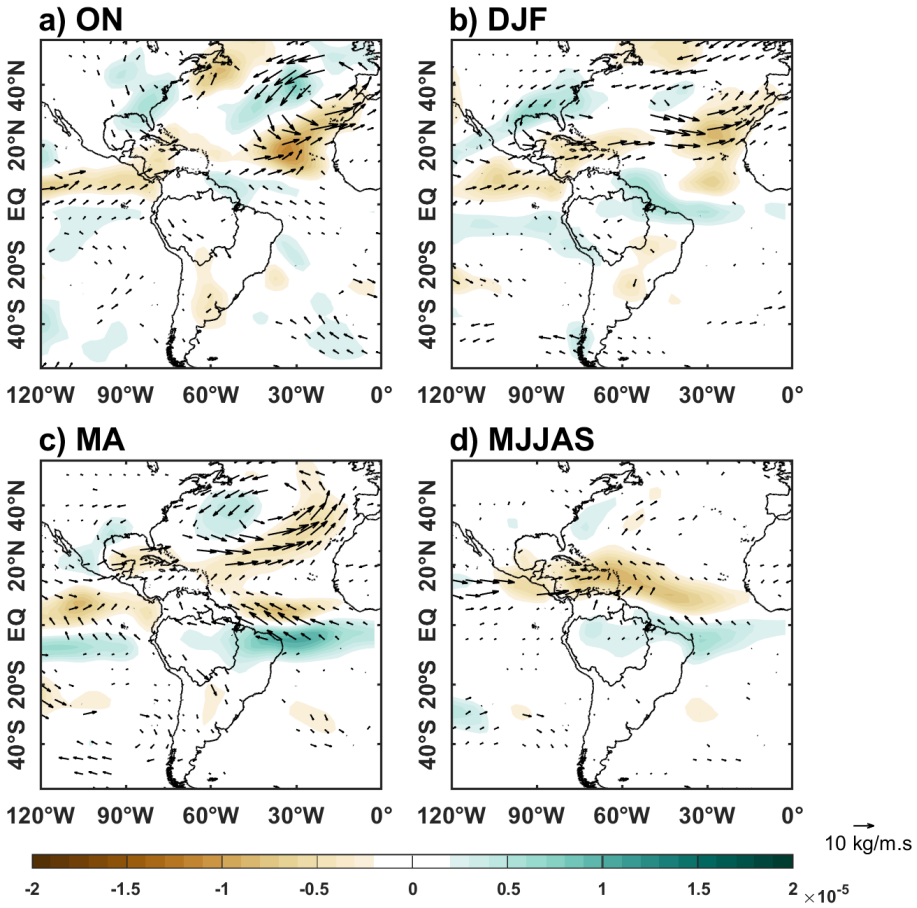

Figure 4.31: As in Fig. 4.28, but for TNAi (Tropical North Atlantic).

At the end of the SAMS (Mar-Apr), warm conditions over the tropical Atlantic, indeed, create a strong region of low pressure that reduces the transport of moisture flux towards

the continental part. This is also observed over the central-east of the Amazon Basin, and in agreement with the low precipitation observed during May-April over that region (see Figure 4.23, third panel). Moisture flux over the Atlantic region moves northward, feeding the cyclonic circulation of the Northern Hemisphere, which is stronger during this period. This circulation pattern is in agreement with the vertical structure of specific humidity and winds (Figure 4.34a, third panel). Strong convection in ∼30° N is observed with a subsidence branch between the Equator and 15° S.

The same condition over the Tropical Atlantic is also observed during the May-Sep season (period of significant TNA impact), but less intense. In addition, divergent flux (source region) covers a broad region of the Amazon Basin, also observed in the vertical structure. The circulation pattern shows strong upward motion around the TNA region (∼20-30° N), and downward motion over tropical South America (20° S-EQ), inhibiting convection there. These circulation anomalies have been considered as an intensification of the continental Hadley Cell (Yoon and Zeng, 2010).

TSAi

Considering the regression analysis using the TSAi (Figure 4.32), it is observed three important flux patterns. The first, over the Tropical North Atlantic toward Amazon Basin, with moisture flux entering from the north and northeast of the basin. The second, over southeastern Brazil, with a source region in Tropical South Atlantic and flux toward the continent (SACZ region). This flux, and the flux from the Amazon Basin (coming from the Tropical Atlantic), feed the third flux circulation, located over southeastern South America, with an intense moisture flux towards southeast, showing the presence of the SALLJ. This configuration is also observed in the vertical structure (Figure 4.34b) between 45° W-55° W, with ascending winds and high specific humidity over the Equator and the 30° S. This results suggest an agreement with Barros et al. (2000), which found that an increment (diminish) in precipitation over southeastern continent (northeastern Argentina, Uruguay and southern Brazil) is associated to weak (strong) performance of the SACZ.

During the peak of SAMS (Dec-Feb), most of the humidity convergence is restricted over southeastern South America and Northeast of Brazil, which coincides with areas with significant correlation between the TSA and rainfall values (Figure 4.24). Over the Amazon Basin, the moisture source cover a broad region of the northern and central basin, with

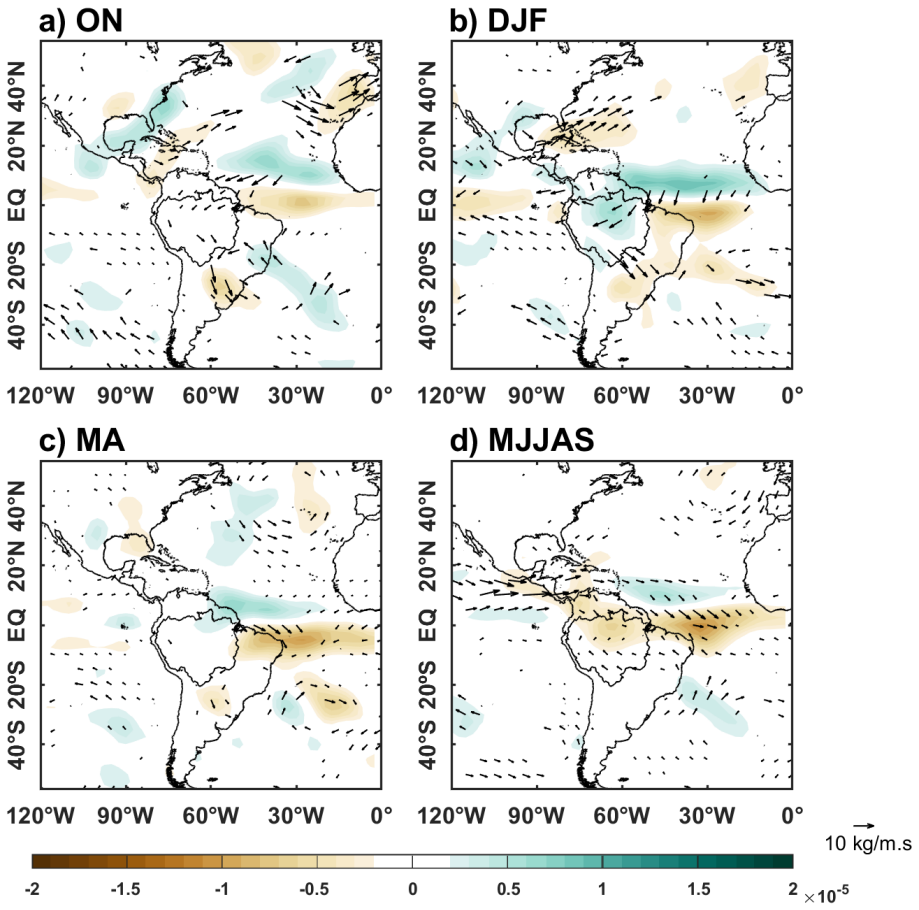

Figure 4.32: As in Fig. 4.28, but for TSAi (Tropical South Atlantic).

strong moisture flux from the northeast and towards southeast. This circulation pattern is reversed during Mar-April and greatly intensified during the absence of SAMS (May-Sep), when northern South America shows a moisture convergence. This feature, indeed, reduces the rate of moisture flux towards the southeast of South America, leading to a reduction in precipitation (Figure 4.24, fourth panel) and strong divergence within there. This pattern can be further analyzed with the vertical structure in Figure 4.34b, showing a convective region over 20-30° S and subsidence over the Equator during the peak and late SAMS. This is reverted in May-September, with a strong convective area over the equatorial region with descending branches over both 20°S (upper-level) and 20°N.

STSAi

Concerning the STSA region (Figure 4.33), during the onset of the SAMS (Oct-Nov), it is observed a not defined pattern. The vertical structure suggestes a convective region

between the equatorial region and 20° S, with low specific humidity over this region. This is reversed during the peak of the SAMS (Dec-Feb), where a moisture source region covers a broad area of the northern and central Amazon Basin, leading to an increase of precipitation (see Figure 4.25). This patter is also observed in the vertical structure (Figure 4.34c) with strong convective region with high humidity (q) over EQ-20° N. This pattern decreases in the May-April period, whit a moisture source in the South Atlantic region and central Amazon Basin. Likewise, the moisture flux is towards northeast (northeastern South America and Tropical North Atlantic) and southeast South America, leading precipitation, which is observed in the vertical structure (Figure 4.34c, third panel) as a convective region over 30° S-40° S. Finally, in the absence of the SAMS, it is not observed a defined moisture flux pattern. However, Amazon Basin shows a broad area of moisture source over the central and north of the basin, leading to a reduction in precipitation (see Figure 4.25).

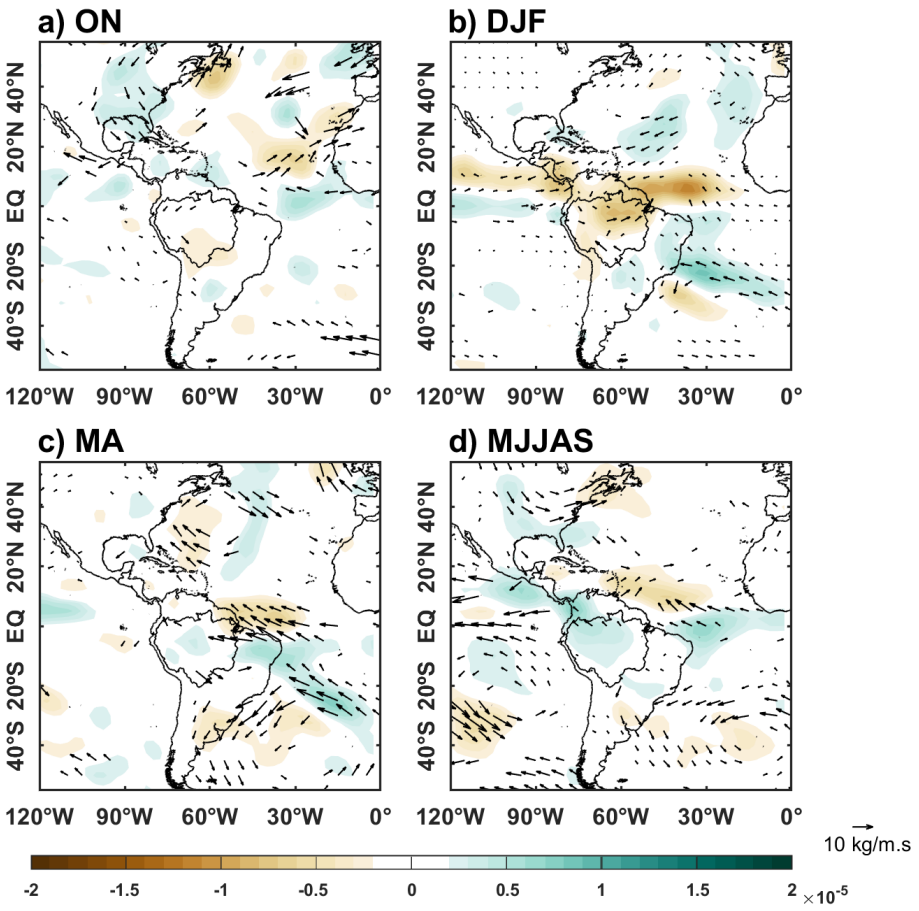

Figure 4.33: As in Fig. 4.28, but for STSAi (Subtropical South Atlantic).

As seen in previous analysis considering the climate indices correlation with precipitation fields, the regression between vertically integrated moisture flux and its convergence against the SST-based indices also corroborates the greater influence of the Pacific during Dec-Feb (SAMS peak) and the Tropical Atlantic during Mar-Apr (SAMS demise) and May-Sep (SAMS absence) over South America and, specially, over the Amazon Basin.

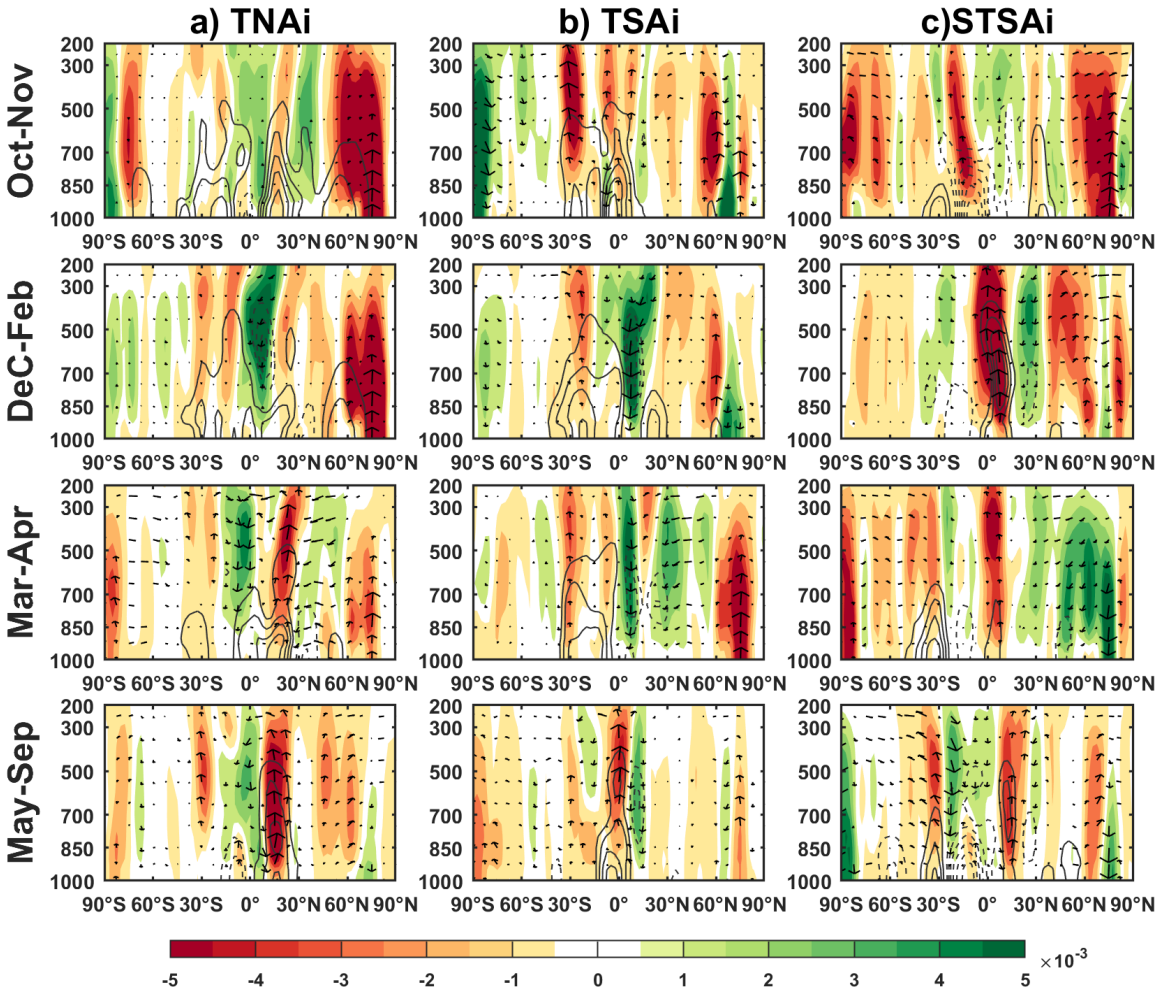

Figure 4.34: Regressed vertical sections of the meridional-vertical wind (v,w; vectors), vertical velocity (shaded), and specific humidity (contours) associated with the Pacific condition over South America. Averaged zonal from 5 °S - EQ vertical section. Contour interval is $1x10^{-2}$ $g\ kg^{-1}$ for specific humidity with solid (dashed) lines indicate positive (negative) values. The wind reference vector is 10 $m\ s^{-1}$. Wind fields are plotted only where either the v or w component is significant at the 95% level or greater as estimated by t-Test.

Chapter 5

Conclusions

This research provides an analysis of the interannual influence of the Atlantic Sea Surface Temperature (SST) on precipitation over South America, with an especial focus on Amazon Basin. In this study, gauge-based gridded rainfall (HOP-HyBAm), satellite derived precipitation (TRMM), and combined satellite and rain gauge (GPCC) data covering the 1998 to 2017 period are used to identify regions with different precipitation regimes over South America and to compare the three databases. In addition, gridded SST sata (HadiSST) for the 1870-2017 period is used to perform the Atlantic indices (TNAi, TSAi, STSAi) through Empirical Orthogonal Functions (EOF) for each Atlantic region. The interannual rainfall variability and the associated atmospheric dynamical characteristics are assessed under anomalous SST conditions of the adjacent tropical Pacific and Atlantic ocean. Climatic SST indices for Pacific and for Atlantic, GPCC and ECMWF Reanalysis (ERA-20C) datasets, for the 1940-2010 period, are used for this purpose.

5.1 Brief Summary and Main Conclusions

This study starts with a brief description of the precipitation climatology of South America, followed by the determination of its homogeneous sub-regions. Cluster analysis revealed that twelve regions are characterized by different annual precipitation regimes, which are driven by different atmospheric precipitation systems. The regions located in the extreme north of South America (Region 1 and Region 2, in Figure 4.6) show maximum rainfall between late austral fall and during winter. Equatorial regions (Regions 3 and 9, in the same Figure) present a regime with maximum rainfall during the austral autumn. The

central and southern region of Chile (Region 8) also shows the maximum precipitation during the austral winter. The other regions (e.g., Region 5 and 6) are characterized by having a monsoon regime, with maximum precipitation during the austral summer, although with different rainfall rates (shown in Figure 4.6).

In the sequence of the research, we determined the Atlantic indices to assess the interannual variability. The variance explained by the EOFs for Tropical North Atlantic (TNA), Tropical South Atlantic (TSA), and Subtropical South Atlantic (STSA) show that the first mode (PC1) is the dominant mode for the interannual variability showing a strong percentage (58.6 %, 57.17 %, and 21.41 %, respectively). In addition, the PC1 time series for each Atlantic region show that the PC1 peaks are related with extreme precipitation in the Amazon Basin (i.e.,drought and floods), according to recorded events mentioned in Espinoza et al. (2019) (see their Table 1). The TNA variability peaks in 3-5 and 10-11 years, corresponding to the interannual and decennial solar cycles (see Figure 4.9b), while the TSA variability is in 1.5, 2.5, 4-5 and 11 years (see Figure 4.12b), which is consistent with previous studies (e.g., Huang et al., 2004; Antico and Torres, 2015). In the other hand, the STSA variability peaks in 1.5, 4-6, and 8 years is noticed.

Interannual variability of the different Atlantic regions allows us to analyze their interaction between them and the the adjacent Pacific Ocean. Concerning to the Atlantic interactions, the TNA and TSA show a periodic coupling every 20 years, mainly noticeable at the beginning of the time series (shown in Figure 4.18a). Short periods in 3-4 years frequency are also noticed, where TSA leads TNA, whereas in the 11-12 years frequency, TNA leads TSA. On the other hand, the TNA and STSA are coupled in the frequency of 1.5-5 years, where TNA leads STSA and STSA leads TNA in alternate periods. The TSA and STSA interaction indicated that both regions are mostly decoupling, and varying in the opposite direction in 20 years. In addition, a shift in 1979 was determined with decreasing negative correlations (see Figure 4.17. Interaction between the Atlantic and Pacific regions (shown in Figure 4.19), also, indicates that TNA is more correlated with Central Pacific, while TSA is more correlated with Eastern Pacific. The TNA and Central Pacific presents an in-phase relationship with Central Pacific in frequencies of 3-5, 10-15 years, where TNA peaks lead the Central Pacific peaks. Moreover, the TSA leads the Eastern Pacific in frequency of 10-11 years and leads the Central Pacific in frequency of 10-20 years

(see Figure 4.20. The STSA show a connection between the Central and Eastern Pacific in different frequencies (40-50 years for the Eastern Pacific, and 60-70 years for the Central Pacific).

The Atlantic and Pacific variability are analyzed to investigate how different SST conditions around the surrounding ocean modulate extreme precipitation events over South America and, specifically, in the Amazon Basin (see Figure 4.22-4.25). Strong anomalous condition in the Eastern Pacific (E index) during the Oct-Feb period causes precipitation below normal over northern South America, northeastern Amazonian, and the Northeast of Brazil. In contrast, it also causes precipitation above normal over South Brazil, Uruguay and the La Plata Basin, and the coastal north of Peru and Ecuador. Meanwhile, positive values of the Central Pacific SST anomalies (C index) influences rainfall over northern South America and Northeast of Brazil with below-normal precipitation values. Regions along the SALLJ trajectory, the Southeast Brazil, Uruguay and the La Plata Basin, is influenced by above-normal precipitation values. All of these results are in agreement with recent papers using the same index (e.g., Cai et al., 2020, and references therein). Besides, anomalous conditions over the Tropical North and South Atlantic Ocean (TNA and TSA index) impact precipitation mainly during the late of the SAMS season (March-April) and during the May to September period, causing precipitation below normal over a broad region in South America, covering the central and eastern South America. Meanwhile, the Subtropical South Atlantic (STSA) show influence in the peak of the SAMS and during the SAMS absence, with positive (negative) correlations in the central and northern (northern) of South America during Dec-Feb (May-Sep).

We also found a strong influence of the interannual SST variability by other time-scales, like as decadal and interdecadal variability. For instance, high Pacific Decadal Oscillation (PDO) values intensify low (high) precipitation during the ENSO and TSA periods in northern (southeastern) South America during the onset and peak of the SAMS. These results are consistent with other previous works (e.g., Kayano and Andreoli, 2007; and Marengo, 2004). On the other hand, the Atlantic Multidecadal Oscillation (AMO) also influences during the peak and the end of the SAMS, also modifying the interannual variability mainly over the Central Pacific and the TNA region.

Finally, dynamical features of how different SST conditions in adjacent tropical oceans

impact South America, and Amazon Basin. We determined its influence through regression analysis between different SST indices against the vertically integrated moisture flux and its divergence. As widely documented in many previous works, the ENSO phenomena impact South America during the austral summer, creating conditions for a deficit of precipitation in Amazon Basin in response to the presence of the strong large-scale subsidence over the continent (see Figure 4.30). In addition, our results also suggest different impacts of both types of ENSO conditions (Central and Eastern Pacific El Niño) around the entire year in agreement with recent works (e.g., Timmermann et al., 2018; Freund et al., 2019). Additionally, warm conditions in the tropical north Atlantic in recent decades also played a key role in modulating extreme hydrological events (Marengo and Espinoza, 2016, and references therein). Our results show that the tropical Atlantic also acts as a source of moisture reducing. For instance, it is responsible for moisture advection toward Northwest of Amazon Basin during the SAMS onset (October-November) and the SAMS peak (December-February) (see Figure 4.31). In contrast, when warm conditions are observed during March-April and May-September, the rate of moisture flux considerably reduces (Figures 4.31 and 4.34), affecting precipitation in a broad region of Amazon Basin, as occurred in the last extreme event of 2010.

5.2 Perspectives and future works

The SST interannual variability and its influence in the Amazon Basin precipitation and other regions of South America are extremely complex, as documented in this research and previous works. This work contributes an brick in the understanding how such nonlinearities between different time-scales occur through analyses made with observational data.

Future work may include coupled ocean-atmosphere numerical climate models to test hypotheses about cause and effect relationships, highlighting the role of SST variability in key ocean basins, such as those addressed in this research. For instance, climate models can help to analyze different interactions between Atlantic regions, and between Pacific and Atlantic regions, to better answer why the coupling or decoupling between these regions is oscillating in time or why they occur in specific periods. Can such coupled ocean-

atmosphere models reproduce the interannual variability of SST in ocean basins adjoining South America and its influence on South America precipitation patterns, as observed in the present work?

Bibliography

Aceituno P., Relation entre la posicion del anticiclon subtropical y la precipitación en Chile, Relatório do Projeto no E.551.791 do Departamento de Geofísica da Universidade do Chile, 1980, p. 14

Aceituno P., On the functioning of the Southern Oscillation in the South American sector. Part I: surface climate, Mon. Weather Rev., 1988

Acevedo M. F., Mcgregor K., Andressen R., Ramirez H., Ablan M., Relations of climate variability in Venezuela to tropical Pacific SST anomalies. In 10th Symp. Glob. Chang. Stud. Am. Meteorol. Soc. , San Antonio Texas, USA, 1999, p. 1.31

Aliaga V. S., Ferrelli F., Piccolo M. C., Regionalization of climate over the Argentine Pampas, Int. J. Climatol, 2017, vol. 37, p. 1237

Alves L. M., , 2009 in , Tempo e clima no Brasil. Cavalcanti, I. F. A.; Ferreira, N. J.; Silva, M. G. A. J.; Dias, M. A. F. S. Chapt. Clima da região centro-oeste do Brasil

Andreoli R. V., Kayano M. T., ENSO-related rainfall anomalies in South America and associated circulation features during warm and cold Pacific decadal oscillation regimes, Int. J. Climatol., 2005, vol. 25, p. 2017

Antico A., Torres M. E., Evidence of a decadal solar signal in the Amazon River: 1903 to 2013, Geophys. Res. Lett., 2015, vol. 42, p. 10782

Arraut J. M., Satyamurty P., Precipitation and water vapor transport in the Southern Hemisphere with emphasis on the South American region, J. Appl. Meteorol. Climatol., 2009, vol. 48, p. 1902

Ashok K., Behera S. K., Rao S. A., Weng H., Yamagata T., El Niño Modoki and its possible teleconnection, J. Geophys. Res. Ocean., 2007, vol. 112, p. 1

Barichivich J., Gloor E., Peylin P., Brienen R. J., Schöngart J., Espinoza J. C., Pattnayak K. C., Recent intensification of Amazon flooding extremes driven by strengthened Walker circulation, Sci. Adv., 2018, vol. 4, p. 1

Barros V., Gonzalez M., Liebmann B., Camilloni I., Influence of the South Atlantic convergence zone and South Atlantic Sea surface temperature on interannual summer rainfall variability in Southeastern South America, Theor. Appl. Climatol., 2000, vol. 67, p. 123

Becker A., Finger P., Meyer-Christoffer A., Rudolf B., Schamm K., Schneider U., Ziese M., A description of the global land-surface precipitation data products of the Global Precipitation Climatology Centre with sample applications including centennial (trend) analysis from 1901-present, Earth Syst. Sci. Data, 2013, vol. 5, p. 71

Berbery E. H., Barros V. R., The hydrologic cycle of the La Plata basin in South America, J. Hydrometeorol., 2002, vol. 3, p. 630

Boers N., Rheinwalt A., Bookhagen B., Barbosa H. M., Marwan N., Marengo J., Kurths J., The South American rainfall dipole: A complex network analysis of extreme events, Geophys. Res. Lett., 2014, vol. 41, p. 7397

Bombardi R. J., Carvalho L. M., The South Atlantic dipole and variations in the characteristics of the South American Monsoon in the WCRP-CMIP3 multi-model simulations, Clim. Dyn., 2011, vol. 36

Bombardi R. J., Carvalho L. M., Jones C., Reboita M. S., Precipitation over eastern South America and the South Atlantic Sea surface temperature during neutral ENSO periods, Clim. Dyn., 2014, vol. 42, p. 1553

Bourlès B., Araujo M., McPhaden M. J., Brandt P., PIRATA: A Sustained Observing System for Tropical Atlantic Climate Research and Forecasting, Earth Sp. Sci., 2019, vol. 6, p. 577

Braun S. A., Stocker E., Marius J., , 2011 Tropical Rainfall Measuring Mission

Brierley C., Wainer I., Inter-annual variability in the tropical Atlantic from the Last Glacial Maximum into future climate projections simulated by CMIP5/PMIP3, Clim. Past, 2018, vol. 14, p. 1377

Cai W., McPhaden M. J., Grimm A. M., Rodrigues R. R., Taschetto A. S., Garreaud R. D., Dewitte B., Poveda G., Ham Y.-G., Santoso A., Ng B., Anderson W., Wang G., Geng T., Jo H.-S., Marengo J. A., Alves L. M., Osman M., Li S., Wu L., Karamperidou C., Takahashi K., Vera C., Climate impacts of the El Niño-Southern Oscillation on South America, Nat. Rev. Earth Environ., 2020, vol. 1, p. 215

Capotondi A., Wittenberg A. T., Newman M., Di Lorenzo E., Yu J. Y., Braconnot P., Cole J., Dewitte B., Giese B., Guilyardi E., Jin F. F., Karnauskas K., Kirtman B., Lee T., Schneider N., Xue Y., Yeh S. W., Understanding ENSO diversity, Bull. Am. Meteorol. Soc., 2015, vol. 96, p. 921

Carvalho L. M.; Jones C., , 2009a in , Tempo e clima no Brasil. Cavalcanti, I. F. A.; Ferreira, N. J.; Silva, M. G. A. J.; Dias, M. A. F. S. Chapt. Zona de convergência do Atlântico Sul

Carvalho L. M.; Jones C., , 2009b in , Tempo e clima no Brasil. Cavalcanti, I. F. A.; Ferreira, N. J.; Silva, M. G. A. J.; Dias, M. A. F. S. Chapt. Clima da região nordeste do Brasil

Carvalho L. M., Jones C., Liebmann B., Extreme precipitation events in southeastern South America and large-scale convective patterns in the South Atlantic covergence zone, J. Clim., 2002

Carvalho L. M., Jones C., Silva A. E., Liebmann B., Silva Dias P. L., The South American Monsoon System and the 1970s climate transition, Int. J. Climatol., 2011, vol. 31, p. 1248

Carvalho L. M. V., Jones C., Liebmann B., The South Atlantic Convergence Zone: Intensity, Form, Persistence, and Relationships with Intraseasonal to Interannual Activity and Extreme Rainfall, Journal of Climate, 2004, vol. 17, p. 88

Castellanos P., Campos E. J., Piera J., Sato O. T., Silva Dias M. A., Impacts of Agulhas

leakage on the tropical Atlantic western boundary systems, J. Clim., 2017, vol. 30, p. 6645

Chang P., Yamagata T., Schopf P., Behera S. K., Carton J., Kessler W. S., Meyers G., Qu T., Schott F., Shetye S., Xie S. P., Climate fluctuations of tropical coupled systems - The role of ocean dynamics, J. Clim., 2006, vol. 19, p. 5122

Chelton D., Risien C., Zonal and Meridional Discontinuities and Other Issues with the HadISST1.1 Dataset, NASA Report, 2016, vol. 1

Chiessi C. M., Mulitza S., Pätzold J., Wefer G., Marengo J. A., Possible impact of the Atlantic Multidecadal Oscillation on the South American summer monsoon, Geophys. Res. Lett., 2009, vol. 36, p. 1

Coelho C. A., de Oliveira C. P., Ambrizzi T., Reboita M. S., Carpenedo C. B., Campos J. L. P. S., Tomaziello A. C. N., Pampuch L. A., Custódio M. d. S., Dutra L. M. M., Da Rocha R. P., Rehbein A., The 2014 southeast Brazil austral summer drought: regional scale mechanisms and teleconnections, Clim. Dyn., 2016, vol. 46, p. 3737

Cohen J. C. P., Dias M. A. S., Nobre C. A., Aspectos climatológicos das linhas de instabilidade na Amazônia., Climanálise, 1989

Costa A. A., De Oliveira C. J., De Oliveira J. C. P., Sampaio A. J. D. C., Microphysical observations of warm cumulus clouds in Ceara, Brazil, Atmos. Res., 2000, vol. 54, p. 167

da Silva L. J., Reboita M. S., da Rocha R. P., Relação da passagem de frentes frias na região sul de Minas Gerais (RSMG) com a precipitação e eventos de geada, Rev. Bras. Climatol., 2014, vol. 14, p. 229

de Ruijter W. P. M., Biastoch A., Drijfhout S. S., Lutjeharms J. R. E., Matano R. P., Pichevin T., van Leeuwen P. J., Weijer W., Indian-Atlantic interocean exchange: Dynamics, estimation and impact, J. Geophys. Res. Ocean., 1999, vol. 104, p. 20885

Deser C., Alexander M. A., Xie S.-P., Phillips A. S., Sea Surface Temperature Variability: Patterns and Mechanisms. vol. 2, 2010, 115

Deser C., Phillips A. S., Alexander M. A., Twentieth century tropical sea surface temperature trends revisited, Geophys. Res. Lett., 2010, vol. 37, p. 1

Deser C., Phillips A. S., Hurrell J. W., Pacific interdecadal climate variability: Linkages between the tropics and the North Pacific during boreal winter since 1900, J. Clim., 2004

Dommenget D., Latif M., Interannual to decadal variability in the tropical Atlantic, J. Clim., 2000

dos Santos S. R. Q., Braga C. C., Sansigolo C. A., de Araujo Tiburtino Neves T. T., dos Santos A. P. P., Droughts in the Amazon: Identification, Characterization and Dynamical Mechanisms Associated, Am. J. Clim. Chang., 2017, vol. 06, p. 425

Drumond A., Nieto R., Gimeno L., Ambrizzi T., A Lagrangian identification of major sources of moisture over Central Brazil and la Plata Basin, J. Geophys. Res. Atmos., 2008

Enfield D. B., Mestas-Nuñez A. M., Trimble P. J., The Atlantic multidecadal oscillation and its relation to rainfall and river flows in the continental U.S, Geophys. Res. Lett., 2001, vol. 28, p. 2077

Espinoza J. C., Marengo J. A., Ronchail J., Carpio J. M., Flores L. N., Guyot J. L., The extreme 2014 flood in south-western Amazon basin: The role of tropical-subtropical South Atlantic SST gradient, Environ. Res. Lett., 2014, vol. 9, p. 124007

Espinoza J. C., Ronchail J., Frappart F., Lavado W., Santini W., Guyot J. L., The Major Floods in the Amazonas River and Tributaries (Western Amazon Basin) during the 1970-2012 Period: A Focus on the 2012 Flood, J. Hydrometeorol., 2013, vol. 14, p. 1000

Espinoza J. C., Ronchail J., Guyot J. L., Cochonneau G., Naziano F., Lavado W., Oliveira E. D., Pombosag R., Vauchelh P., Spatio-temporal rainfall variability in the Amazon basin countries (Brazil, Peru, Bolivia, Colombia, and Ecuador), Int. J. Climatol., 2009, vol. 29, p. 1574

Espinoza J. C., Ronchail J., Guyot J. L., Junquas C., Vauchel P., Lavado W., Drapeau G., Pombosa R., Climate variability and extreme drought in the upper Solimões River (western Amazon Basin): Understanding the exceptional 2010 drought, Geophys. Res. Lett., 2011, vol. 38

Espinoza J. C., Ronchail J., Marengo J. A., Segura H., Contrasting North–South changes in Amazon wet-day and dry-day frequency and related atmospheric features (1981–2017), Clim. Dyn., 2019, vol. 52, p. 5413

Figueroa S. N., Nobre C. A., Precipitation dristribution over central and western tropical South America, Climanalise, 1990, vol. 5, p. 36

Fisch G. F., Marengo J. A., Nobre C. A., Uma revisão geral sobre o clima da Amazônia, Acta Amaz., 1998, vol. 28, p. 101

Freund M., Australian rainfall and El Nino diversity: past variability and context for recent changes, University of Melbourne, 2018, Ph.D. Thesis

Freund M. B., Henley B. J., Karoly D. J., McGregor H. V., Abram N. J., Dommenget D., Higher frequency of Central Pacific El Niño events in recent decades relative to past centuries, Nat. Geosci., 2019, vol. 12, p. 450

Fu R., Yin L., Li W., Arias P. A., Dickinson R. E., Huang L., Chakraborty S., Fernandes K., Liebmann B., Fisher R., Myneni R. B., Increased dry-season length over southern Amazonia in recent decades and its implication for future climate projection, Proc. Natl. Acad. Sci. U. S. A., 2013, vol. 110, p. 18110

Gan M., Rodrigues L. R., Rao V. B., , 2009 in , Tempo e clima no Brasil. Cavalcanti, I. F. A.; Ferreira, N. J.; Silva, M. G. A. J.; Dias, M. A. F. S. Chapt. Monção na América do Sul

Garreaud R., Vuille M., Clement A. C., The climate of the Altiplano: Observed current conditions and mechanisms of past changes, Palaeogeogr. Palaeoclimatol. Palaeoecol., 2003, vol. 194, p. 5

Garreaud R. D., A plausible atmospheric trigger for the 2017 coastal El Niño, Int. J. Climatol., 2018, vol. 38, p. e1296

Garreaud R. D., Aceituno P., Interannual rainfall variability over the South American Altiplano, J. Clim., 2001

Garreaud R. D., Aceituno P., , 2007 in Veblen T. T., Young K. R., Orme A. R., eds, , The Physical Geography of South America. Oxford University Press Chapt. 3 pp 45–59

Garreaud R. D., Vuille M., Compagnucci R., Marengo J., Present-day South American climate, Palaeogeogr. Palaeoclimatol. Palaeoecol., 2009, vol. 281, p. 180

Garreaud R. D., Wallace J. M., Summertime incursions of midlatitude air into subtropical and tropical South America, Mon. Weather Rev., 1998, vol. 126, p. 2713

Gloor M., Brienen R. J., Galbraith D., Feldpausch T. R., Schöngart J., Guyot J. L., Espinoza J. C., Lloyd J., Phillips O. L., Intensification of the Amazon hydrological cycle over the last two decades, Geophys. Res. Lett., 2013, vol. 40, p. 1729

Goldberg R. A., Tisnado G. M., Scofield R. A., , 1987 Characteristics of extreme rainfall events in Northwestern Peru during the 1982-1983 E1 Nifio Period

Greco S., Swap R., Garstang M., Ulanski S., Shipham M., Harris R. C., Talbot R., Andreae M. O., Artaxo P., Rainfall and surface kinematic conditions over central Amazonia during ABLE 2B, J. Geophys. Res., 1990, vol. 95, p. 1

Grimm A. M., Ambrizzi T., , 2009 in , Past Clim. Var. South Am. Surround. Reg.. pp 159–191

Grimm A. M., Barros V. R., Doyle M. E., Climate variability in southern South America associated with El Nino and La Nina events, J. Clim., 2000, vol. 13, p. 35

Grimm A. M., Tedeschi R. G., ENSO and extreme rainfall events in South America, J. Clim., 2009, vol. 22, p. 1589

Grodsky S. A., Carton J. A., The intertropical convergence zone in the South Atlantic and the equatorial cold tongue, J. Clim., 2003

Hadley G., Concerning the cause of the general trade winds, Philos Trans R Soc Lond, 1735, vol. 39, p. 58

Hastenrath S., Climate dynamics of the tropics, Clim. Dyn. Trop., 1991

Hastenrath S., Heller L., Dynamics of climatic hazards in northeast Brazil, Q. J. R. Meteorol. Soc., 1977

Hastenrath S., Lamb P. J., Climatic atlas of the tropical Atlantic and eastern Pacific oceans. Madison; London: University of Wisconsin Press, 1977

Hersbach H., Peubey C., Simmons A., Berrisford P., Poli P., Dee D., ERA-20CM: A twentieth-century atmospheric model ensemble, Q. J. R. Meteorol. Soc., 2015

Hirst A. C., Hastenrath S., Atmosphere-Ocean Mechanisms of Climate Anomalies in the Angola-Tropical Atlantic Sector, 1983, vol. 13, p. 1146

Horel J. D., Cornejo-Garrido A. G., Convection along the coast of northern Peru during 1983: spatial and temporal variation of clouds and rainfall., Mon. Weather Rev., 1986

Houghton R. W., Tourre Y. M., Characteristics of low-frequency sea surface temperature fluctuations in the tropical Atlantic, 1992, vol. 5, p. 765

Hu Q., Feng S., Oglesby R. J., Variations in North American summer precipitation driven by the Atlantic multidecadal oscillation, J. Clim., 2011, vol. 24, p. 5555

Huang B., Schopf P. S., Shukla J., Intrinsic Ocean–Atmosphere Variability of the Tropical Atlantic Ocean, J. Clim., 2004, vol. 147, p. 2058

Huffman G. J., , 2018 The Transition in Multi-Satellite Products from TRMM to GPM (TMPA to IMERG)

Huffman G. J., Adler R. F., Bolvin D. T., Gu G., Nelkin E. J., Bowman K. P., Hong Y., Stocker E. F., Wolff D. B., The TRMM Multisatellite Precipitation Analysis (TMPA): Quasi-global, multiyear, combined-sensor precipitation estimates at fine scales, J. Hydrometeorol., 2007, vol. 8, p. 38

Huffman G. J., Adler R. F., Bolvin D. T., Nelkin E. J., , 2010 in , Satell. Rainfall Appl. Surf. Hydrol.

Hurrel J. W., Kushnir Y., Ottersen G., Visbeck M., , 2003 in Hurrell J. W., Kushnir Y., Ottersen G., Visbeck M., eds, , North Atl. Oscil. Clim. Significance Environ. Impact. Geophysical monograph Washington, DC Chapt. 1 pp 1–35

Kaplan A., Cane M. A., Kushnir Y., Clement A. C., Blumenthal M. B., Rajagopalan B., Analyses of global sea surface temperature 1856-1991, J. Geophys. Res. Ocean., 1998, vol. 103, p. 18567

Kayano M. T., Andreoli R. V., Relationships between rainfall anomalies over northeastern Brazil and the El Niño-Southern Oscillation, J. Geophys. Res. Atmos., 2006, vol. 111, p. 1

Kayano M. T., Andreoli R. V., Relations of South American summer rainfall interannual variations with the Pacific Decadal Oscillation, Int. J. Climatol., 2007, vol. 27, p. 531

Kayano M. T., Andreoli R. V., de Souza R. A. F., El Niño–Southern Oscillation related teleconnections over South America under distinct Atlantic Multidecadal Oscillation and Pacific Interdecadal Oscillation backgrounds: La Niña, Int. J. Climatol., 2019, vol. 39, p. 1359

Kayano M. T., Capistrano V. B., How the Atlantic multidecadal oscillation (AMO) modifies the ENSO influence on the South American rainfall, Int. J. Climatol., 2014, vol. 34, p. 162

Kerr R. A., A North Atlantic climate pacemaker for the centuries, Science (80-.)., 2000, vol. 288, p. 1984

Killick R., Fearnhead P., Eckley I. A., Optimal detection of changepoints with a linear computational cost, J. Am. Stat. Assoc., 2012

Knight J. R., Folland C. K., Scaife A. A., Climate impacts of the Atlantic multidecadal oscillation, Geophys. Res. Lett., 2006

Kousky V. E., Gan M. A., Upper tropospheric cyclonic vortices in the tropical South Atlantic., Tellus, 1981, vol. 33, p. 538

Kousky V. E., Kagano M. T., Cavalcanti I. F., A review of the Southern Oscillation: oceanic[U+2010]atmospheric circulation changes and related rainfall anomalies, Tellus A, 1984

Lagos P., Silva Y., Nickl E., Mosquera K., El Ninño - Related precipitation variability in Perú, Adv. Geosci., 2008

Laraque A., Ronchail J., Cochonneau G., Pombosa R., Guyot J. L., Heterogeneous distribution of rainfall and discharge regimes in the Ecuadorian Amazon basin, J. Hydrometeorol., 2007, vol. 8, p. 1364

Lau K. M., Hengyi Weng Climate signal detection using wavelet transform: how to make a time series sing, Bull. - Am. Meteorol. Soc., 1995

Lavado-Casimiro W., Espinoza J. C., Impactos de el niño y la niña en las lluvias del Perú (1965-2007), Rev. Bras. Meteorol., 2014, vol. 29, p. 171

Levine A. F., Frierson D. M., McPhaden M. J., AMO forcing of multidecadal pacific ITCZ variability, J. Clim., 2018, vol. 31, p. 5749

Levine A. F., McPhaden M. J., Frierson D. M., The impact of the AMO on multidecadal ENSO variability, Geophys. Res. Lett., 2017, vol. 44, p. 3877

Liu C., Zipser E. J., "Warm rain"in the tropics: Seasonal and regional distributions based on 9 yr of TRMM data, J. Clim., 2009, vol. 22, p. 767

Livezey R. E., Chen W. Y., Statistical field significance and its determination by Monte Carlo techniques., Mon. Weather Rev., 1983

Lübbecke J. F., Rodríguez-Fonseca B., Richter I., Martín-Rey M., Losada T., Polo I., Keenlyside N. S., Equatorial Atlantic variability—Modes, mechanisms, and global teleconnections, Wiley Interdiscip. Rev. Clim. Chang., 2018, vol. 9, p. 1

Machado L. A., Silva Dias M. A., Morales C., Fisch G., Colaborators. The CHUVA project: How does convection vary across Brazil?, Bull. Am. Meteorol. Soc., 2014, vol. 95, p. 1365

Machado L. A. T., Ferreira N. J., Laurent H.; Diedhiou A., , 2009 in , Tempo e clima no Brasil. Cavalcanti, I. F. A.; Ferreira, N. J.; Silva, M. G. A. J.; Dias, M. A. F. S. Chapt. Distúrbios ondulatórios de leste

Mantua N. J., Hare S. R., The Pacific Decadal Oscillation, J. Oceanogr., 2002

Mantua N. J., Hare S. R., Zhang Y., Wallace J. M., Francis R. C., A Pacific Interdecadal Climate Oscillation with Impacts on Salmon Production, Bull. Am. Meteorol. Soc., 1997, vol. 78, p. 1069

Marengo J., Cornejo A., Satyamurty P., Nobre C., Sea W., Cold surges in tropical and extratropical south America: The strong event in June 1994, Mon. Weather Rev., 1997, vol. 125, p. 2759

Marengo J. A., Interdecadal variability and trends of rainfall across the Amazon basin, Theor. Appl. Climatol., 2004, vol. 78, p. 79

Marengo J. A., Alves L. M., Alvala R. C., Cunha A. P., Brito S., Moraes O. L., Climatic characteristics of the 2010-2016 drought in the semiarid northeast Brazil region, An. Acad. Bras. Cienc., 2018

Marengo J. A., Alves L. M., Soares W. R., Rodriguez D. A., Camargo H., Riveros M. P., Pabló A. D., Two contrasting severe seasonal extremes in tropical South America in 2012: Flood in Amazonia and drought in Northeast Brazil, J. Clim., 2013

Marengo J. A., Espinoza J. C., Extreme seasonal droughts and floods in Amazonia: Causes, trends and impacts, Int. J. Climatol., 2016, vol. 36, p. 1033

Marengo J. A., Hastenrath S., Case Studies of Extreme Climatic Events in the Amazon Basin, J. Clim., 1993, vol. 6, p. 617

Marengo J. A., Liebmann B., Kousky V. E., Filizola N. P., Wainer I. C., Onset and end of the rainy season in the Brazilian Amazon Basin, J. Clim., 2001, vol. 14, p. 833

Marengo J. A., Nobre C. A., , 2009 in , Tempo e clima no Brasil. Cavalcanti, I. F. A.; Ferreira, N. J.; Silva, M. G. A. J.; Dias, M. A. F. S. Chapt. Clima da Região Amazônica

Marengo J. A., Nobre C. A., Tomasella J., Oyama M. D., de Oliveira G. S., de Oliveira R., Camargo H., Alves L. M., Brown I. F., The drought of Amazonia in 2005, J. Clim., 2008, vol. 21, p. 495

Marengo J. A., Tomasella J., Alves L. M., Soares W. R., Rodriguez D. A., The drought of 2010 in the context of historical droughts in the Amazon region, Geophys. Res. Lett., 2011, vol. 38

Martín-Rey M., Polo I., Rodríguez-Fonseca B., Losada T., Lazar A., Is there evidence of changes in tropical Atlantic variability modes under AMO phases in the observational record?, J. Clim., 2018, vol. 31, p. 515

Masiokas M. H., Cara L., Villalba R., Pitte P., Luckman B. H., Toum E., Christie D. A., Le Quesne C., Mauget S., Streamflow variations across the Andes (18°–55°S) during the instrumental era, Sci. Rep., 2019, vol. 9, p. 1

Masiokas M. H., Villalba R., Luckman B. H., Le Quesne C., Aravena J. C., Snowpack variations in the central Andes of Argentina and Chile, 1951-2005: Large-scale atmospheric influences and implications for water resources in the region, J. Clim., 2006

Mayta V. C., Silva N. P., Ambrizzi T., Dias P. L., Espinoza J. C., Assessing the skill of all-season diverse Madden–Julian oscillation indices for the intraseasonal Amazon precipitation, Clim. Dyn., 2020

Melo A. B. C., Cavalcanti I. F. A., Souza P. P., , 2009 in , Tempo e clima no Brasil. Cavalcanti, I. F. A.; Ferreira, N. J.; Silva, M. G. A. J.; Dias, M. A. F. S. Chapt. Zona de Convergência Intertropical do Atlântico

Molinier M., Guyot J. L., De Oliveira E., Guimaraes V., Les regimes hydrologiques de l'Amazone et de ses affluents, IAHS-AISH Publ., 1996, pp 209–222

Molion L. C. B., Climatologia dinâmica da Regiao Amazônica: mecanismos de precipitaçao, Rev. Bras. Meteorol., 1987

Montecinos A., Díaz A., Aceituno P., Seasonal diagnostic and predictability of rainfall in subtropical South America based on tropical Pacific SST, J. Clim., 2000

NASA JAXA Key TRMM Facts, Earth Sci. Ref. Handb., 2001

Newman M., Alexander M. A., Ault T. R., Cobb K. M., Deser C., Di Lorenzo E., Mantua N. J., Miller A. J., Minobe S., Nakamura H., Schneider N., Vimont D. J., Phillips A. S., Scott J. D., Smith C. A., The Pacific decadal oscillation, revisited, J. Clim., 2016, vol. 29, p. 4399

Nieto-Ferreira R., Rickenbach T. M., Regionality of monsoon onset in South America: a three-stage conceptual model, International Journal of Climatology, 2011, vol. 31, p. 1309

Nnamchi H. C., Li J., Anyadike R. N. C., Does a dipole mode really exist in the South Atlantic Ocean?, Journal of Geophysical Research: Atmospheres, 2011, vol. 116

Nobre C. A., Molion L. C. B., The climatology of drought prediction, Kluwer Academic Publishers. The impact of variation on agriculture, 1988

Nobre P., Shukla J., Variation of Sea Surface Temperature, Wind Stress and Rainfall over the Tropical Atlantic and South America, J. Clim., 1996, vol. 9, p. 2464

Peng Q., Xie S. P., Wang D., Zheng X. T., Zhang H., Coupled ocean-atmosphere dynamics of the 2017 extreme coastal El Niño, Nat. Commun., 2019, vol. 10, p. 1

Poli P., Hersbach H., Berrisford P., authors O., , 2015 ERA-20C Deterministic

Poli P., Hersbach H., Dee D. P., Berrisford P., Simmons A. J., Vitart F., Laloyaux P., Tan D. G., Peubey C., Thépaut J. N., Trémolet Y., Hólm E. V., Bonavita M., Isaksen L., Fisher M., ERA-20C: An atmospheric reanalysis of the twentieth century, J. Clim., 2016

Poli P., Hersbach H., Tan D., Dee D., Thépaut J.-N., Simmons A., Peubey C., Laloyaux P., Komori T., Berrisford P., Dragani R., The data assimilation system and initial performance evaluation of the ECMWF pilot reanalysis of the 20th-century assimilating surface observations only (ERA-20C), ERA Rep. Ser., 2013

Poveda G., Jaramillo A., Gil M. M., Quiceno N., Mantilla R. I., Seasonality in ENSO-related precipitation, river discharges, soil moisture, and vegetation index in Colombia, Water Resour. Res., 2001

Poveda G., Waylen P. R., Pulwarty R. S., Annual and inter-annual variability of the present climate in northern South America and southern Mesoamerica, Palaeogeogr. Palaeoclimatol. Palaeoecol., 2006, vol. 234, p. 3

Ramirez M. C. V., Kayano M. T., Ferreira N. J., Statistical analysis of upper tropospheric vortices in the vicinity of northeast Brazil during the 1980-1989 period, Atmósfera, 1999, vol. 12, p. 75

Rao V. B., Hada K., Characteristics of rainfall over Brazil: Annual variations and connections with the Southern Oscillation, Theor. Appl. Climatol., 1990, vol. 42, p. 81

Rau P., Bourrel L., Labat D., Melo P., Dewitte B., Frappart F., Lavado W., Felipe O., Regionalization of rainfall over the Peruvian Pacific slope and coast, Int. J. Climatol., 2017, vol. 37, p. 143

Rayner N. A., Parker D. E., Horton E. B., Folland C. K., Alexander L. V., Rowell D. P., Kent E. C., Kaplan A., Global analyses of sea surface temperature, sea ice, and night

marine air temperature since the late nineteenth century, J. Geophys. Res. D Atmos., 2003

Reboita M. S., Gan M. A., Porfírio R., Rocha D. A., Ambrizzi T., Regimes de precipitação na América do Sul: Uma revisão bibliográfica, Rev. Bras. Meteorol., 2010, vol. 25, p. 185

Rickenbach T. M., Nocturnal cloud systems and the diurnal variation of clouds and rainfall in southwestern Amazonia, Mon. Weather Rev., 2004, vol. 132, p. 1201

Riehl H., Venezuelan rain systems and the general circulation of the summer tropics II: Relations between low and high latitudes, Mon. Weather Rev., 1977, vol. 105, p. 1421

Riehl H., Betts A. K., Mata M. P. D., Betts A. K., Mata M. P. D., , 1977 On the Weather of Venezuela: A Summary Report on the Venezuela Experiments of 1969 and 1972

Robertson A. W., Farrara J. D., Mechoso C. R., Simulations of the atmospheric response to South Atlantic sea surface temperature anomalies, J. Clim., 2003, vol. 16, p. 2540

Robertson A. W., Mechoso C. R., Interannual and interdecadal variability of the South Atlantic convergence zone, Mon. Weather Rev., 2000, vol. 128, p. 2947

Rodionov S. N., A sequential algorithm for testing climate regime shifts, Geophys. Res. Lett., 2004

Ronchail J., Cochonneau G., Molinier M., Guyot J. L., De Miranda Chaves A. G., Guimarães V., De Oliveira E., Interannual rainfall variability in the Amazon basin and sea-surface temperatures in the equatorial Pacific and the tropical Atlantic Oceans, Int. J. Climatol., 2002, vol. 22, p. 1663

Ropelewski C. F., Halpert M. S., , 1987 Global and Regional Scale Precipitation Patterns Associated with the El Niño/Southern Oscillation

Rousseeuw P. J., Silhouettes: A graphical aid to the interpretation and validation of cluster analysis, J. Comput. Appl. Math., 1987

Rühs S., Durgadoo J. V., Behrens E., Biastoch A., Advective timescales and pathways of Agulhas leakage, Geophys. Res. Lett., 2013, vol. 40, p. 3997

Salati E., Marques J., Molion L. C. B., Origin and distribution of rain in the Amazon Basin, Interciencia, 1978, vol. 3, p. 200

Santos E. B., Lucio P. S., Santos e Silva C. M., Precipitation regionalization of the Brazilian Amazon, Atmos. Sci. Lett., 2015, vol. 16, p. 185

Satyamurty P., Da Conceicao Ferreira C., Gan M. A., Cyclonic vortices over South America, Tellus, Ser. A, 1990, vol. 42 A, p. 194

Satyamurty P., da Costa C. P. W., Manzi A. O., Moisture source for the Amazon Basin: A study of contrasting years, Theor. Appl. Climatol., 2013, vol. 111, p. 195

Satyamurty P., Nobre C. A., Silva Dias P. L., , 1998 in Karoly D. J., Vincent D. G., eds, , Meteorol. South. Hemisph.. American Meteorological Society Boston Chapt. 3C pp 119–140

Silva C. B., Silva M. E. S., Krusche N., Ambrizzi T., de Jesus Ferreira N., da Silva Dias P. L., The analysis of global surface temperature wavelets from 1884 to 2014, Theor. Appl. Climatol., 2019, vol. 136, p. 1435

Silva Dias M. A., Sistemas de Mesoescala e previsao de tempo a curto prazo, Rev. Bras. Meteorol., 1987

Silva Dias M. A., Dias J., Carvalho L. M., Freitas E. D., Silva Dias P. L., Changes in extreme daily rainfall for São Paulo, Brazil, Clim. Change, 2013, vol. 116, p. 705

Silva Dias M. A. F., Rozante J. R., Machado L. A., , 2009 in , Tempo e clima no Brasil. Cavalcanti, I. F. A.; Ferreira, N. J.; Silva, M. G. A. J.; Dias, M. A. F. S. Chapt. Complexos Convectivos de Mesoescala

Silva Dias P. L., Schubert W. H., Demaria M., Large-scale response of the tropical atmosphere to transient convection., J. Atmos. Sci., 1983

Sterl A., Hazeleger W., Coupled variability and air-sea interaction in the South Atlantic Ocean, Clim. Dyn., 2003, vol. 21, p. 559

Sulca J., Takahashi K., Espinoza J. C., Vuille M., Lavado-Casimiro W., Impacts of different ENSO flavors and tropical Pacific convection variability (ITCZ, SPCZ) on austral summer rainfall in South America, with a focus on Peru, Int. J. Climatol., 2018

Sun C., Kucharski F., Li J., Jin F. F., Kang I. S., Ding R., Western tropical Pacific multidecadal variability forced by the Atlantic multidecadal oscillation, Nat. Commun., 2017, vol. 8, p. 1

Sun C., Li J., Li X., Xue J., Ding R., Xie F., Li Y., Oceanic forcing of the interhemispheric SST dipole associated with the Atlantic Multidecadal Oscillation, Environ. Res. Lett., 2018, vol. 13

Sun Q., Miao C., Duan Q., Ashouri H., Sorooshian S., Hsu K. L., A Review of Global Precipitation Data Sets: Data Sources, Estimation, and Intercomparisons, Rev. Geophys., 2018, vol. 56, p. 79

Takahashi K., Montecinos A., Goubanova K., Dewitte B., ENSO regimes: Reinterpreting the canonical and Modoki El Nio, Geophys. Res. Lett., 2011, vol. 38, p. 1

Taljaard J. J., , 1972 in van Loon H., Taljaard J. J., Sasamori T., London J., Hoyt D. V., Labitzke K., Newton C. W., eds, , Meteorol. South. Hemisph.. American Meteorological Society Boston Chapt. 1 pp 1–8

Timmermann A., An S. I., Kug J. S., Jin F. F., El Niño-Southern Oscillation complexity, Nature, 2018, vol. 559, p. 535

Tokinaga H., Xie S. P., Weakening of the equatorial Atlantic cold tongue over the past six decades, Nat. Geosci., 2011

Torrence C., Compo G. P., A Practical Guide to Wavelet Analysis, Bull. Am. Meteorol. Soc., 1998

Trenberth K. E., Shea D. J., Atlantic hurricanes and natural variability in 2005, Geophys. Res. Lett., 2006, vol. 33

Uvo C., A Zona de Convergência Intertropical (ZCIT) e a Precipitação da região Norte do Nordeste do Brasil, INPE, 1989, Master Dissertation

Uvo C., Berndtsson R., Regionalization and spatial properties of Ceará State rainfall in northeast Brazil, J. Geophys. Res., 1996, vol. 101, p. 4221

Uvo C. B., Repelli C. A., Zebiak S. E., Kushnir Y., The relationships between tropical Pacific and Atlantic SST and northeast Brazil monthly precipitation, J. Clim., 1998, vol. 11, p. 551

Velasco I., Fritsch J. M., Mesoscale convective complexes in the Americas, J. Geophys. Res., 1987

Venegas S. A., Mysak L. A., Straub D. N., Atmosphere-ocean coupled variability in the South Atlantic, J. Clim., 1997, vol. 10, p. 2904

Venrick E. L., Mcgowan J. A., Cayan D. R., Hayward T. L., Climate and chlorophyll a: Long-term trends in the central North Pacific Ocean, Science (80-.)., 1987

Vera C., Higgins W., Amador J., Ambrizzi T., Garreaud R., Gochis D., Gutzler D., Lettenmaier D., Marengo J., Mechoso C. R., Nogues-Paegle J., Silva Dias P. L., Zhang C., Toward a unified view of the American monsoon systems, J. Clim., 2006, vol. 19, p. 4977

Viale M., Bianchi E., Cara L., Ruiz L. E., Villalba R., Pitte P., Masiokas M., Rivera J., Zalazar L., Contrasting climates at both sides of the Andes in Argentina and Chile, Front. Environ. Sci., 2019, vol. 7, p. 1

Vuille M., Bradley R. S., Keimig F., Climate variability in the Andes of Ecuador and its relation to tropical Pacific and Atlantic Sea Surface temperature anomalies, J. Clim., 2000

Wainer I., Servain J., Clauzet G., Is the decadal variability in the tropical Atlantic a precursor to the NAO?, Ann. Geophys., 2008, vol. 26, p. 4075

Wainer I., Venegas S. A., South Atlantic multidecadal variability in the climate system model, J. Clim., 2002, vol. 15, p. 1408

Wang H., Fu R., Cross-equatorial flow and seasonal cycle of precipitation over South America, J. Clim., 2002, vol. 15, p. 1591

Wilks D. S., Statistical Methods in the Atmospheric Sciences 3 edn, 2011, 699

Williams E., Dall' Antonia A., Dall' Antonia V., de Almeida J. M., Suarez F., Liebmann B., Malhado A. C. M., The drought of the century in the Amazon Basin: an analysis of

the regional variation of rainfall in South America in 1926, Acta Amaz., 2005, vol. 35, p. 231

Xu R., Wunsch D., Survey of clustering algorithms, IEEE Trans. Neural Networks, 2005, vol. 16, p. 645

Yamazaki Y., Rao V. B., Tropical cloudiness over the South Atlantic Ocean, Journal of the Meteorological Society of Japan, 1977, vol. 55, p. 205

Yoon J. H., Multi-model analysis of the Atlantic influence on Southern Amazon rainfall, Atmos. Sci. Lett., 2016, vol. 17, p. 122

Yoon J. H., Zeng N., An Atlantic influence on Amazon rainfall, Clim. Dyn., 2010, vol. 34, p. 249

Zhang R. H., Rothstein L. M., Busalacchi A. J., Origin of upper-ocean warming and El Nino change on decadal scales in the tropical Pacific Ocean, Nature, 1998

Zhou J., Lau K. M., Does a monsoon climate exist over South America?, J. Clim., 1998, vol. 11, p. 1020

Appendix

Appendix A

Section: Relationship between the Atlantic and the Pacific SST

A.1 Supplementary figures

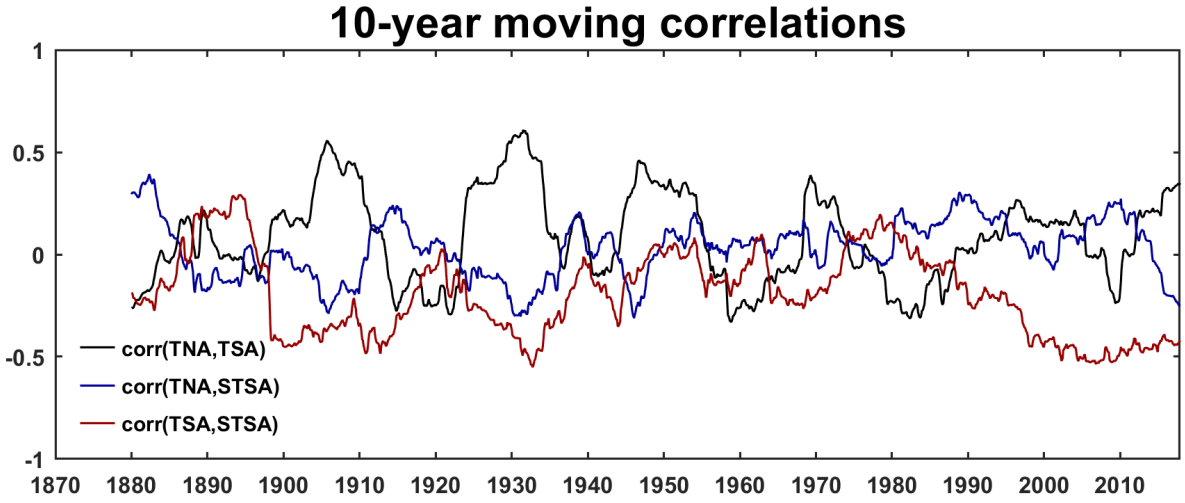

Figure A.1: 10-years moving correlation of the Atlantic regions: TNAi-TSAi (black), TNAi-STSAi (blue) y TSAi-STSAi (red).

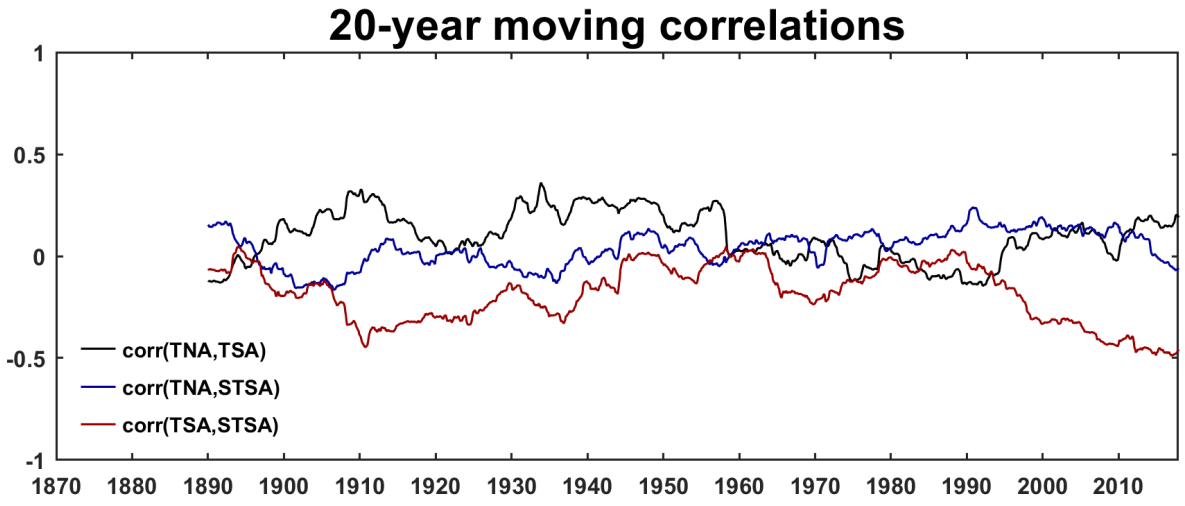

Figure A.2: 20-years moving correlation of the Atlantic regions: TNAi-TSAi (black), TNAi-STSAi (blue) y TSAi-STSAi (red).

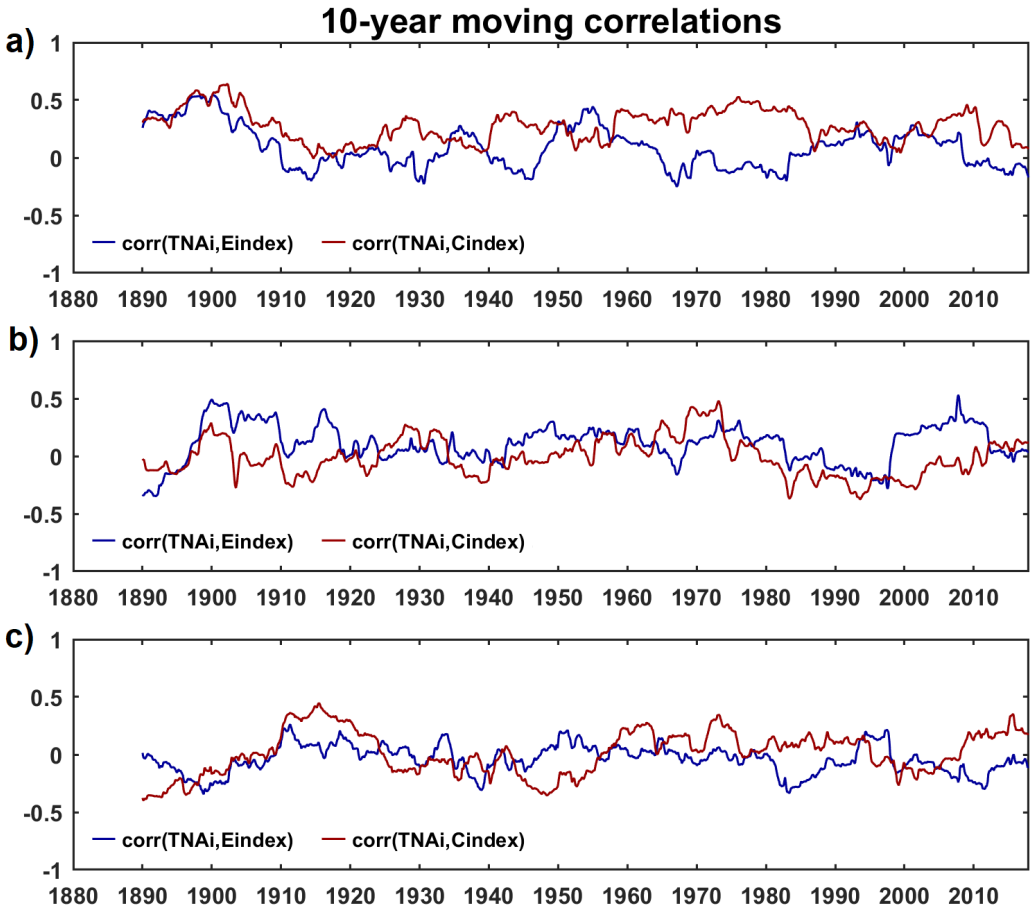

Figure A.3: 10-years moving correlation of the Atlantic regions: TNAi-TSAi (black), TNAi-STSAi (blue) y TSAi-STSAi (red).

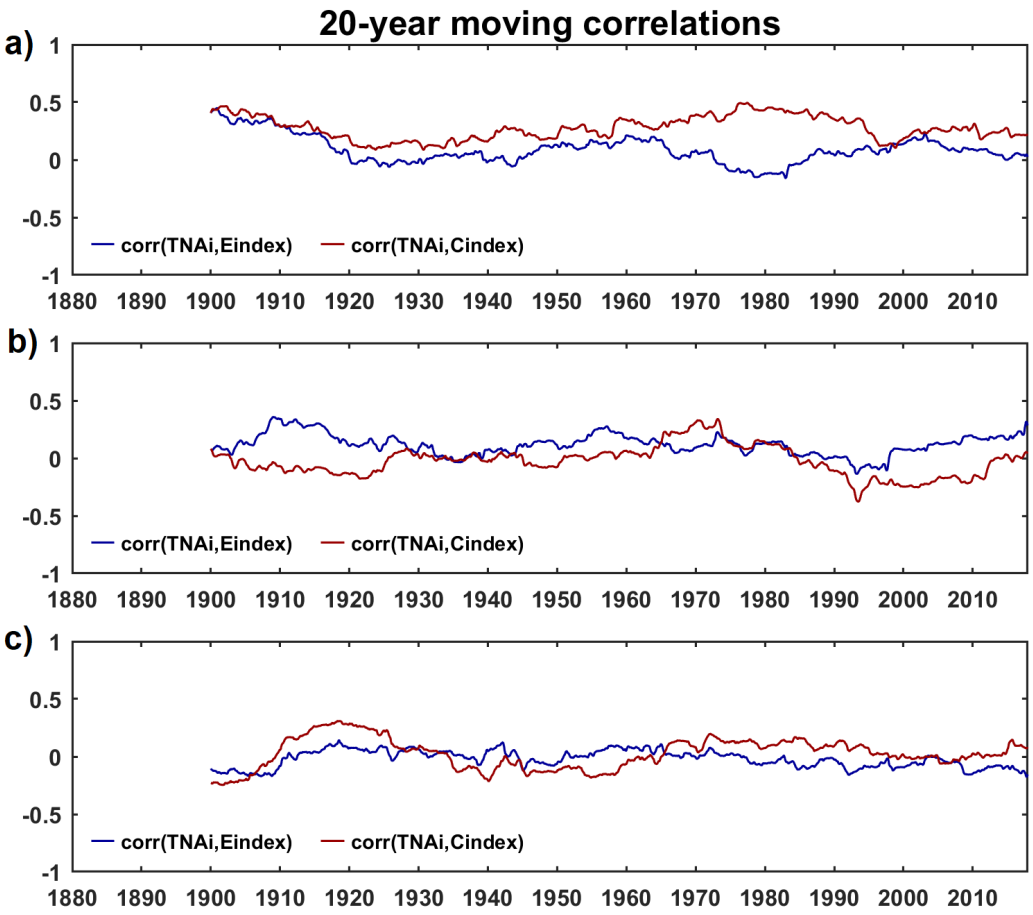

Figure A.4: 20-years moving correlation of the Atlantic regions: TNAi-TSAi (black), TNAi-STSAi (blue) y TSAi-STSAi (red).

Appendix B

Section: Influence of the SST on the precipitation

The relationship between Pacific and Atlantic SST indices are also computed considering three precipitation databases (TRMM, HyBAm and GPCC), to assess differences and similarities in the correlation results. In this section, we mainly compare the skill of the different hybrid precipitation datasets in relation to HyBAm observed data. In order to compare them, the 1998-2009 common period was considered. Correlation maps, comparing the three databases, are presented, considering the onset, peak and demise of the SAMS season and dry season (May-Sep). As mentioned in Section 4.4, from these correlations (positive or negative) we can infer flood or drought events.

B.1 October - November (ON)

During the onset of the SAMS season (ON; Figure B.1), correlations between precipitation anomalies and E index present significant negative values over the southernmost region of the Amazon Basin. These values are similar in the three databases analyzed (TRMM, HyBAm and GPCC).

Considering the C index, significant negative values in the northeast region of the Amazon Basin is observed. However, when the HyBAm data (Figure B.1b) was considered for the analysis, there are also significant negative correlations in the southern part of the basin. In addition, significant negative correlations are observed in the northwestern region of Argentina, and positive values in the southeastern region of South America and southern Chile, according to the results obtained from TRMM and GPCC data (Figure B.1a,c).

On the other hand, there is not influence by TNAi and TSAi, in this period. Accor-

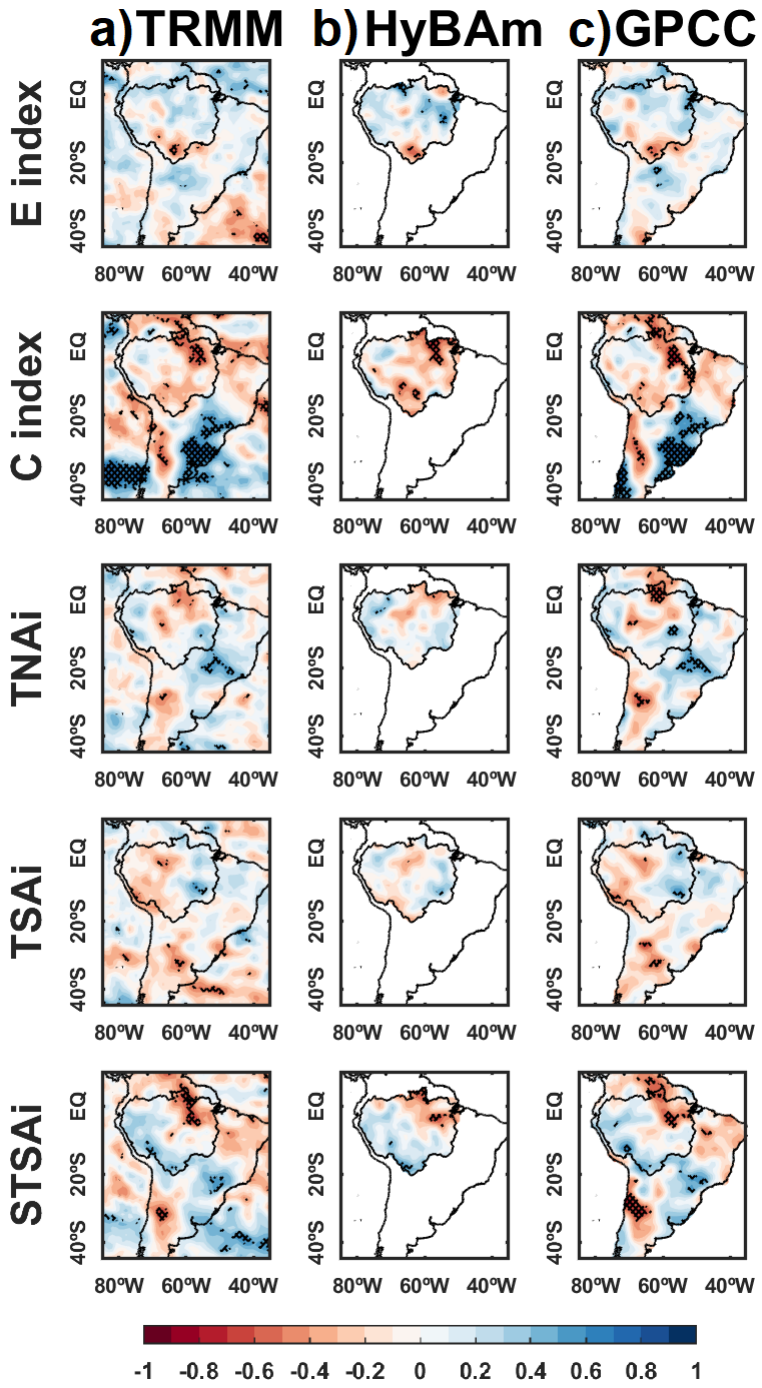

Figure B.1: October - November (ON) spatial correlation between precipitation anomalies and the Pacific (E and C index) and Atlantic (TNAi, TSAi and STSAi) SST indices for (a) TRMM, (b) HyBAm, and (c) GPCC databases. Blue (red) shadings indicate positive (negative) correlation, where statistically significant values are plotting in hatching.

ding to TRMM and GPCC databases (Figure B.1a, c), significant negative correlations is observed in the northernmost and a limited area in the central region of the Amazon Basin, concerning the TNAi. In contrast, there are significant positive correlations in the

southeast of the basin and Southeast of Brazil.

Finally, the STSAi influence in the north and northeast region of the Amazon Basin with negative correlations, and in the northwestern region of Argentina, according to TRMM and GPCC (Figure B.1a, c), with a slight difference between the three databases.

B.2 December - February (DJF)

During the peak of the SAMS season there are strong significant values, especially in relation to the Pacific region (E and C indices, Figure B.2). For the E index, negative correlations are located in the central Amazon Basin, considering the TRMM and HyBAm database (Figure B.2a, b); while GPCC data also show significant negative values in the east of the basin (Figure B.2c). On the other hand, positive correlations appear in the southeast and on the west coast of South America (Coastal region of Peru and Ecuador), for the TRMM and GPCC datasets (Figure B.2a, c). Correlations between precipitation anomalies and the C index show an intensification of negative values over the north and northeast of the Amazon Basin, and in the northeast region of South America in agreement with recent works (e.g. Cai et al., 2020). As was mentioned in Section 4.4, significant negative values also appear in the Andean region of the basin, most clear from HyBAm (Figure B.2b). According to Lagos et al. (2008) and Lavado-Casimiro and Espinoza (2014), anomalous conditions in the Central Pacific are strongly related with anomalous condition in the Peruvian Andes. Positive correlations decrease and move further north, in southeastern Brazil, according to TRMM and GPCC data (Figure B.2a, c).

In relation to the Atlantic indices, during this period, an increase in the intensity of these correlations are also observed. However, there are some differences when three databases (see Figure B.2) are separately analyzed. The influence of the TNA region on precipitation in the Amazon Basin is, basically, over the north and northeast of Basin. Considering the TSAi, significant negative values in the central Amazon Basin is observed, and in northern Argentina as well as. Significant impact is also observed in the climatological position of the ITCZ for the TRMM data. In contrast, positive correlation values are shown in southeastern of South America. Finally, the STSAi presents only positive influence, generating above-normal rainfall in the center of the Amazon Basin, the ITCZ,

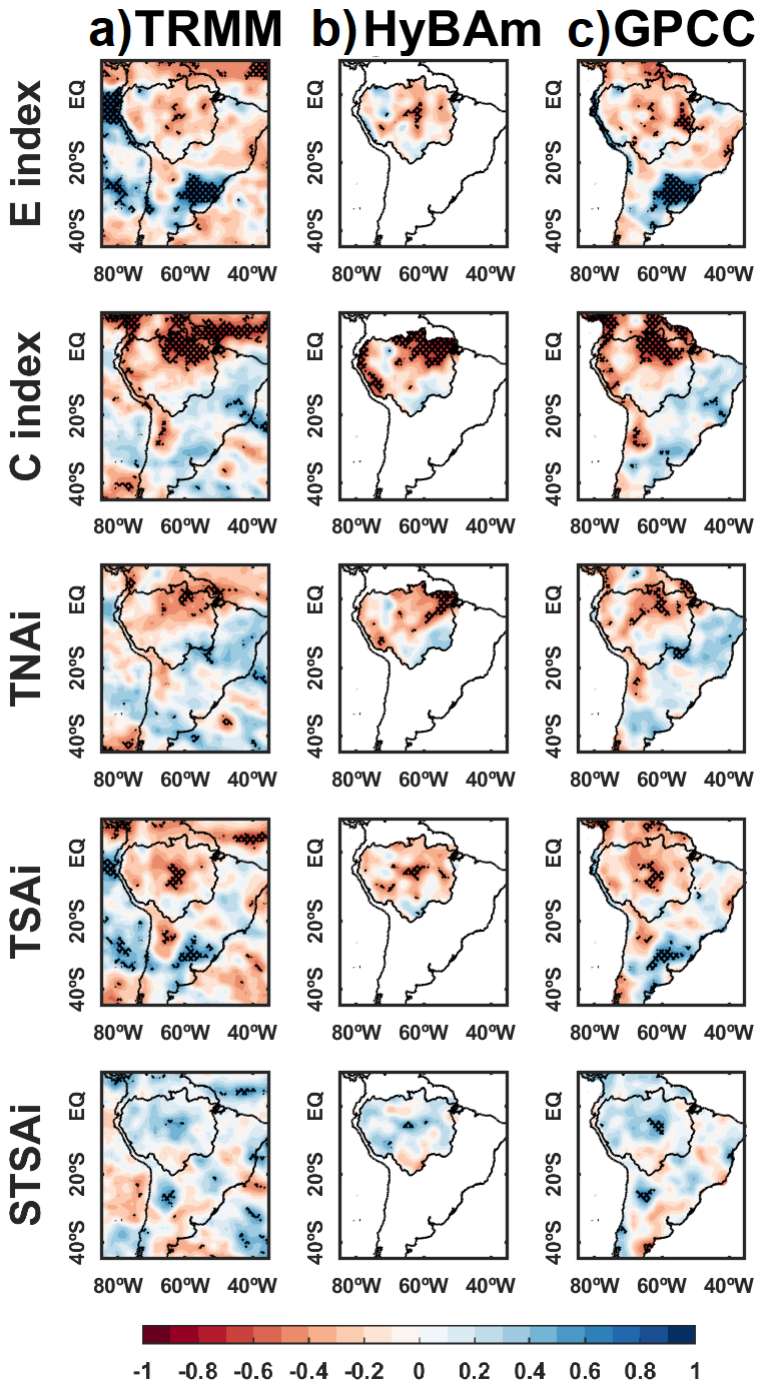

Figure B.2: As a Fig. B.1, but for December-February.

and northern Argentina.

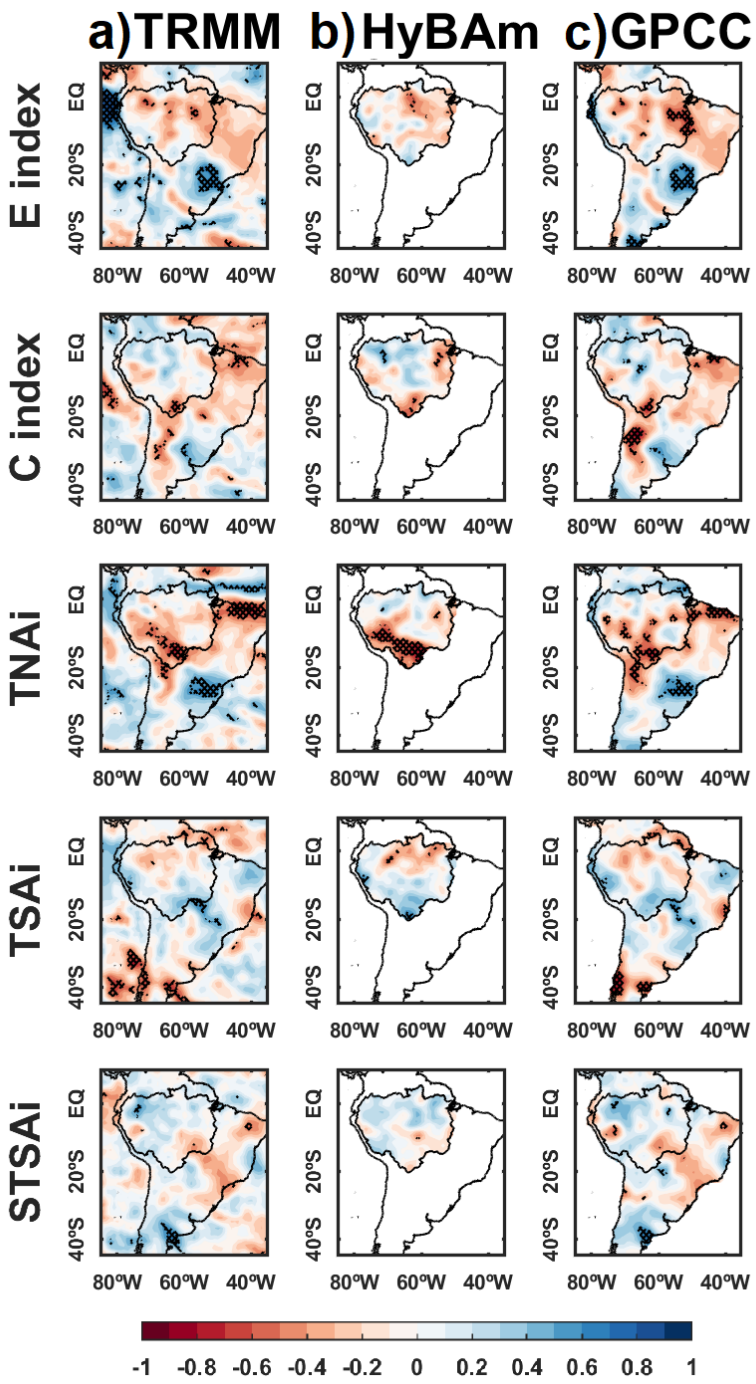

Figure B.3: As a Fig. B.1, but for March-April.

B.3 March - April (MA)

In the end of the SAMS season (Figure B.3) is hallmarked by a decrease in the intensity of the correlations, especially in the Pacific and South Atlantic indices. Correlations between the E index and precipitation presented significant decrease in its positive and

negative values. Negative values is mainly located over the eastern of the Amazon Basin, more noticeable in the GPCC data (Figure B.3c), and less positive values in the southeast of South America, in TRMM and GPCC (Figure B.3a, c). In relation to C index, the areas of positive and negative correlation are also weaker, leaving only scattered regions in the south of the basin, more noticeable in the HyBAm data (Figure B.3c).

As observed in the main text of this document, the relationship between rainfall and the TNAi presents significant negative values in the southern part of Amazon Basin and Northeast coast of Brazil. On the other hand, positive correlations have intensified in southeastern South America, according to TRMM and GPCC (Figure B.3a, c). Finally, correlations between precipitation and the TSAi and STSAi indices are not significant within the Amazon Basin for this period, but in the southern regions of South America, they show negative and positive correlations, respectively, according to the TRMM and GPCC data (Figure B.3a, c). Overall, and as observed in previous results, there is a strong coherence in the correlation maps among all datasets, therefore, the choice of GPCC data in the main document is justified.

B.4 May - September (MJJAS)

The "dry" period of the basin is mainly characterized by a minimal influence of the Pacific region (Figure B.4. As documented in previous papers and in this document, the May to September period is characterized by a non-active Pacific ENSO event. However, some influence is still observed in the extreme North of Peru, as occurred in the Coastal 2017 El Niño event (Garreaud, 2018; Peng et al., 2019). Correlations between precipitation and E/C index are not significant in the Amazon Basin.

On the other hand, the correlations between TNAi and precipitation anomalies intensified during this period, also observed in Section 4.4, showing significant negative values, spread throughout almost the entire Amazon Basin. Concerning the TSAi index, there are not influence on the precipitations in South America for this period. Finally, the correlations between precipitation and the STSAi index show significant negative values in the center of the Amazon Basin, more noticeable in the GPCC (Figure B.4c), and in the extreme northwest of the basin, as observed in HyBAm (Figure B.4b). Significant positive

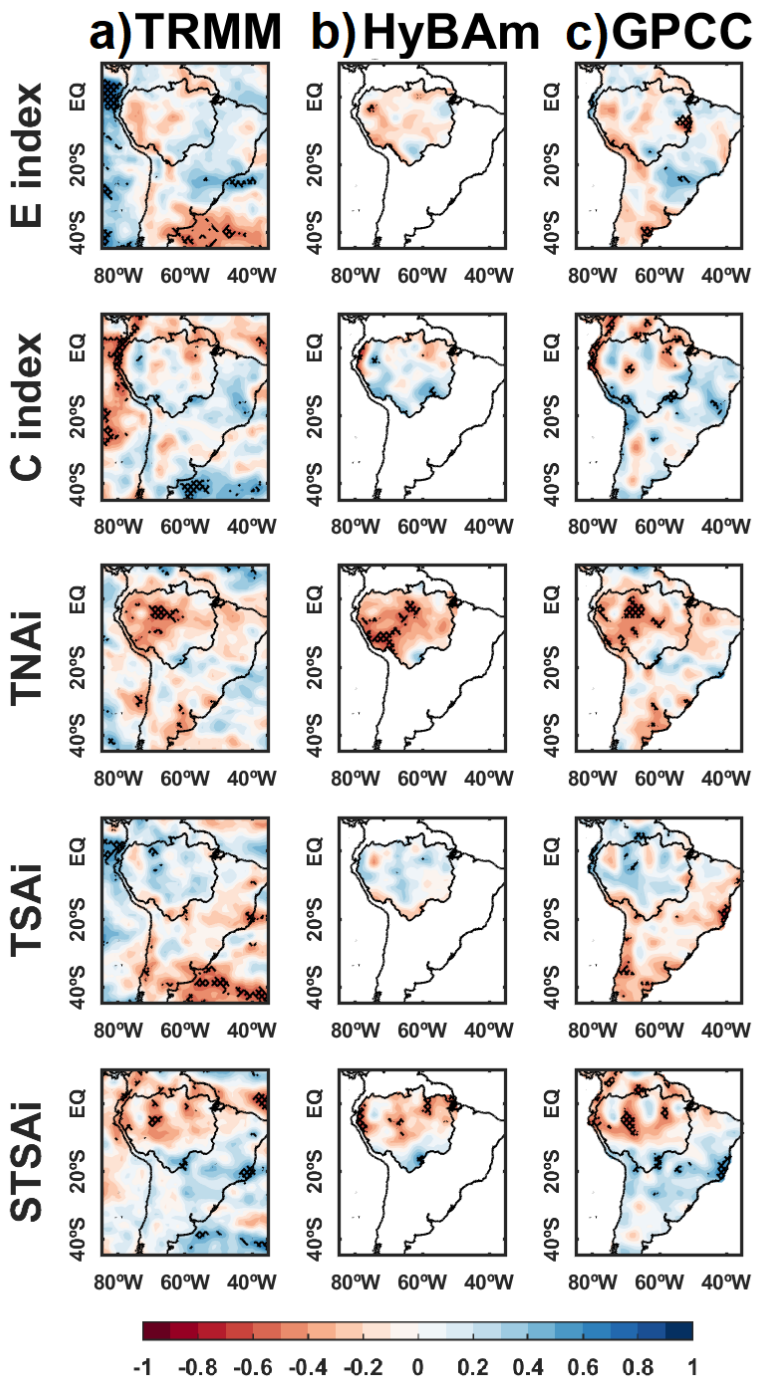

Figure B.4: As a Fig. B.1, but for May-September.

scattered regions in the south central of the continent correlations are observed in the three databases.